Stretchable Thermoelectric Devices for Wearable Electronics and Soft Robotics

Submitted in partial fulfillment of the requirements

for the degree of

Doctor of Philosophy

in

Mechanical Engineering

Mason Philip Zadan

B.S., Physics, University of Richmond

Carnegie Mellon University
Pittsburgh, PA
July, 2024

© Mason Philip Zadan 2024

All Rights Reserved

"...Immo, qui humili et constanti animo abscondita rerum perscrutari conatur, etsi inscius quasi manu Dei ducitur qui, res omnes sustinens, facit ut sint id quod sunt."

"...The humble and persevering investigator of the secrets of nature is being led as it were, the hand of God in spite of himself, for it is God, the conserver of all things, who made them what they are." (CCC para. 159)

Acknowledgements

I want to acknowledge my advisor Professor Carmel Majidi for his mentorship and continued support throughout my PhD. I am still not sure why he took me on as an undergrad research assistant in the summer of 2018 but I am thankful for it! Thank you for introducing me to a career I love. I have learned countless things from you and hope I have lived up to the standard of the lab.

I would like to thank my committee members including Professor Malakooti, Professor Yao, and Professor Shen. Learning from you all, in the context of a research setting and in the classroom, has been extremely rewarding. I am thankful for all of your mentorship over the years.

Thank you to my collaborators including Dinesh, Drew, Anthony, Dylan, Jiahe, Yiwen, Jingxian, Jeff, Wuzhou, Yafeng, Navid, Toby, and Jeremiah. Your dedication to research is inspiring and I thank you for all for the hard work that made this thesis possible.

I would like to thank my colleagues during my time at Meta Reality Labs including Omar, Yunsik, Marcos, and Chloe. Thank you all for being so welcoming and introducing me to research in an industry setting.

To Michael and Richard, thank you for your friendship.

To all of the Soft Machines Lab members past and present who I had the pleasure of working with, thank you for the fun times and your support.

To my friends from the University of Richmond, thank you for your friendship and for making me a better person. I love you all.

To my Family, thank you for your undying love and support. I love you all.

Doctoral committee:

Dr. Carmel Majidi (chair), *Carnegie Mellon University*

Dr. Mohammad H. Malakooti, *University of Washington*

Dr. Sheng Shen, *Carnegie Mellon University*

Dr. Lining Yao, *University of California, Berkeley*

Funding source:

I would like to acknowledge and thank my funding source the Nano-Bio Materials Consortium (NBMC), led by the Air Force Research Laboratory (AFRL) in partnership with SEMI (FA8650-18-2-5402). I would also like to thank the Air Force Research Laboratory (AFRL) Center of Excellence in Data-Driven Materials.

Abstract

As continuous wearable physiological monitoring systems become more ubiquitous in healthcare, there is an increasing need for power sources that can sustainably power wireless sensors and electronics for long durations. Wearable energy harvesting with thermoelectric devices (TEDs), in which body heat is converted to electrical energy through the Seebeck effect, presents a promising way to prolong wireless operation and address battery life concerns. To accomplish this, wearable energy harvesting devices will need to be made conformable and stretchable to operate on the human body and not impede comfort or movement. This requires advances in high-performance soft composite materials to keep power output high and not sacrifice bio-compatibility. In this dissertation, I introduce stretchable TEDs as a solution to both wearable health monitoring and soft robotic energy harvesting and thermoregulation needs. Liquid metal (LM) material architectures are introduced to replace traditionally rigid components such as coppers and ceramics. I focus this dissertation on (i) introducing TEDs that replace rigid components with LM composites, elastomers, and 3D printing, (ii) developing a novel approach to soft robotic actuation using liquid crystal elastomer (LCE) shape memory polymers combined with 3D printed TEDs, (iii) developing high power density TEDs and integrating them to power a PPG monitoring system, and (iv) exploring 2D MXene sheets in LM composites to effect the properties of thermal interface materials (TIM). (v) Lastly, I discuss future work on direct ink-writing of thermoelectric inks.

Contents

List of Tables

List of Figures

Chapter 1

Introduction

- **M. Zadan**, C. Chiew, C. Majidi, and M. H. Malakooti, "Liquid Metal Architectures for Soft and Wearable Energy Harvesting Devices", *Multifunctional Materials*, vol. 4, no. 1, p. 012001, 2021.

1.1 Background and Motivation

1.1.1 Progress in Wearable Energy Harvesting

As wearable electronics become more readily available and implemented for more complex and diverse tasks, the power requirements of wearable computing have also increased. Onboard human body-generated power supplies have come alongside them to generate energy from biomechanical motion and heat generated from the body[1, 2, 3]. Each of these types of wearable energy harvesting devices can harness energy from the human body using different energy conversion mechanisms (figure 1.1a). For instance, wearable thermoelectric generators (TEGs) convert thermal energy from body heat to electrical energy through the Seebeck effect in which temperature differentials between the skin and the environment across positively and negatively doped semiconductors create a potential difference[4, 5]. Separately, thermoelectric devices (TED) can also act as solid state coolers through the Peltier

effect when current is applied across the semiconductors [6].

Other methods for wearable energy harvesting include wearable triboelectric nanogenerators (TENGs) and electromechanical energy harvesters—including dielectric elastomer generators (DEGs) and piezoelectric generators (PEGs). In contrast to TEGs, these methods generally convert biomechanical kinetic energy to electrical energy. They can scavenge energy from various modes of biomechanical motion on many points of the body such as the knee, hip, shoulder, elbow joint motion, and heel strike[7]. In particular, TENGs harness these biomechanical motions by electrostatic induction from the contact separation mechanism between materials with different intrinsic tendencies for gaining or losing electrons[8, 9]. DEGs generate energy from capacitive changes of charged electrodes sandwiching a dielectric elastomer sheet as it stretches and relaxes with biomechanical movement[10, 11]. This human motion, such as bending the knee or arm, forces the charges to reconfigure on the elastomer as it is stretched, generating varying voltages. PEGs use active materials with high electromechanical coupling coefficients, which intrinsically converts mechanical deformations (i.e. pressure, vibration, body movement) into electrical signal or vice versa[12]. They are widely used among commercial sensors and actuators[13, 14] but increasingly utilized for wearable, flexible and wireless energy harvesting[15, 16, 17].

1.1.2 Thermoelectric Seebeck Energy Harvesting

Among the various approaches to wearable energy harvesting, TEGs, have stood out for their ability to generate power continuously without the requirement of movement. The effectiveness of these semiconductors is captured by the semiconductors figure of merit (ZT), which is described as $ZT = \frac{\alpha^2\sigma}{\lambda}T$ where α is the Seebeck coefficient, σ is the electrical conductivity, λ is the thermal conductivity, and T is the temperature[18]. The TEG output power $P_{TEG} = (\alpha\Delta T)^2\sigma$ depends on semiconductor Seebeck coefficient α, local thermal gradient (ΔT), and the electrical conductivity (σ)[18]. For operation on the body, TEGs must be made flexible for both comfort and improved contact with the skin. Commercially available TEGs

Figure 1.1: Liquid metals in wearable energy harvesting devices. **a**, image highlighting the applications and locations of LM based wearable electronics. Inset top left: liquid metal embedded elastomer based TEG [20]. Inset bottom left: LM foam based shoe insert TENG [21]. Inset top right: LM microfluidic and composite elastomer based wrist worn TEG [22]. Inset bottom right: LMEE based joint worn TENG [23]. **b**, Liquid metal embedded elastomer under deformation [24]. **c**, Liquid metal being poured. **d**, Example of LM microfluidics [25].

do not meet this need.

1.1.3 Thermoelectric Peltier Coolers

Separate from the energy harvesting potential of TEDs through the Seebeck effect, TEDs also act as solid state cooling devices through the Peltier effect. When operated as Peltier coolers, a current is applied across the semiconductor junctions inducing a temperature differential between the two sides. The cooling capacity Q_c can be calculated from $Q_c = Q_g - Q_d - \frac{1}{2}Q_j$ where $Q_g = \alpha I T_c$ is the thermoelectric cooling term, $Q_d = -K\Delta T$ is the conductive heat flow across the semiconductor junctions, and $Q_j = RI^2$ is the joule heat. I is the current across the semiconductor junctions, K is the thermal conductance, T_c is the temperature of the cold side, and R which is the electrical resistance of the thermo-elements [19].

1.1.4 The Need for Soft Materials in Wearables

Compatibility between the device and the body has become an area of research for more conformable and efficient wearable systems. High elastic mismatch between skin and conventionally rigid electronics, poor breathability, and limited durability under large deformations are some of the common challenges. To address these issues, soft and stretchable components are implemented, with special emphasis on the use of elastomers and textiles. While these soft components provide flexibility at some level, key rigid components are still required. These include stiff electrodes (e.g. copper for wiring) and thermal interfaces (e.g. ceramics for thermal management). As soft encapsulating components and rigid components interact with each other while trying to operate on the ever-changing morphologies of the human body, issues can occur. These issues include loss of contact between the device and body from the rigid components, short device lifetime due to the weak bonding and high stress concentration at the soft and rigid interface, and a lack of comfort for wearers. The more components of wearable energy harvesters that can be made soft and compliant to human movement, the more efficient, robust, and comfortable these devices will become.

Overview of Liquid Metal based Soft Materials

To address the materials challenges, room temperature liquid metal (LM) alloys have increasingly been explored as a potential replacement for circuit interconnects and thermal interfaces in electronic devices. For wearable applications, LM can be used to replace wiring[26, 27], thermal interfaces[20, 24, 28], and dielectric materials[29]. LM alloys of gallium (Ga) such as EGaIn are liquid at room temperature, have low viscosities, high thermal conductivities ($20-30 W m^{-1} K^{-1}$)[30, 31, 32], high electrical conductivities ($1-4\times10^{6}\ S m^{-1}$)[33] and low toxicities[34, 35]. To harness these properties in wearable electronics, LMs can be packaged as microfluidics[36, 37], and LM embedded elastomer (LMEE) composites[24, 38, 39, 40, 41, 42] (figures 1.1b-d). Design constraints for wearable energy harvesters are conformability with a user's skin, biocompatibility, structural integrity, and stable functionality (i.e. thermal

and electrical properties), [43, 44, 45]. LM fluidics and LMEE are two current LM material architectures that have the potential to meet the needs of materials in wearable energy harvesting if improvements can be made.

1.1.5 Stimulation Methods for Thermally Responsive Liquid Crystal Elastomer Actuators

Liquid crystal elastomers (LCEs) are a class of shape memory polymer (SMP) composed of loosely crosslinked polymer networks that exhibit reversible shape change during transitions from nematic to isotropic phases[46]. They have become increasingly popular as actuators for use in soft robotics[47, 48, 49], wearable computing and haptics[50, 51], and shape morphing matter [52, 53, 54] on account of their muscle-like work density and contraction strain[55, 56, 57, 58, 59] and ability to be printed or patterned into a wide range of geometries[60, 61]. In most robotics and engineering applications, LCE-based actuators are stimulated thermally using an external heat source or electrically through Joule heating using an integrated wire or embedded network of percolating particles. Previous work has focused on heating LCEs primarily through Joule heating[51, 57, 58, 62, 63], with many of these applications using LM [64, 65, 66] and wavy electronics[57, 58, 67, 68] as a heating element.

However, a key limitation of these approaches is their reliance on open-loop heating and passive cooling. This results in slow changes in temperature and a limited ability to control the speed and profile of the LCE actuator response. In particular, actuation speeds can be slow due to the LCE's low thermal conductivity of 0.3 $Wm^{-1}K^{-1}$[65] and cooling speed is greatly limited due to heat transfer by convection rather than conduction. The latter results in cooling times that can take five times[57, 69], 10 times[58],or even up to 50 times[70] the activation time in order for the LCE to cool under ambient conditions and return to its original state. Moreover, faster actuation speeds have been shown to require longer cool down times due to the greater increase in temperature[70]. To decrease heating times, soft fillers such as LM droplets have been embedded to increase the thermal conductivity of these

architectures[51]. Issues with cooling times still persist, with these differences in heating and cooling times being functions of the difference in the rate of heat transfer between conduction (heating) and convection (cooling); smarter approaches are needed to address this issue. One potential solution is to introduce TED Peltier coolers into these systems.

The Need for Soft Actuation Methods

Current robotic systems use rigid components such as servomotors, clutches, and hydraulics to navigate through the environment and interact with individuals and objects. These rigid robotic systems are modular, and often times task specific being non-multifunctional. These drawbacks develop from the constraints imposed by manufacturing and design. These traditional robotic systems oftentimes contain separate segments for computation, energy storage, sensing, and actuation [71]. The field of soft robotic systems has begun to address this by replacing rigid components with soft and deformable replacements [72]. This has included soft tactile sensing skins [73], soft grippers [74], along with actuators enabled by pneumatics, shape memory alloys (SMA), particle jamming, and dielectric elastomer actuators [75, 76, 77, 55]. Liquid crystal elastomer (LCE) has recently emerged as a thermally responsive shape memory polymer (SMP) that has applications in soft robotics [78].

1.2 Objectives and Dissertation Overview

My dissertation focuses on (i) designing and fabricating soft and deformable TEDs and exploring TED design parameters for improved performance, (ii) integrating soft TEDs into thermal responsive polymers to develop actively heated and cooled soft robotic limbs for actuation along with energy recovery, (iii) developing TEDs to power a photoplethysmography (PPG) wearable health monitoring systems, (iv) introducing $Ti_3C_2T_x$ MXene 2D materials into soft LM composites to improve thermal and electrical properties, and (v) discussing future research directions to move away from rigid Bi_2Te_3 semiconductors to direct ink

written (DIW) thermoelectric-LM ink composites.

The research questions of this dissertation are:

1. Can soft LM based multi-functional elastomers be introduced to replaced the rigid components in TEDs to create stretchable wearable energy harvesting devices?
2. Can soft TEDs be combined with soft thermally responsive materials (LCE) and provide active heating/cooling without impairing their mechanics or natural response to thermal stimulation?
3. Can stretchable TED performance be improved using novel soft thermal and electrical materials to power wearable battery-free PPG health sensing wearables from body heat?
4. How can 2D materials such as $Ti_3C_2T_X$ MXenes effect the performance of soft LM based elastomeric thermal interface materials (TIM)?

The dissertation is presented in the following structure.

In Chapter 2, I introduce a stretchable TEG that replaces two of the main rigid components in TEGs: copper interconnects between the semiconductors and a ceramic TIM. LMEE composites, which consist of LM inclusions embedded within a silicone elastomer, are introduced to function as both the thermal interface and electrical interconnects. I characterize the electromechanical performance under a host of wearable conditions.

In Chapter 3, I present a novel soft robotic limb made of an improved 3D printed soft TEDs placed between two LCE SMP layers. This transducer functions as an actuator that bends in response to thermal input from the TED. During actuation, one LCE layer heats and the opposing layer cools inducing reversible actuation. I also introduce these limbs as energy harvesters capable of recycling energy during intra-cycle cool downs and generating energy from the surrounding environment. These actuators are extensively characterized.

In Chapter 4, I demonstrate material and design improvements to greatly increase TED performance to a point where the TEDs fully power a PPG monitoring systems. To enable this performance improvement, I introduce a conductive LM-Ag-SIS ink for interconnects

and a novel LM-epoxy TIM. I also explore the design choices of semiconductor density, aspect ratio, and TIM thermal conductivity on performance. Lastly, I demonstrate these TEGs powering the "TEGsense" PPG monitoring wearable.

In Chapter 5, I develop MXene-LM composites, and explore the influence that 2D MXene sheets have on LM droplets. MXenes are wrapped around micron scale LM droplets which makes them electrically conductive along with functionalizng the surface. These coated droplets when added to a matrix material aggregate into larger clusters. These clusters increase thermal and electrical performance at low bond line thickness (BLT). I conduct microCT imaging to better understand MXenes as an aggregation mechanism for soft LM composites.

In Chapter 6, I conclude this dissertation by summarizing the key outcomes and contributions. I also discuss limitations and potential next steps including future research directions on DIW-printable thermoelectric inks. Even with the bulk of the materials in TEDs being soft and stretchable, the semiconductors themselves are still rigid. This can cause stress concentrations at the rigid-soft interface. Thermoelectric semiconductors are often fabricated through high temperature annealing making them rigid and brittle. To mitigate this, I will discuss leveraging the advantages of LM composites to explore 3D printing of thermoelectric composites with LM potentially as a binder embedded in an elastomer matrix.

Chapter 2

Liquid Metal Embedded Elastomers for Soft and Stretchable Thermoelectrics

- **M. Zadan***, M. H. Malakooti*, and C. Majidi, "Soft and Stretchable Thermoelectric Generators Enabled by Liquid Metal Elastomer Composites", *ACS Applied Materials & Interfaces*, vol. 12, no. 15, p. 17921-17928, 2020.

2.1 Introduction

Thermoelectric generators (TEGs) are a simple and effective way to harvest excess (and otherwise wasted) energy from body heat in order to power wearable sensors and circuitry [79, 80, 81, 82]. These devices have been shown to have the potential to power a myriad of electronic devices including implantable medical devices, internet of things (IoT) technologies, wireless body area networks, and wearable devices for applications ranging from glucose sensing to global positioning system tracking [83, 84, 85, 86, 45, 87, 88]. While promising for some use cases, existing wearable TEG technologies are primarily made of rigid or inextensible materials that limit their ability to conform to the skin or support repeated mechanical deformation[2]. For wearable applications, reliable heat absorption is greatly improved through the use of flexible materials to fabricate TEGs that can conform to the skin

and accommodate natural human motion. Previous studies have incorporated polydimethylsiloxane (PDMS) and polymers in order to replace more rigid materials, resulting in flexible TEGs that are more compatible with the body[89, 90, 91]. One such study used PDMS as a matrix material along with rigid semiconductors that were connected using copper interconnects[92]. This resulted in a flexible and bendable TEG, although performance was limited to an electrical power output of 2.1 μW when exposed to a temperature difference of ΔT = 19 °C. A more recent study on thermoelectric devices (TEDs) for limb cooling aligned semiconductors between two elastomer sheets in the open air, thereby mitigating the thermal conductivity between the top and bottom elastomer pieces[93]. A separate study introduced a flexible PDMS TEG composed of an array of 144 bismuth telluride semiconductor chips wired together using thin, flexible, and yet inextensible copper interconnects. This TEG was combined with a boost converter in order to power a device capable of electrocardiography, thereby showing the potential of flexible TEGs for wearable biomonitoring and electronics applications[94, 95].

The drawbacks in these and other previous elastomer-based soft TEGs follow from the use of PDMS as an encapsulating material. PDMS is a thermal insulator with a low thermal conductivity of 0.18 W $m^{-1}K^{-1}$ that has the potential to interfere with the flow of heat to and from the thermoelectric modules[83]. Moreover, wiring the thermoelectric components with rigid or inextensible electrical interconnects results in a device that cannot stretch and fully conform to the body. Since rigid interconnects cannot deform with the surrounding elastomer, they can induce high stress concentrations that can lead to fracture or delamination and consequently mechanical or electrical failure of the device. Progress toward the development of mechanically robust TEGs for wearable computing depends on the use of soft and stretchable materials for thermally conductive encapsulation and internal electrical wiring.

Gallium-based liquid metal (LM) alloys such as eutectic gallium–indium (EGaIn) and gallium–indium–tin (Galinstan) are a promising class of materials for addressing existing

challenges in creating soft and stretchable TEGs. The high electrical conductivity and ability of EGaIn to deform and move with the surrounding materials makes it an excellent candidate as a conductive material for stretchable electronic devices[96, 97, 98, 99, 100]. This unique ability of EGaIn has been incorporated in simple applications for TEGs to aid as the interconnects between semiconductors[101, 102]. In one such study, EGaIn channels were embedded within PDMS and functioned as electrical interconnects connecting the TEG semiconductors[103]. Besides the complex fabrication process, the resulting TEG exhibited limited voltage and power generation (8.22 mV and 46.28 μW, respectively, for a Δ30 °C temperature difference) but demonstrated that EGaIn is a promising material for electrical interconnects in such applications. Similar to previously reported flexible TEGs, the major drawback was the poor thermal management in the device because of the low thermal conductivity of the encapsulating elastomer. More recently, the design of TEGs with EGaIn channels was improved by enhancing the thermal conductivity of pure PDMS[22].

Alternatively, LM alloys have been incorporated into flexible and stretchable devices by suspending LM micro/nanodroplets within an elastomeric matrix. Such LM-embedded elastomers (LMEEs) have been shown to exhibit exceptional electrical and thermal properties with a wide range of applications[38]. LMEEs have also been shown to operate effectively under extreme cold weather conditions because of the supercooling effects that suppress the freezing temperature of LM alloys encased in this elastomer composite from -5.9 to -84.1 °C. This freezing point suppression addresses operating challenges in LM alloy based TEGs in cold weather environments[28]. Particularly for TEG applications, it was recently shown that utilizing LMEE thermal interfaces rather than insulating elastomers significantly improves the energy harvesting performance of TEGs[28]. Here, I show that stretchable high performance TEGs can be simply designed and fabricated by utilizing LMEE composites both as a stretchable circuit wiring and a thermally-conductive elastomer for more efficient heat management.

In this chapter, I introduce a soft and stretchable TEG for cold weather conditions

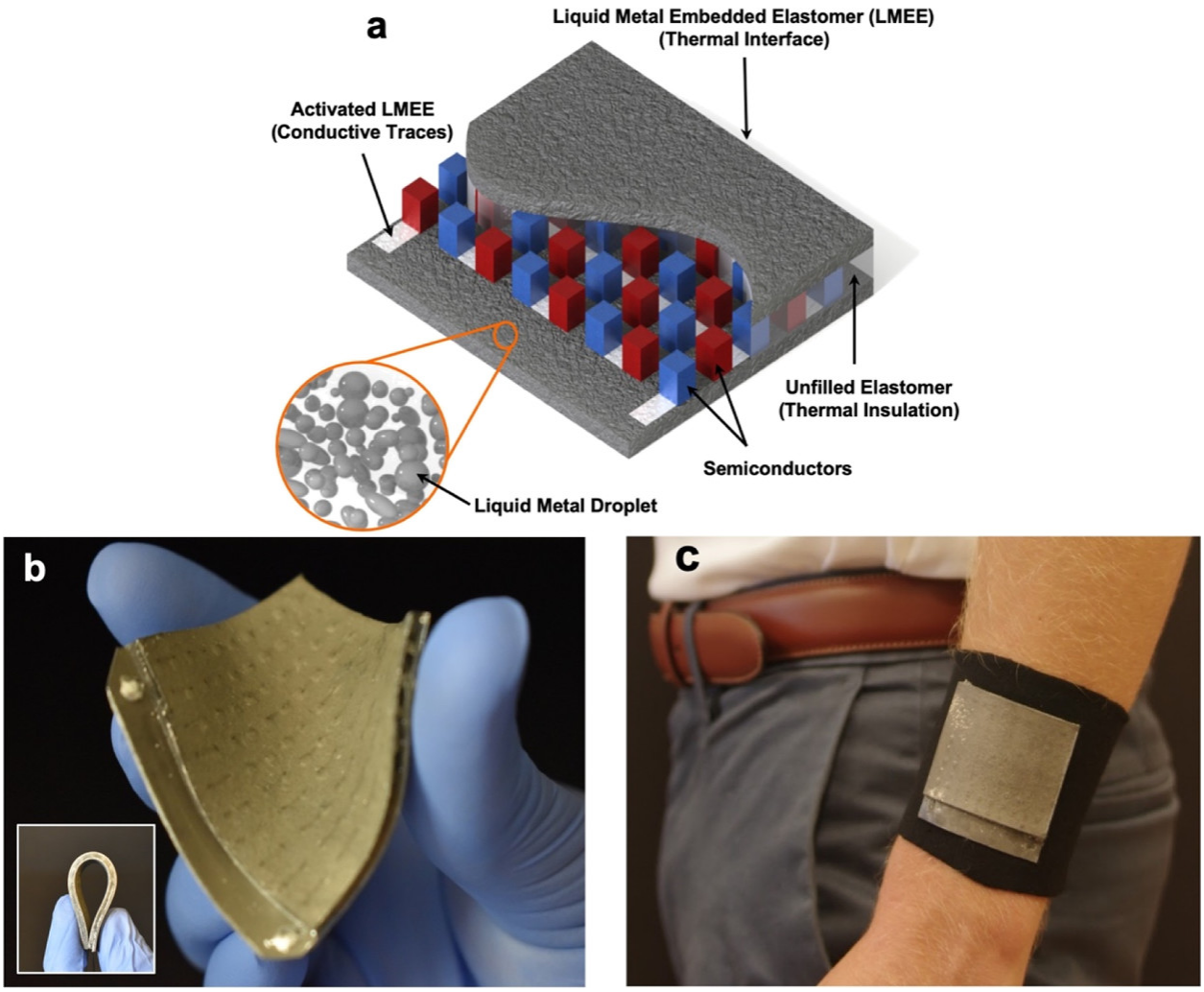

Figure 2.1: Stretchable TEGs with a LM embedded elastomer (LMEE). **a**, Schematic of the stretchable TEG with a thermally conductive LMEE as the material interface on the top and bottom. The LMEE contains a mechanically sintered pattern for providing electrical connections between p-type and n-type Bi2Te3 semiconductors. **b**, A photo of the fabricated TEG under deformation (inset: a TEG device completely bent). The raised bumps on the surface of the TEG are the locations of the LMEE conforming around the semiconductors. **c**, Stretchable TEG conforming to the forearm when attached to a fabric armband.

that utilizes an electrically insulating and conductive LMEE for thermal management and electrical connectivity between embedded, milli-scale Bi_2Te_3 components. As shown in Figure 2.1a, the device is composed of a top and bottom LMEE layer that acts as a heat spreader and forms electrical interconnects between the Bi_2Te_3 chips when mechanically sintered. The LMEE layers are composed of LM droplets dispersed in a soft silicone elastomer matrix. Their high elastic compliance and thermal conductivity enable the layers to conform

intimately to the skin and transport heat through the embedded thermoelectric components. Moreover, the LMEE can be locally "sintered" with mechanical activation in order to create electrically conductive traces on the normally electrically insulating LMEE that makes connections between the embedded semiconductor components, thereby eliminating the need for additional components to individually connect the semiconductors. Specifically, the electrically conductive LMEE traces eliminate the need for rigid copper interconnects that would otherwise be required for serial connection of the semiconductors. Because the LMEE serves two crucial functions in the TEG device and reduces the number of required components in the device, the fabrication process is significantly simplified. Moreover, because the device is primarily composed of soft and stretchable elastomers, these TEGs are highly flexible (Figure 2.1b) and can be strained to over 50% in tension without electrical or mechanical failure, exceeding the strain limit of previous TEGs and well above the deformation needed for wearable electronic applications. Furthermore, they exhibit only a small increase in resistance when stretched and do not permanently deform because of repeated cyclic loading. Such advantages give the TEGs presented here the ability to remain functional while bending and stretching in order to conform to the body (Figure 2.1c).

2.2 Thermoelectric Generator Design and Fabrication

Figure 2.2a,b illustrate the steps of the fabrication process. The overall structure of this device consists of three main components: a top and bottom layer of the LMEE and an insulating PDMS center layer embedded with an array of semiconductors. LMEE's excellent thermal conductivity and electrical properties lend itself well for this device since the material can act as a conformable area of contact for heat absorption and also as an array of electrical interconnects between the semiconductors. In particular, LMEE composites with a 50% LM volume fraction have a thermal conductivity of 1.6 $m^{-1}K^{-1}$ in their unstretched state, which makes them excellent for thermal absorption[24]. A 50% fill percentage was selected for these

devices because the thermal conductivity of the LMEE is a function of the fill percentages of the LM alloy, with an increase in the fill percentage corresponding to an increase in thermal conductivity[24]. Specifically, 50% has been shown to work well for not only thermal but also electrical applications[104]. This fill percentage is high enough to create percolating networks when sintered with an excellent conductivity of σ = 1.37 $\times 10^5$ S m^{-1} but low enough to be electrically insulating when not activated as shown in a previous work[104, 40]. The LMEE was fabricated using a mixture of eutectic gallium indium (EGaIn; 75% gallium and 25% indium by mass) at a 50% fill ratio with a PDMS (Sylgard 184; Dow Chemicals) matrix and cured for 1 h at 100 °C.

These bismuth telluride semiconductors were selected for their high efficiency and figure of merit (ZT) of ≥ 1.1 at 300 K. High efficiency is a relative term—for example, high performance Bi_2Te_3 semiconductors with a ZT = 1 at ΔT 50 °C have an efficiency of only around 3.5%. This indicates the importance of selecting appropriate thermal materials when developing a TEG device[5]. Comparing these semiconductor's figure of merit with those reported in the literature for Bi_2Te_3 semiconductors, the figure of merit of these devices at 300 K is in line and comparable to those of other semiconductors making them an excellent choice for thermoelectric energy harvesting[18, 105, 106]. Referring to Figure 2.2c,d, P and N-type semiconductors (Wuhan Xinrong New Materials Co., Ltd.) were placed in the alternating order in one hundred square holes that were patterned within a layer of PDMS (Sylgard 184, Dow Chemicals). For this layer, I cured Sylgard 184 with a 10:1 elastomer to curing agent ratio (by mass) in a 50 × 50 × 1.3 mm mold. The PDMS center layer was cut from the cured PDMS molds using a CO2 laser cutter (VLS 3.50, Universal Laser Systems) and one hundred square holes for the semiconductors were cut with a dimension of 1.1 × 1.1 mm. The semiconductor "legs" have a dimension of 1.4 × 1.4 × 1.6 mm with a height to width aspect ratio of 1.14. To decrease contact resistance caused by the semiconductors and interconnects, EGaIn was sputtered onto the top and bottom of the semiconductors. To selectively deposit the EGaIn, a flexible stencil was placed on both sides of the center PDMS

structure with cutouts for the semiconductors. EGaIn was airbrushed on the top and bottom and the stencil was removed leaving EGaIn only on the ends of the semiconductors.

To achieve electrical connection between the embedded semiconductors, internal interconnects were created by mechanically activating the LMEE composite. By applying constant force, the suspended EGaIn droplets are ruptured internally to create conductive pathways for electrical circuitry[40]. When activated, these pathways can have a volumetric conductivity as high as $\sigma = 1.37 \times 10^5 Sm^{-1}$, therefore being conductive enough to replace copper or other rigid conductors and thereby greatly cutting down on the complexity of fabrication[104]. In this application, pressure from a pen was used to activate the LMEE and create electrical interconnects between the adjacent semiconductor legs. This mechanical patterning was performed on the top and bottom LMEE layers in order to support the array of 100 semiconductors (Figure 2.2a,e).

After interconnect patterning, the elastomer pieces were bonded together with the aid of oxygen plasma treatment (SPI Plasma Prep II) in order to activate the surfaces and allow for strong adhesion[107, 108]. Following the plasma treatment, the three pieces were manually aligned and bonded together. Glass slides were placed on the top and bottom of the device and a clamp held the device together. It was finally cured in an oven for 1 h at 100 °C. Figure 2.2f gives a view of the cured TEG with a final dimension of 41.0 × 47.3 × 3.0 mm in which the raised dots and darkened lines on the surface highlight the semiconductor placement and sintered interconnect pathways, respectively. The embedded semiconductors and interconnects, deforming along with this TEG, can move and operate reliably under extreme strain such as the positions in Figure 2.2g,h in which the semiconductors are highlighted along the side view (Figure 2.2g). Figure 2.2h highlights the lack of damage, hysteresis, or tearing after 1000 cycles of 30% for these TEGs.

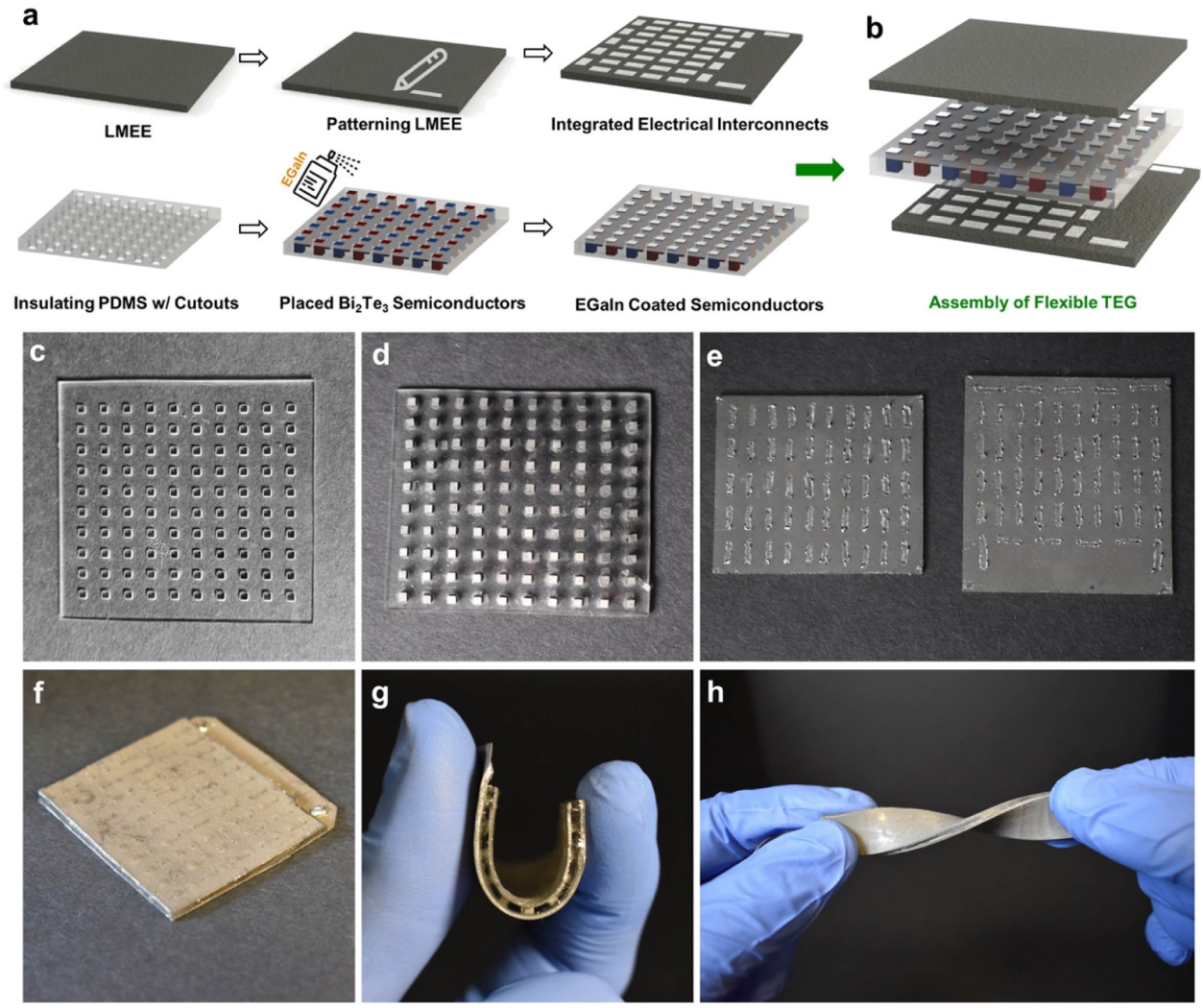

Figure 2.2: Fabrication process of the stretchable TEG with LM composites. **a**, Fabrication schematic highlighting the creation of the semiconductor interconnects through LMEE mechanical activation along with EGaIn sputtering onto the semiconductor array. **b**, Schematic of TEG assembly once the internal side of LMEE layers is oxygen plasma treated. **c**, The laser cut PDMS center layer with cutouts for the semiconductors. **d**, Insulating center layer of PDMS with one hundred Bi_2Te_3 semiconductors in P and N alternating alignment. **e**, Patterned top (left) and bottom (right) LMEE pieces, the patterns will serve as electrical connections between individual semiconductors. **f**, Assembled 42 × 48 mm stretchable TEG with raised bumps indicating alignment and position of semiconductors. **g**, Side view of the TEG bending 180° with semiconductors visible and deforming with the device. **h**, Photograph of a TEG post 1000 loading cycles with no damage or hysteresis.

2.3 Seebeck Characterization

In order to understand the thermoelectric performance of these stretchable TEGs, the open-circuit voltage was measured as a function of the temperature difference between the two

sides of the stretchable TEG devices. Figure 2.3a shows the increase of the open circuit voltage as the temperature gradient increases. Voltage was measured by placing the TEG on a hot plate at varying discrete temperatures from 35 to 105 °C with increments of 10 °C. Longer exposure of the TEG on the hotplate amounted to a loss in voltage. This occurred much more quickly at higher temperatures, as the heat transferred from the bottom of the TEG to the top more quickly lowering the temperature gradient. The reported open-circuit voltage for each sample was measured as the peak voltage value obtained using an oscilloscope (Rigol DS1054Z). To ensure consistency in the measurements providing intimate contact with the hot plate and absorbing heat, a 440 g aluminum block was placed on top of the TEG.

Figure 2.3a shows the data for four cycles of heating starting at ΔT = 10 °C and increasing to a temperature difference of 80 °C. The top side of the TEG was kept at room temperature (approximately 25 °C) for each test and the TEG surface temperature was tested using an infrared camera (FLIR C2, FLIR Systems Inc.) in between tests. The results indicated high voltage outputs that are well within the range needed for wearable electronics, even at lower temperature gradients. For example, the average voltage output for a 10 °C temperature difference was 59.96 mV. As shown in Figure 2.3a, increasing the temperature gradient between two sides of the soft TEG increases the output voltage. The generated voltage can reach more than 400 mV for temperature gradients in the range of 80 °C, which was the highest temperature gradient tested. Comparing this with other previous studies on flexible TEGs, this stretchable TEG exhibits much more robust voltage output at lower and higher temperature gradients, thereby expanding the applications for this technology. Relative to a previous work, our TEG exceeds these voltage outputs significantly with values of 0.6 mV at ΔT = 10 °C (ref [89]), 51.3 mV at ΔT = 19 °C (ref [91]), 19 mV at ΔT = 10 °C (ref [101]), 3 mV at ΔT = 20 °C (ref [102]), and 8.22 mV at ΔT = 30 °C (ref [103]). Moreover, the stretchable TEG presented here can be elastically strained, as described below.

In order to characterize the power generation capabilities of the LMEE TEG, the output voltage was measured across a varying external load resistor (R_{ext} = 1 to 100 Ω) for an

applied temperature gradient of 60 °C (Figure 2.3b). In this way, the current passing through the load resistor can be calculated and used for estimating the TEG power output in the impedance matching circuit[93, 109]. As shown in Figure 2.3b, the increase in external resistance corresponds to a sharp increase in voltage that began to level off as resistance increased well above 20 Ω. I observed that the increasing voltage soon converged with an open circuit voltage of 320 mV, that is circuits with high load resistance behave like an open circuit, as has been observed before[110]. As expected, the increase in resistance to 500 Ω corresponds to a high output voltage of 315 mV. Using these voltages and external resistances, R_{ext}, the power output is calculated as: $P = \frac{V^2}{R_{ext}}$. Referring to Figure 2.3c, the curve of this graph increases quickly and peaks at an external load of 11.5 Ω followed by a sharp drop in power as the resistance continues to increase. The TEG's maximum power for a 60 °C temperature gradient was 1.68 mW or 86.6 $\mu W cm^{-2}$ at the peak of 11 Ω, which corresponds to a voltage of 139 mV. Power per cm^2 of just the surface area of the semiconductors at this resistance was 0.857 mWcm^{-2}. The maximum power is predicted to correspond to the resistance when the internal resistance and the external load match [91, 28]. This is in reasonable agreement with the experimental measurement of the internal resistance of ~13.5 Ω at room temperature.

The internal resistance of these devices is controlled by three factors; the semiconductor resistance, the LMEE interconnect resistance, and the contact resistance between the semiconductors and interconnects. The device interconnect length was 5.48 mm with an average resistance of ~0.12 Ω. For 101 interconnects, this gives a total value of 11.8 Ω. This average measured interconnect resistance of ~0.12 Ω is comparable to the expected resistance value of 0.126 Ω for the same length based on the data from a previous work on LMEE electrical conductivity[104]. Likewise, ~7 mΩ was found to be the semiconductor resistance for one semiconductor, giving ~0.7 Ω for the 100 semiconductor array. Based on current semiconductor dimensions, the conductivity of these semiconductors is around 1.2 $\times 10^5 S m^{-1}$. These two values for resistance along with the overall resistance for the TEG of

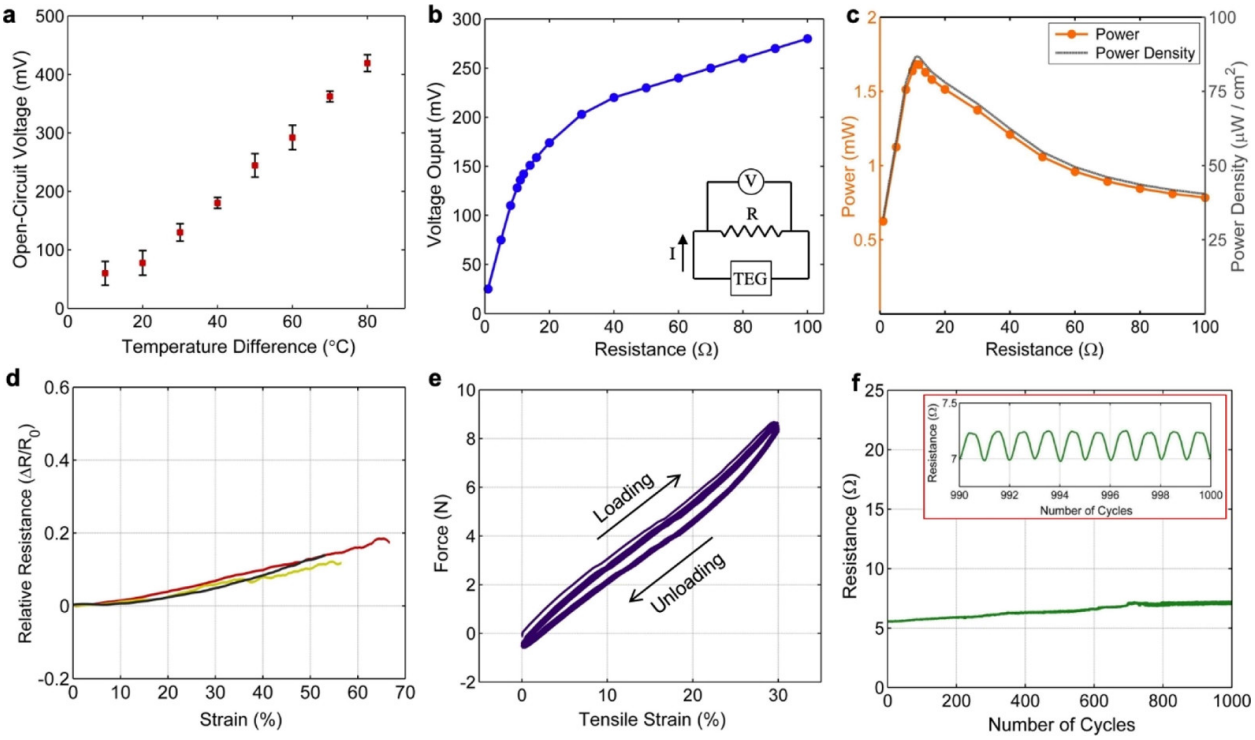

Figure 2.3: Energy harvesting and electromechanical characterization of stretchable TEGs.**a**, The open circuit voltage as a function of the temperature gradient on the top and bottom of the TEGs. **b**, The output voltage as a function of external resistor load for a temperature gradient of 60 °C. **c**, Estimated power and power density across the varying external resistor load for the 60 °C temperature difference. **d**, Change in relative resistance as a function of tensile strain for three representative stretchable TEG devices **e**, Hysteresis behavior of the soft-matter TEG under cyclic loading up to 1000 cycles. **f**, Measured electrical resistance of the stretchable TEG subjected to uniaxial cyclic loading with maximum strain of 30% for 1000 cycles; (inset: zoomed-in view for the last 10 cycles).

~13.5 Ω give enough information to determine an expected total contact resistance of ~1 Ω. While the resistances of commercially available TEGs are much lower, our value for device resistance is far less than or in the range with those reported in previous studies on flexible TEGs, with some research reporting resistances in the KΩ range[89, 90, 91, 92, 93, 101]. The value of contact resistance is observed to be less than a tenth of the interconnect resistance. This is because of the low contact resistance between EGaIn-sputtered semiconductors and EGaIn traces, considering EGaIn is often used to mitigate contact resistances and serve as an interconnect in electronic devices[111].

2.4 Electromechanical Characterization

2.4.1 Strain at Yield

To show that these devices can remain functional under mechanical deformation, I performed tensile tests using a universal load frame (Instron 5969). Tensile tests above 50% strain along with cyclic loading tests to 30% strain were conducted. The TEGs used for the tensile measurements share the same design architecture and fabrication process described above but consisted of two rows of nine semiconductors with electrically conductive fabric connectors coming out of each end instead of the previously described 100 semiconductor units (Figure 2.2h). With the Instron grips in place, these slender stretchable TEGs had a gauge length of 40 mm and a width and thickness of 12.6 and 2.8 mm, respectively. In the first set of tests, the tensile specimens of the TEG devices were strained until electrical failure (Figure 2.3d). Failure occurred at strains between 50 and 70%, highlighting the stretchability of the soft TEG and its ability to support significant deformation without electrical or mechanical failure. In particular, the patterned sections of the LMEE acting as the interconnects deform with the movement of the semiconductors and maintain their connection. It should be noted that the increase of the internal resistance in these TEG devices remains below 20%, which implies a stable electrical circuit for power generation.

As shown in Appendix A.1 and Figure A.1, using a simplified circuit model, we predict a power loss of less than 4% for stretchable TEGs when the deviation from initial internal resistance (matched with an external resistance) remains below 35%. This level of increase or decrease of internal resistance is an equivalent to $\Delta R = \pm 5\ \Omega$ for the fabricated TEGs with 100 semiconductors. Under the assumption of a fixed optimal load resistor, the generated power will decrease with the overall internal resistance changes because of the increase or decrease of resistance in the interconnects. The resistance change is attributed to a potential weakening/strengthening of the electrical contacts between the semiconductors and LMEE interconnects when the devices are bent, stretched, or compressed. While a variable external

load resistor can address this issue by matching to the new impedance, a 30% change in internal resistance will have only modest impact on the voltage and power output. This is highly advantageous for devices that may operate under harsh conditions and under strenuous mechanical loads.

The semiconductor elements are not attributed to the increase in resistance under strain as these are rigid components. In addition, a previous work has shown that there is a minimal resistance increase under strain for LMEE traces indicting that the increase in TEG resistance under strain is not from LMEE interconnects[40]. In addition, under cyclic loading, LMEE traces have also been shown to have only a small increase in resistance[104]. This leads to the contact resistance between the traces and semiconductors as the primary source of increased resistance under strain. As shown previously for our 100-semiconductor TEGs, there exists an overall internal resistance of ~13.5 Ω, of which ~1 Ω is attributed to internal contact resistance. Assuming a 12% resistance increase at 50% linear strain from Figure 2.3d, the internal resistance will be 15.1 Ω. Considering that the increase in interconnect and semiconductor resistance is minimal, this 1.6 Ω increase in resistance is attributed to contact resistance. This indicates that at a 50% strain, there is a 2.6 time increase in contact resistance. This is most likely coming from the changing morphology of the interconnects and displacement of rigid semiconductors under strain as the interconnects are thin and interfaced with semiconductors through a liquid interface. As mentioned previously, this increase in resistance at extreme strains only contributes to a 4% power loss when the deviation from the internal resistance stays below 35%.

2.4.2 Cyclical Loading

In order to evaluate long-term performance for applications in wearable electronics, the TEG was subjected to uniaxial cyclic loading of 30% strain for 1000 cycles. A 30% strain was selected as it is the maximum typical tensile load for skin, and can be used in this case as an extreme measure for wearable applications[98]. As shown in Figure 2.3e, there is a slight

amount of inelastic deformation with the first loading cycle, which I attribute to the Mullins effect, as has been previously shown for LMEE composites[24]. For subsequent loadings, the deformation is largely elastic, with only modest hysteresis between loading and unloading. Resistance increased as the number of cycles increased from a preloading resistance of ~5.7 to ~6.9 Ω (21% increase) after the 1000th 30% strain cycle (Figure 2.3f). Prior to loading, the stretchable TEG with only 18 semiconductors was able to generate ~30 mV at ΔT = 75 °C. For each individual cycle, electrical resistance increased as the load increased, following the path of cyclic loading (Figure 2.3f). In general, the lack of permanent mechanical deformation after loading, together with the continued electrical functionality of the device under significant tensile strain, attests to LMEE's excellent applicability to soft, conformal, and stretchable TEDs.

The semiconductors in these TEGs take up 10.1% of the total area fraction. However, an increase in this area fraction, also called the fill factor, has been shown to increase the power efficiency ($Wcm^{-2}K^{-2}$)[112]. For commercial TEGs, a fill factor of 30% is common. Based on the current fabrication techniques, there are no barriers to increase the fill percentages of semiconductors in these TEGs to reach such an area fraction. Using the current TEG dimensions, this would require ~300 semiconductors in a 15 by 15 grid embedded in the current sized devices. Assuming that the widths of the LMEE patterned interconnects remain the same, along with knowledge that the current parallel gap between the interconnects is ~3.17 mm, these updated devices would have parallel interconnect gaps of 2.11 mm. This is greater than the minimum of 2 mm previously reported to avoid shorting between EGaIn traces in the LMEEs[104]. Additionally, the lengths of the interconnect traces can be shortened to keep the distance between the ends of the interconnects above 2 mm to mitigate shorting and accommodate increased semiconductors per row.

2.5 Conclusion

This material architecture has the ability to be expanded far beyond these initial soft TEG devices, with future opportunities to explore the integration of LMEE-based TEGs into wearable technologies. I demonstrated that the TEG devices with a LMEE thermal interface are fully conformable to be wrapped comfortably on the body and deform around the curves of the arm. To increase power, voltage, and practicality, the size of these devices can be increased and customized to various parts of the body. In the future, larger version of these devices or devices with a denser arrangement of semiconductors could be engineered into an armband-style soft TEG that could self-adhere to the skin and be used to power wearable sensors and electronic devices. This would be an opportunity to exploit the unique elasticity of these devices in order to enable on-skin energy harvesting with wearable computing systems.

2.6 Lessons Learned

Stretchable TEGs capable of harvesting electrical energy from body heat under cold weather conditions have the potential to make wearable electronic and robotic systems more lightweight and portable by reducing their dependency on onboard batteries. However, progress depends on the integration of soft conductive materials for robust electrical wiring and thermal management. The use of thermally conductive soft elastomers is especially important for conforming to the body, absorbing body heat, and maintaining a temperature gradient between the two sides of the TEGs in order to generate power.

In this chapter a soft-matter TEG architecture composed of electrically and thermally conductive LMEE composites with integrated arrays of n-type and p-type Bi_2Te_3 semiconductors is introduced. The incorporation of a LMEE as a multifunctional encapsulating material allows for the seamless integration of 100 thermoelectric semiconductor elements into a simplified material layup that has a dimension of 41.0 × 47.3 × 3.0 mm. These stretchable TEDs generate voltages of 59.96 mV at Δ10 °C, 130 mV at Δ30 °C, and 278.6 mV

and a power of 86.6 $\mu W cm^{-2}$ at Δ60 °C. Moreover, they do not electrically or mechanically fail when stretched to strains above 50%, making them well-suited for energy harvesting in soft electronics and wearable computing applications.

While this chapter demonstrates a promising approach to soft TEDs, the design presented here is still limited by relatively low power output. Better thermal management is needed to decrease heat transfer across the semiconductors to obtain higher temperature differentials. A new manufacturing process needs to be developed with novel conductive inks to increase semiconductor density significantly to improve power output. Only by improving these aspects will TEGs be viable as a power source for wearable healthcare electronics. In the next chapter, I will show improved thermoelectric performance through 3D printed elastomer substrates along with integration of these TEDs into thermally responsive polymer actuators.

Chapter 3

Soft Thermoelectrics for Liquid Crystal Elastomer Actuation and Energy Harvesting

- **M. Zadan**, D. K. Patel, A. P. Sabelhaus, J. Liao, A. Wertz, L. Yao, and C. Majidi, "Liquid Crystal Elastomer with Integrated Soft Thermoelectrics for Shape Memory Actuation and Energy Harvesting", *Advanced Materials*, vol. 34, no. 23, 2200857, 2022.

3.1 Introduction

LCEs are a type of thermally responsive SMP that have both fluid-like and solid-like properties. These materials are made of rigid molecules, referred to as mesogens, enabling the liquid crystals to exhibit long range order in their nematic state [46]. As described in Chapter 1 Section 1.1.5, this allows for large shape deformations without mechanical failure. When heated above the nematic to isotropic transition temperature (T_{NI}), when a thermal stimulus is applied, the mesogens re-orient themselves into an isotropic state inducing a macroscopic contraction of the material as the material becomes an amorphous crystalline solid. Some advantages of LCEs over other shape memory materials is their large elastomer like stroke

length as well as their ability to be programmed to complex shape changes [60]. Cooling is still a major issue in LCE actuators, as passive cooling is slow. Introducing TEDs into LCE actuators, could enable active Peltier cooling while not impeding the actuation of the LCE.

3.1.1 Background on Liquid Crystal Elastomer Actuation Methods

There have been recent efforts to improve the speed and control of LCE actuators through novel methods of stimulation[113], though most of these introduce significant mechanical design challenges for robotics. Compared to external convection heating and Joule activation, a faster and more controlled LCE response can be achieved by pumping hot and cold fluid through embedded microfluidic channels[113] or by utilizing compressed air[70]. However, this leads to the need for bulky heating units and liquid pumps for actuation. Other approaches for actuating LCEs have included electromagnetic (EM) radiation, including visible[114, 115, 116], microwave[117], and infrared light (IR)[118]. However, these methods are unrealistic for robust autonomous robotic motion since the LCE must be in the range of directional EM emitters, which typically require a visual line of sight since the wavelengths in this range cannot penetrate opaque structures. Moreover, the emitted EM radiation does not usually enable the precision needed for controlled robotic actuation. Approaches with magnetic actuation have also been tried, but these require large external magnets and are susceptible to potential interference issues with the environment, such as metal around where the robot is navigating through[119]. Some of our recent work has focused on 2.4 GHz beam forming for non-line-of-sight targeted actuation [120, 121]. While promising, these approaches are still limited in their ability to enable robust and repeatable heating and cooling for controllable actuation. They also require large setups that would need to be moved to the location of operation, making them not compatible with lightweight mobile or wearable robotic devices.

A second challenge with LCE actuators is the low energy efficiencies associated with the existing methods of stimulation. Heating through Joule activation requires high input power

(≈1–10 W) over long periods of time (≈10–100 s) to heat LCEs above their nematic-to-isotropic transition temperatures[63, 70, 122]. Moreover, during intracycle cooling, this energy is lost through convection cooling. Likewise, although convection heating and EM-based actuation methods can increase actuation speeds, they are also susceptible to inefficiency on account of indiscriminately directing energy over large volumes[123]. These prohibitive properties make it difficult for LCE-based actuators to become viable options when compared to other actuation modalities. Moreover, such challenges are not limited to LCEs and are also observed in other thermally activated shape memory materials such as nickel–titanium shape memory alloys (SMAs), which suffer from low energy efficiencies of 1–2%[124]. A possible solution to increase the efficiency is recycling some of the otherwise-wasted thermal energy back into the actuator or host device. One of the future potentials and advantages of soft robotic systems is the ability to recover energy that is momentarily stored within soft materials and actuators that would otherwise go unused[72]. In the case of LCEs, the ability to recover energy from residual heat and thermal gradients could contribute to improved energy efficiency and longevity of the host electronic device or robotic system.

3.1.2 Thermoelectric Devices for Liquid Crystal Elastomer Actuation

In this chapter, I simultaneously address both challenges by combining LCEs with a thin thermoelectric layer that is soft, stretchable, and conforms to the LCE during deformation without impeding actuation. The thermoelectric device (TED) layer is composed of n-type and p-type bismuth telluride (Bi_2Te_3) microcubes that are wired together with eutectic gallium–indium (EGaIn) liquid metal interconnects and embedded within a 3D printed elastomer matrix (Figure 3.1a). This approach to create TEDs that are soft and elastic builds on recent research that has focused on combining Bi_2Te_3 with elastomers and liquid metals to create thermoelectric generators (TEGs) that are flexible and stretchable for wearable applications[95, 20, 125, 94, 103, 102, 126, 127]. Previous work has also shown

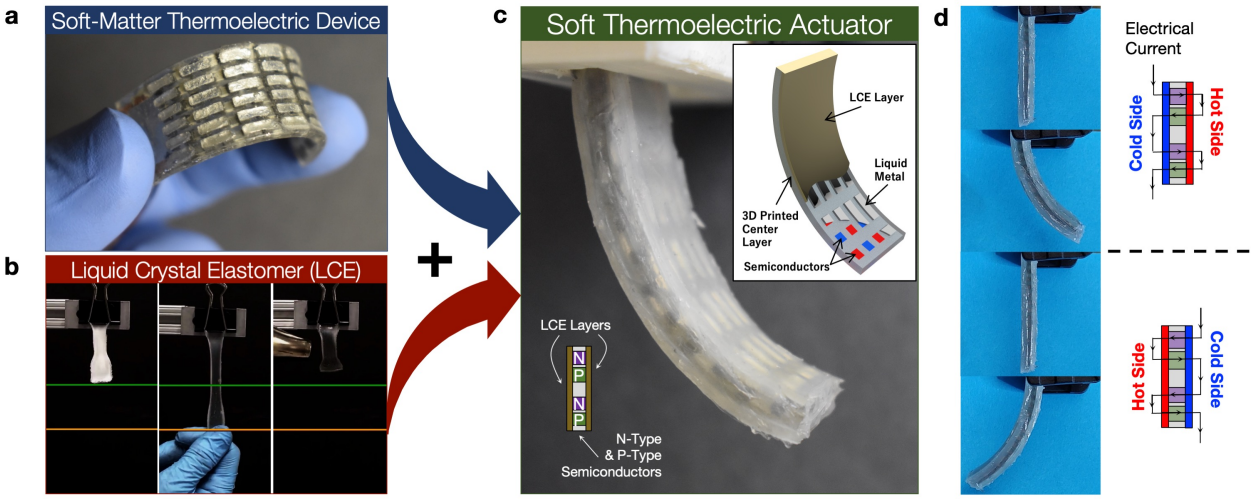

Figure 3.1: **a**, A stretchable 90 semiconductor soft-matter TED under deformation highlighting conformity of LM traces and 3D printed center layer. **b**, Images showing the responsiveness of the LCE shape memory polymer to heat. **c**, LCE-TED soft limb during actuation with right side heating and left side cooling. The inset represents a schematic diagram showing LM traces and semiconductors beneath the LCE layer. **d**, Images highlighting how the change in the current direction across semiconductors reverses the direction of actuation using only one input source.

that soft TEDs with integrated wavy-electronic copper interconnects are viable candidates for thermohaptic feedback in virtual reality[126, 127]. Here, I show that patterned liquid metal is similarly promising as interconnects within a soft TED architecture. Depending on the mode of operation, the soft TED functions as a Peltier heating/cooling device to control the contraction of the LCE layers or as an energy generator that uses the Seebeck effect to convert thermal gradients into electricity. In the Peltier mode, it can be used as thermal stimuli for LCEs, which exhibits the shape memory response presented in Figure 3.1b. This thermoelectric layer is then placed between two pre-strained pieces of LCE (Figure 3.1c). I term the final device an "LCE-TED." When current is applied across the leads of the soft TED, the right side of the LCE-TED transducer contracts as the LCE heats from Peltier heating that induces uniform bending of the transducer in the counterclockwise (CCW) direction. Reversing the flow of current causes the right side that was previously heating to subsequently actively cool and the left side of the device to heat up, resulting in bending in the clockwise (CW) direction (Figure 3.1d). By incorporating a soft and stretchable TED, both high and low temperatures can be applied to the LCE layers at the same time with only

one electrical input. By placing the TED in the center of the actuator, this ensures that heat is both being delivered effectively to the contracting side of the LCE as well as cooling the opposite side actively.

Through a series of soft robotics demonstrations, I demonstrate our design's potential to significantly improve the adoption of LCEs in practical applications. First, the closed-loop position control of our LCE-TED shows fast and accurate tracking due to active cooling. Prior applications of feedback in LCE-based robotic actuators are few and focus on sensing capabilities[65, 128]. Most are only proof-of-concept, are relatively slow, and either lack full pose feedback for the robot[58] or are nonspecific about the feedback procedure[70]. In each case, the lack of cooling (i.e., a negative control input) limits the ability to apply traditional control analysis techniques. Other types of antagonistic thermoelectric actuators can be modeled with a bidirectional control input; however, these require either careful techniques to avoid overheating[129], external cooling hardware[130], or highly advanced constitutive models[131]. Our device's tracking control demonstration, using a theoretically-grounded feedback procedure, overcomes each of these drawbacks.

Second, a soft robot built from two of our actuators shows the LCE-TED locomoting to a heat source and harvesting energy while stationary. Although simple in design, this two-limbed walker demonstrates the potential for creating soft robotic systems that can harvest some of their electrical power from energy in the environment. Lastly, to further increase voltage harvesting potential, I highlight the "physical intelligence" of this transducer to autonomously orient itself closer to a heat source, which allows for more electricity to be generated through the Seebeck effect. This feature is loosely inspired by phototropism, in which a plant responds and moves toward a light source. Together, these demonstrations show significant promise for robots built from soft LCE-TED actuators.

3.2 Liquid Crystal Elastomer Soft Transducer Fabrication

3.2.1 3D Printed Soft Thermoeletrics Fabrication

I fabricate the TED layer with an array of n- and p-type Bi_2Te_3 semiconducting chips that are wired in series using EGaIn liquid metal traces. The chips are embedded inside an elastomer matrix that is 3D printed using a Digital Light Processing (DLP) method and sealed with a UV curable ink[132]. As shown later, this soft TED enables the operation of both the Peltier and Seebeck effect and is mechanically compatible with layers of LCE placed on the top and bottom surface.

Figure B.1 depicts steps for device fabrication. The TEDs are made with a maximum of 90 semiconducting chips (1.4 × 1.4 × 1.6 mm) in six rows of 15 with overall active dimensions of 43.0 × 14.5 × 3.4 mm and a surface area fill of 28%. The center layer (53 × 14 × 1.6 mm), which acted as a substrate for the LM channels and semiconductors, was printed using a DLP 3D printer (Figure B.1-i). This 3D printing process was based on previous work by Patel et al. [132] The center layer consisted of 1 mm wide and 0.4 mm deep channels for LM interconnects and holes for semiconductors (Figure B.1-ii). The elastomeric resin used for 3D printing the center layer and sealing the LM traces comprises 49.02 wt% of epoxy aliphatic acrylate (EAA, Ebecryl 113, Allnex USA), 49.02% of aliphatic urethane acrylate (AUD, Ebecryl 8413, Allnex, USA) and 1.96% TPO (diphenyl(2,4,6-trimethylbenzoyl)phosphine oxide, Genocure TPO, RAHN USA Corp.) as the photoinitiator. TPO was dissolved in elastomeric monomers in a hot water bath at 86 °C. 3D printing was performed using a DLP-based 3D printer (PicoHD@27, Asiga). This printer was operated by a top-down DLP system with a digital mirror device (DMD) and a UV–LED light source operating at 385 nm. The printer was maintained at 40 °C during printing, and each layer was irradiated for 0.5 s, and layer thickness was 100 μm. The printed structures were sonicated with isopropyl alcohol (IPA) for 3 min to remove the uncured resin.

Depending on the desired configuration 44–90 1.4 × 1.4 × 1.6 mm 99.99% purity Bi_2Te_3 semiconductors (Wuhan Xinrong New Materials Co., Ltd.) were placed into 1 × 1 × 1.6 mm holes. This was followed by a post-curing in a UV chamber (CL-1000 Ultraviolet Crosslinker, UVP) for 3 min on each side to ensure a tight seal between substrate and semiconductors, mitigating LM shorting (Figure B.1-iii). A Stencil (polyester plastic McMaster-Carr) was then placed on the substrate, and EGaIn was airbrushed (Master G22) into the channels for 30 s (Figure B.1-iv,v). The device is then placed in a freezer at -30 °C solidifying the EGaIn traces below their melting temperature of 15.5 °C. The same UV curable ink used for the center layer was brushed onto the exposed LM traces using a paintbrush, covering them in a thin layer, and UV cured for 12 min at λ = 365 nm (Warson R838) (Figure B.1-vi). This process was repeated on the backside with thin copper tape leads being attached before airbrushing (Figure B.1-vii). More images of completed devices are available in Figure B.2.

Devices with 90 semiconductors were chosen for Peltier and Seebeck testing as this was the highest density of semiconductors that could be integrated without electrical shorting using our fabrication process. Increasing the semiconductor density increased energy-harvesting performance. Versions with 60 semiconductors that were evenly spaced were selected for transducer testing as they balanced heating uniformity and performance with flexural rigidity. Commercially available semiconductor pellets with dimensions of 1.4 × 1.4 × 1.6 mm were chosen because of their low aspect ratio, which reduced the mechanical impedance to actuator bending and allowed for a relatively low electrical resistance[133]. However, I do note that the low aspect ratio would result in less ability to maintain a temperature differential due to the flow of heat through the thickness of the device [133]. The overall footprint of 53 × 14.5 mm was selected for the center layer since this was the maximum build area that can be achieved with the DLP 3D printer that was used. I used this high length-to-width ratio in order for direct implementation into soft robotic limbs.

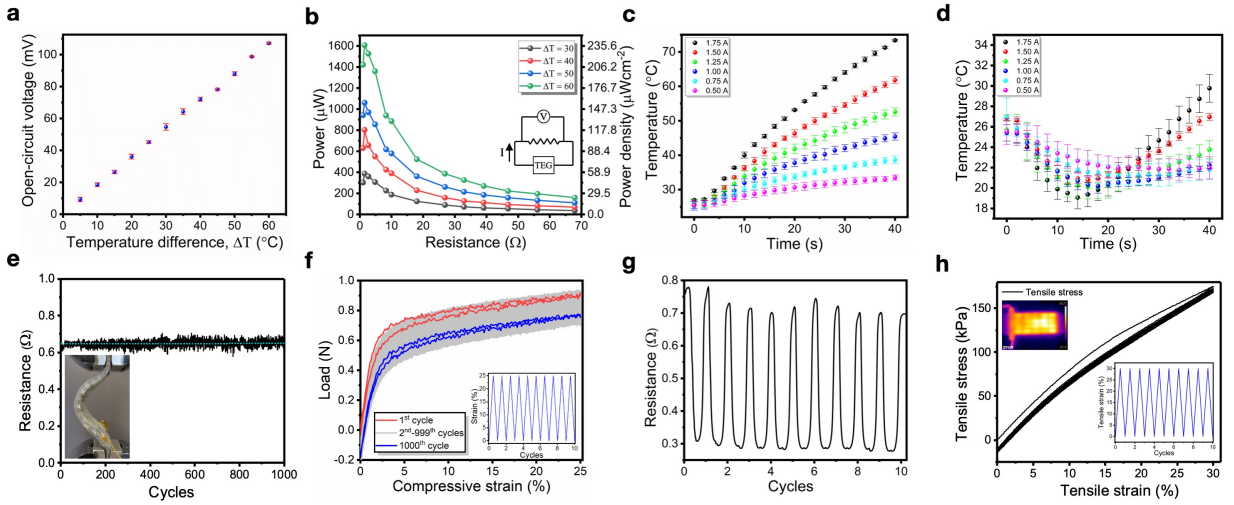

Figure 3.2: **a**, Temperature difference across a soft-matter TEG vs open-circuit voltage, confirming a linear relationship with a small error (n = 3). **b**, Resistance versus power and power density for varying temperature differentials. Inset: Circuit diagram for impedance matching. **c**, Time versus temperature for varying currents on the heating side of a 90 semiconductor TEG (n = 3). **d**, Time versus temperature for varying currents on the cooling side for a 90 semiconductor TEG (n = 3). **e**,Graph of change in resistance for 1000 cycles at 25% compression highlighting no mechanical or electrical failure. Inset: 44 semiconductor TEG at 25% compression in the universal load frame. **f**, Strain versus load for 1000 compressive cycles. **g**, Change in resistance for 10 cycles at 30% axial strain in the universal load frame. **h**, Stress–strain curve for ten cycles at 30% axial strain showing no mechanical failure or damage. The thermal inset shows 44 semiconductor TEG heating properly after cyclic loading.

3.2.2 Liquid Crystal Elastomer Transducer Fabrication

By placing photoinitiated pre-strained LCE onto each side of the TED, I can create a flexural actuator in which the opposing LCE layers are simultaneously heated and cooled. LCE fabrication was based on a process developed by Yakacki et al. [134]. For fabricating actuators, the LCE was pre-strained to 80%, UV cured, and adhered to each side of the TED (Figure 3.1c; Figure B.8).

LCE fabrication was based on work by Yakacki et al.[134] RM257 monomer (1,4-bis-[4-(3-acryloyloxypropyloxy)benzoyloxy]-2-methylbenzene) (10.957 g; Wilshire Technologies; 95%) was dissolved into 3.40 g toluene (Sigma–Aldrich) at 80 °C for 20 min. Once cooled for 5 min 3.076 g EDDET (2,2'-(ethylenedioxy)diethanethiol) (Sigma–Aldrich), 0.488 g PETMP (pentaerythritol tetrakis (3-mercaptopropionate)) (Sigma–Aldrich), 0.077 g HHMP

((2-hydroxyethoxy)-2-methylpropiophenone) (Sigma–Aldrich), and 0.038 g DPA (dipropylamine) (Sigma–Aldrich) were mixed into the monomer solution and vortexed mixed for 1 min [66]. The mixture was then degassed for 1 min and poured into 11 × 2 × 0.2 cm molds, with each mold creating enough LCE for one actuator. Samples oligomerize for 12 h at room temperature in a fume hood followed by 12 h in a vacuum oven (Across International) at 80 °C and 508 mm of Hg to evaporate the toluene. The LCE was uniaxially strained to 80%, and UV light (UVP, UVL-56 handheld UV lamp) was applied to crosslink for 30 min at 365 nm and 6 W, programming in a reversible prestrain of 39–45%. When pre-strained, the LCE strips were 1.1 mm thick and a 400 μm thick layer of Sil-poxy (Smooth-On) was then used to adhere the strips to each side of the TEG.

3.3 Seebeck Characterization

Open-circuit voltage data were collected for three cycles at room temperature with the TEG placed on a hot plate with a 200g mass ensuring even contact. Thermoelectric testing was conducted without the LCE layer to better understand the TEDs themselves. Peak voltage was recorded as temperature differentials can decrease quickly. Power data were recorded by measuring voltage in parallel to the external resistor from the circuit given in the inset of Figure 3.2b. The TEG was placed on a hot plate with a 200 g mass ensuring even contact. Maximum voltage in parallel was recorded for various resistor values. In between cycles, the TEG was cooled to ambient temperatures. For Peltier cycles, data were recorded for three passes for 40 s with a 90-semiconductor device being used. Temperatures were recorded using a thermal camera (FLIR C2) along with all tests being conducted at room temperature. The device was cool in between cycles.

Experimental measurements for energy harvesting through the Seebeck effect are presented in Figure 3.2a,b. The voltage V generated by a temperature difference ΔT is estimated as $V = n\alpha\Delta$T, where n is the number of n-type/p-type semiconductor pairs and α is the

Seebeck coefficient of the bismuth telluride [135]. Figure 3.2a shows the open-circuit voltage generated from changing temperature differentials across the TED. A linear relationship was found between temperature difference and voltage in line with the established relationship of $V = n\alpha\Delta T$. At ΔT = 30 and 60 °C, voltages of 54.7 ± 2.0 mV and 107.1 ± 0.7 mV was recorded as an increase in temperature corresponds to larger charge buildup across junctions. While voltages are low, they are in the range needed for voltage boosting to power small microcontrollers (LTC3108 Analog Devices).

By impedance matching the internal resistance of the thermocouple arrays with an external resistor, power (P) can be optimized for the highest possible power output when the device is in contact with a heat source [136]. Figure 3.2b inset gives a diagram of the TEG and external resistor in parallel with a multimeter setup recording the voltage output. By recording voltage output (V_{TEG}) and varying the external resistance (Rext) the power output is determined by

$$P = \frac{V_{TEG}^2}{R_{ext}}$$

Figure 3.2b gives external resistance vs power and power density for temperature differentials of ΔT = 30–60 °C. Peak power was recorded at an external resistance of 1.5 Ω, which is in line with the recorded internal resistance at room temperature of ≈ 1.5Ω, indicating that impedance matching is taking place as expected. At ΔT = 60 °C, max. power of 1.61 mW and $236\mu W cm^{-2}$ was recorded, which corresponds to a 32.7 mA current (Figure B.3). This is a ≈2.75 power density increase over previous work at the same temperature differential [20].

When resistance is plotted against voltage (Figure B.4), an increase in external resistance corresponds to a sharp increase followed by leveling off of voltage when $R_{ext} \approx 10\Omega$. Voltages begin to approach open-circuit voltage at these higher resistor values as the impedance increases. For instance, at ΔT = 60 °C $V_{oc} = 107.1 \pm 0.7mV$ (Figure 3.2a) and with an external resistance of 67.9 Ω, a similar voltage of 104 mV was recorded (Figure B.4). This has been shown before as an increase in impedance from the external parallel resistor leads to a voltage output approaching an open-circuit voltage [20]. In this case, voltage saturates at an

external resistance of around an order of magnitude above internal resistance.

3.3.1 Peltier Characterization

Characterization of the Peltier effect for voltage-controlled heating/cooling is presented in Figure 3.2c,d. By applying a current across thermocouples in series, temperature differentials are created at the junctions as the thermocouple alternates from forward bias to reverse bias. This Peltier effect allows us to create the uniform and fast heating and cooling that is needed to give effective heat output and absorption to the LCE surrounding the actuators. To better understand these characteristics, the Peltier effect for LCE actuation was characterized by recording heating and cooling curves for the TEDs at varying currents. Increasing current increases the rate of temperature increase for heating curves as expected (Figure 3.2c). At 1.75 A, the TED generated 73.4 ± 0.3 °C at 40 s (Figure B.5a) with a power draw of 5.5 W, while at the lower current of 0.5 A at 40 s with a power draw of 0.4 W, the heat generated was 33.5 ± 0.8 °C with a leveling off of temperature increase in this time range.

While an increase in current corresponded to an increase in temperature, the relationship between cooling and current was much more complex. As there is no thermal management or heat sink used during these tests, heat tends to bleed across the 3D center layer. This is seen from the cooling data (1.75 A; Figure 3.2d) as the temperature drops quickly initially from an initial temperature of 25.6 ± 1.0 °C to 19.1 ± 1.1 °C at 14 s (Figure B.5b), followed by a sharp increase to 29.8 ± 1.4 °C at 40 s giving the maximum cooling effect of 6.5 °C. Having a local minimum followed by a sharp temperature increase is less prominent in lower currents where less heat is generated on the opposite ends of the semiconductors with less energy transferring as quickly across. At 0.5 A, the cooling side is 22.7 ± 1.2 °C at 14 s and 22.0 ± 1.1 °C at 40 s with both values within the standard error of each other. This needs to be considered when actively cooling the TEGs as too high of a current will not necessarily lead to a lower temperature. Recent work by Jung et al. has identified underwater applications as a means to improve device performance [137]. Jung et al. showed that using water in

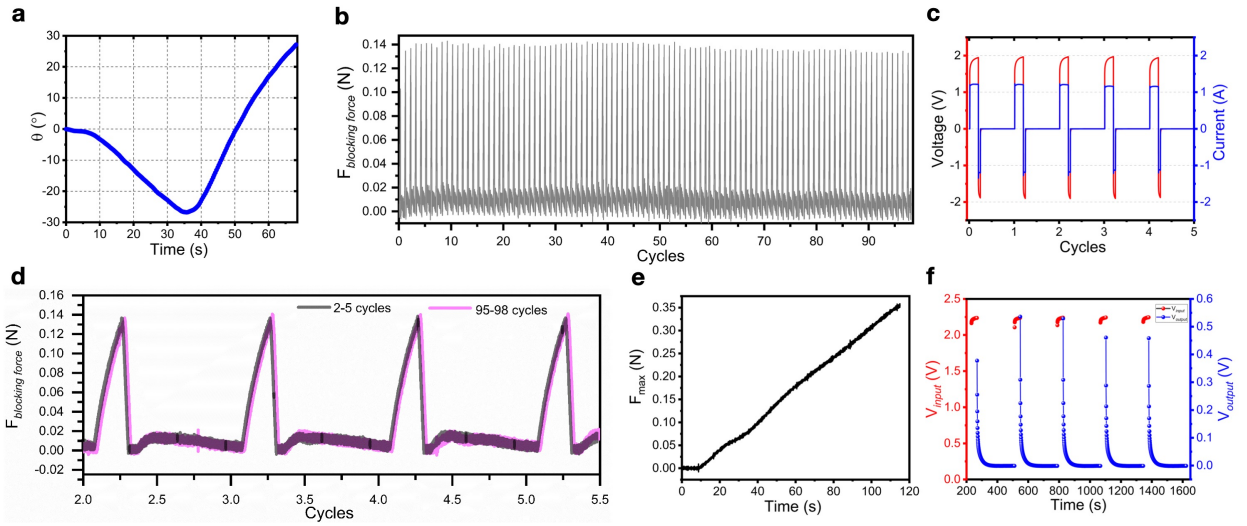

Figure 3.3: **a**, Measurement of time versus stroke angle for a soft-matter actuator running at 2.9 V followed by -2.9 V. **b**, 99 cycle blocking force test at 1.7 V highlighting robustness and stability of actuator. **c**, Voltage and current values for five representative cycles for the blocking force test. **d**, Comparison of cycles 2–5 and 95–98 highlighting high stability and no mechanical or electrical damage during a high cycle load. **e**, Maximum blocking force test of time versus force at 2.9 V to determine a max. force at break of 0.35 N. **f**, Comparison of voltage inputted during actuation through the Peltier effect (red) and voltage outputted through the Seebeck effect during cooldown cycles (blue), highlighting regenerative energy recycling.

contact with the TED as a heat sink led to an improvement in thermoelectric performance. To account for a wide range of operating environments and varying environmental temperature fluctuations, I conducted tests in a water environment. By operating the soft TED in water, I found no influence on heating behavior but did observe limited improvement in cooling performance (Figures B.6-B.7).

3.4 Electromechanical Characterization

In order to confirm that the thermoelectric layer could perform effectively under the stresses of repeated use as actuators and energy harvesters without degrading electrically or mechanically, cyclical bending and axial strain tests were conducted. All force and cyclical loading tests were conducted in a universal load frame (Instron 5969). Mechanical tests were run on a 44 semiconductor TEG modified to accept clamps for the universal load frame. Figure

3.2e gives internal resistance data for 1000 cycles at 25% compression, with the dotted line representing the value of initial resistance. The data showed excellent stability for use in actuators during bending. An image of the device in the compressed state is given in the inset. After 1000 cycles, no mechanical or electrical failure was observed.

In addition, no significant increase in resistance was found after 1000 cycles indicating the 3D printed polymer center layer and LM traces are deforming without effecting contact resistance with the semiconductors during actuation. Under these loading conditions, plastic deformation occurs with changes in stress–strain curves between the first (red) and 1000th (blue) cycles (Figure 3.2f). It is also unclear why the load of the final cycle is higher than the lowest sets of cycles in the grayed-out region. Hysteresis was shown to occur intracycle as expected but in no way impacting actuator performance.

During operation in a soft actuator or robotic system, these TEDs will exhibit very little to no axial strain. Nonetheless, I demonstrate the ability of the soft TED to be cyclically loaded to 30% uniaxial strain for 10 cycles (Figure 3.2g). Resistance dropped from $\approx 0.7\Omega$ at 0% strain to $\approx 0.3\Omega$ at 30% strain. No damage or trends in resistance were detected during these tests. In addition, no mechanical or electrical failure occurred. This decrease in resistance could be caused by a decrease in contact resistance between semiconductors and LM traces from transverse compression during axial loading. This should not be an issue for the actuators as very little axial strain occurs during actuation. After the test was completed, the voltage was applied across the terminals of the device. The device functioned well with no semiconductors failing to generate heat (Figure 3.2h thermal inset). Mechanical stability was observed after the first cycle of axial loading, as seen in Figure 3.2h. There is limited hysteresis during loading for the other nine cycles showing mechanical stability of the 3D printed components under extreme conditions.

3.5 Soft Robotic Actuator Characterization

Actuator angle and force output were characterized to better highlight the actuator characteristics and inform controls and robotic applications given in the next section. Results indicated that these actuators have a high angle of stroke, can generate significant force for an actuator made of soft components, and repeatedly and controllably deliver that same force output as a function of time cyclically for a high number of repetitions. As opposed to Joule-heated actuators with one direction of motion per voltage input, these TED actuated soft muscles can operate in positive and negative angular domains above and below zero degrees bending angle using only one input.

3.5.1 Characterization of Actuator Bending

By reversing the input voltage from positive to negative, the actuator can both actively heat and cool the opposing surfaces at the same time, reversing the direction of actuation. A representative cycle is shown in Figure 3.1d, with time vs angle results shown in Figure 3.3a. With a positive voltage of 2.9 V applied followed by -2.9 V, max. angles of 27° and -27° are reported. The maximum angular velocity recorded during testing was 2.5° s^{-1} (Figure B.9). The ratio of time from 0° to 27° and 27° back to 0° is 1:0.43 for one cycle. This multidirectional actuation and active cooling is an order of magnitude faster compared to actuation cycles (1:10) of previous single input Joule-heated actuators that require ambient air cooling [58]. As there is a defined relationship between temperature and contraction [134], these actuators operate better when running warm. This explains the steeper slope in actuation in the negative direction when the negative voltage is applied. The LCE has already warmed up due to some thermal bleeding from the heated side onto the cooling side, as seen in Figure 3.2d. This, along with stored elastic potential energy, accounts for the faster actuation upon voltage reversal. The first of the 99 blocking force cycles in Figure 3.3b also highlights this characteristic as the initial cycle is the only force output that varies significantly from the

others and represents a warmup cycle.

3.5.2 Force Output

Figure 3.3b shows a plot of time vs force output for the LCE actuator blocking force test for 99 cycles. Blocking force tests were performed on a 60 semiconductor actuator with a 10 N load cell placed right above, with the actuator placed parallel to the ground. The LCE-TED actuated into the load cell, determining force output. An Arduino microcontroller and power source along with an H-bridge of power MOSFETs were used to switch current directions for the blocking force test. Using the H-bridge circuit, the device was actuated for 95 s at 1.7 V into the load cell, 22 s at -1.7 V in reverse until a 0° angle, and 380 s of cooling time at 0 V for 99 cycles. Figure 3.3c graphs time vs voltage and current for five representative cycles. While power source voltage is constant along with current, the voltage across the actuator varies from 1.5-2.0 to -1.5 to -2.0 V to 0 V per cycle as varying semiconductor resistances inside the device and across the pins of the H-bridge metal–oxide–semiconductor field-effect transistors (MOSFETs) (used to reverse current directions) effect voltage. With an average max. force output of 0.138 N and a small standard error of 0.003 N for 98 cycles, high repeatability, stability, and robustness are shown.

To highlight force output stability and consistency, cycles 2–5 are compared to cycles 95–98 in Figure 3.3d. These force output curves are almost identical with max. output along with heating and cooling slopes being indistinguishable between initial and final cycles. Intracycle, the importance of running these actuators “warm” for faster actuation is again shown as only 23% of the positive actuation time is required to return to zero bending angle. By running this actuator at a higher voltage of 3.2 V, I obtained a maximum force output of 0.35 N at break confirming high force output for a soft robotic muscle. By using thin LCE materials as well as low aspect ratio semiconductors, I were able to keep the second bending moment low in order to decrease flexural rigidity stiffness and achieve large bending curvatures. Compared to the commercially available 1.37 mm-diameter coiled nitinol shape

memory alloy wire (Flexinol, Dynalloy inc), the force outputs are comparable with a heating and cooling force output of 0.39 N and 0.17 N for Flexinol, respectively. By defining a figure of merit (FoM) for this device as $\frac{U_e}{U_e+U_t}$ where U_e is the elastic energy and U_t is the thermal energy [138], I determine an FoM of 0.0008 for one cycle at 3.2 V. Further information is given in the Appendix B.1 along with Figure B.10. Although low, this FoM is in line with other thermally driven soft actuators and can potentially be increased by altering the dimensions of the device layers [138].

3.5.3 Regenerative Energy Harvesting

In between actuation cycles, a portion of the heat applied to the system during Peltier heating can be converted back into voltage through the Seebeck effect. Much like electric car regenerative energy harvesting from induction motors during braking, in which induction motors double as energy harvesters when torque is applied to the motor, the LCE-TED actuators have similar characteristics through electrothermal instead of kinetic energy conversion. I introduce regenerative energy harvesting into a soft actuator as a proof of concept. I tested this unique characteristic for five cycles, inputting heat into the system through Peltier heating for 35 s at 2.2 V, followed by recording the voltage output during a 4 min cooldown as the actuator moved back to the rest position. Results are shown in Figure 3.3f, with the left y-axis showing voltage input and the right y-axis showing generated voltage. The maximum generated voltage of 0.53 V was recorded. Voltage drops quickly, and heat transfers across the system as it approaches a steady state. By analyzing one cycle at 2.7 V across the transducer for 50 s and 0 V for 6 min of energy harvesting (Figure B.11), I can determine the efficiency of applied vs generated energy to be η = 0.03%. For more details, see the “Regenerative Energy Harvesting Efficiency” section in Appendix B.2. While this efficiency is not high enough to increase the range of the actuator in a meaningful way, I introduce this as a proof of concept and hope it spurs further investigation of efficient energy recovery methods that can be used for soft actuators. Potential methods to improve

efficiency include decreasing the thermal resistance between the semiconductors and LCE layer to guarantee better contact before the temperature differential across the entire device degrades due to heat conduction. This unique feature introduces a new approach for more energy-efficient soft robotic actuators.

3.6 Actuator Demonstrations

3.6.1 Position-Controlled Actuation Demonstration

Contributions: I fabricated the actuators used in the PI demonstration and conducted PI control tests with Dr. Andrew Sabelhaus. Dr. Andrew Sabelhaus designed the experimental setup and control test bed, chose the controller, wrote the code, and tuned constants.

A position-control feedback test was performed to track deflections of the soft LCE-TED actuator, here considered to be a single-degree-of-freedom robot limb. The feedback control test used a hardware platform adapted from Patterson et al. [139] and Wertz et al. [129] The LCE-TED was clamped to a rigid frame, connected to an electronic circuit in an H-bridge configuration of power MOSFET transistors, and received positive or negative voltage via two pulse-width-modulation (PWM) signals. The nominal applied voltage across the device was calibrated to 2.9 V at the start of each test. A microcontroller changed the applied power by setting the positive/negative PWM duty cycle at time k, i.e., $u(k) \in [-1, 1]$, mapping negative duty cycles to the PWM connected to the "reverse" signal of the H-bridge. Two computer vision markers were placed on the test setup, one on the clamp and one at the tip of the actuator, so that a camera (Intel, Real Sense) measured the deflection angle of the soft limb ($\theta(k)$) in real time. Our control system takes a desired angle $\theta(k)$ and uses proportional-integral (PI) feedback to specify the PWM duty cycle as a function of the position error $e = \theta - \overline{\theta}$, i.e., $u(k) = k_p e(k) + \sum_{t=0}^{k} K_i e(t) \Delta t$ The controller gains K_p and K_i were estimated using various PI tuning rules from the literature. See Appendix B.3 for more specifics on electronics and control. The limb held alternating angles of + 5° or –5° for 50 s each (Figure

3.4a). This response was verified using two different soft limb prototypes that were tested with the same control system. Results show that the actuator can quickly switch between positive and negative angles (Figure 3.4b), as anticipated from the characterization tests. Even though the control system never applies the full 100 % duty cycle power (see Appendix B.3 for more discussion), the limb still reaches its desired angle after only ≈20 s. This would not be possible with passive cooling alone. The position error reaches <0.5° after settling, which is more than sufficient for most soft robotics applications [129].

3.6.2 Soft Walker Demonstration

Contributions: I designed the demonstrations and built the actuators. Dr. Jiahe Liao assisted in the design of the soft robotic walker demonstration along with aiding in data collection and processing.

To demonstrate the use of these transducers in a robotic system, I have developed an LCE-TED walker capable of walking toward a heat source and harvesting energy. The walker is composed of two LCE-TED limbs that are oriented 90° apart and connected at the ends. At the distal end where the limb makes contact with the ground, an angled and jagged copper shim is adhered in order to enable anisotropic friction [57, 140] and allow the walker to move in a forward direction. In its rest state, the device is 65 mm high and 92 mm wide. Each limb was actuated with a 3.0 V power source. The actuation times were left limb +3 V, right limb -3 V for 45 s, then left limb 0 V, Right limb +3 V for 10 s, followed by a cool-down period of ≈6:30. By reversing the voltage direction during actuation, I induced forward movement as the limbs contracted and expanded, first pulling together and then pushing apart. Additional gait information is given in the Experimental Section. Figure 3.4c presents images of a representative gait cycle.

The task planned for this robot was to move itself over to an energy source, in this case, a heat lamp, and generate continuous electricity. Distance between the limb and energy source is key to overcoming the heat loss of air's low thermal conductivity. Initially, I recorded the

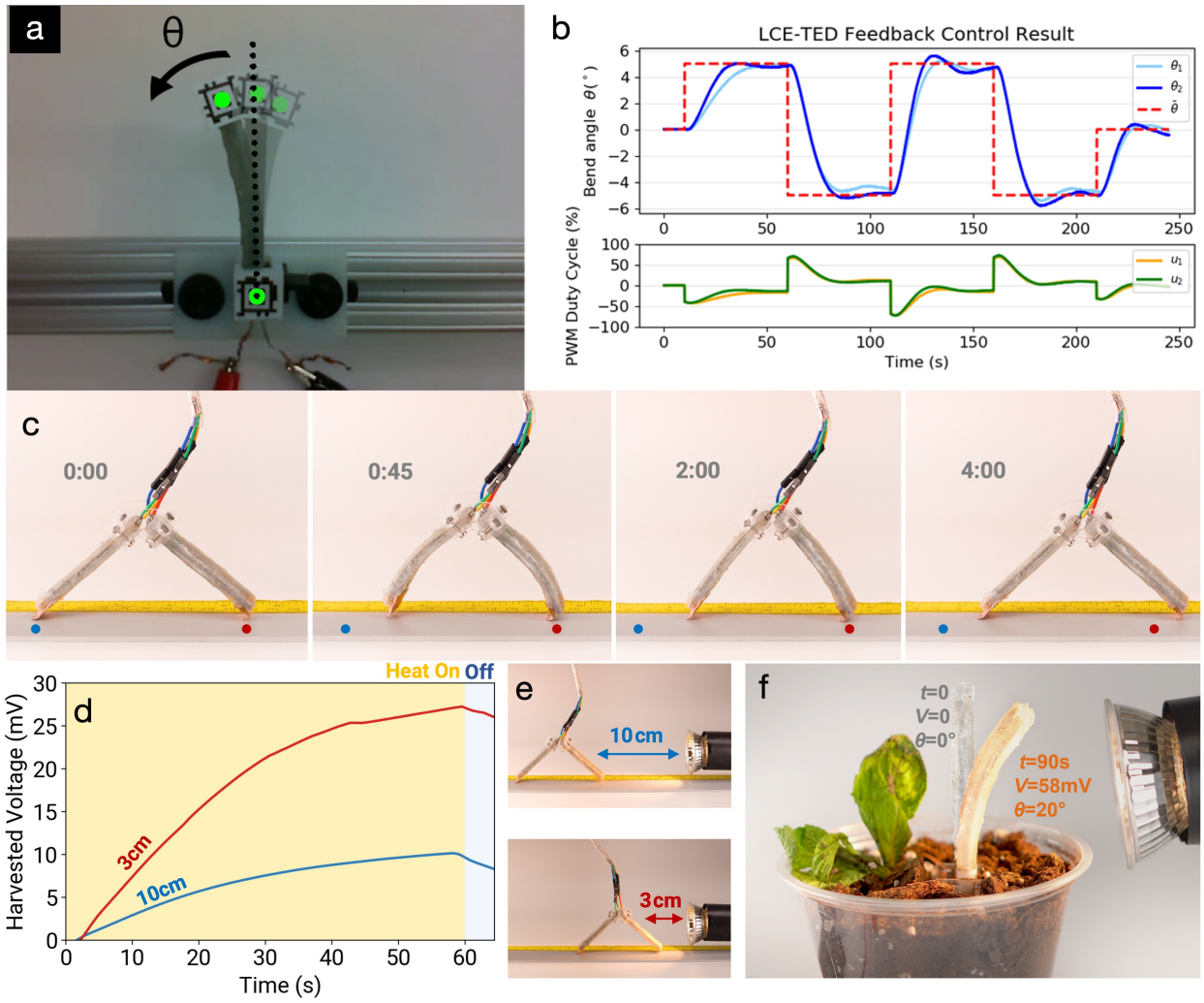

Figure 3.4: **a-b**, Position control test of LCE-TED actuator prototypes. **a**, The target robot limb pose is specified as a deflection angle, measured using a computer vision system. **b**, Feedback control demonstrates low-error tracking of deflection angle, verified on two different actuator prototypes (1 and 2). **c-e**, Walker demonstration of LCE-TED actuators. **c**, Gait mechanics for one gait cycle of the two-legged soft walker. **d**, Graph of energy harvesting from the front limb at the initial and final positions of the soft walker, highlighting the walker's ability to move over to a power source and passively generate voltage during hibernation. **e**, Images of initial vs final position away from the energy source corresponding to (d). **f**, Image of an LCE limb exhibiting physical intelligence as it tracks toward a heat source and increases the harvested voltage

voltage output of the front limb at a distance of 10 cm away from the heat source. The walker then actuated over to the heat source in order to record a higher voltage output (Figure B.12). After re-recording the voltage, I found a much higher voltage output when the limb is closer at 3 cm to the heat lamp (Figure 3.4d,e). When reaching the heat source, the soft walker

enters a "hibernation" state; during that time, it can generate power indefinitely from a heat source. I also found that as the limb generated voltage, the limb closest to the heat lamp begins to heat up and actuates in response to the ambient heating. This limb bending causes the walker to pull even closer to the heat lamp (Supporting Information).

3.6.3 Phototropism-Inspired Energy-Harvesting Demonstration

For the soft walker demonstration, I observed that the limb closest to the heat source would bend in response to the ambient heating and pull the walker closer to the heat lamp. From this, I infer a passive "physical intelligence" of the transducer by which it will autonomously move toward the energy source [141]. This effect, which loosely resembles phototropism and heliotracking SMPs [141, 142], is further examined with the demonstration presented in Figure 3.4f. By placing a soft limb vertically near a heat source and applying no voltage to the limb, I see the soft transducer autonomously sense and bend toward the heat source (Figure B.13). Bending decreases the distance between the thermoelectric layer and the heat source, which can cause an increase in the amount of electricity that is generated (Figure B.14). When the heat source is turned off, the voltage and angle decrease as the limb moves away from the heat source and returns to its naturally straight configuration (Supporting Information). Comparison tests were conducted with and without the LCE layer in which the heat source is placed adjacent to the base of the actuator and oriented so that heat is directed upwards (parallel to the actuator). These measurements show an improvement in voltage output when LCE is incorporated into the limb. This is because LCE actuation will cause the limb to autonomously bend toward the heat source and experience a larger surface area over the heat source leading to a larger temperature differential. Unlike the LCE-integrated limb, the passive limb does not bend and exhibits a voltage output plateau of 10 mV after 50 s of exposure to the heat source. In contrast, the autonomously responsive limb with LCE exhibited a greater than 2× voltage output with a maximum voltage output of 22 mV (Figure B.14). This energy-harvesting demonstration shows the physical intelligence of the

LCE-thermoelectric transducer and suggests the potential for future soft robotic systems to generate energy from their surroundings in between actuation cycles or during periods of hibernation (e.g., sleep mode) or low-power operations.

3.7 Conclusion

This work has demonstrated the use of a deformable, 3D printed TED in LCE actuators to enable both active heating and cooling of LCEs along with energy harvesting. By controlling heating and cooling actively, multidirectional actuation can be controlled with one input improving actuation times over ambient cooling by an order of magnitude. With both heating and cooling, we have shown a practical feedback control example, with a rapid bidirectional response and no external cooling hardware, suitable for integration into soft robots.

Additionally, this work has introduced the concept of soft actuators with intrinsic energy-harvesting capabilities for environmental energy harvesting along with regenerative thermal recycling. The latter allows for the recycling of otherwise wasted thermal energy and is analogous to regenerative braking used in induction motors for electric vehicles. By exploiting temperature gradients in nature or by exploiting internal temperature differentials between the LCE layers, the Seebeck effect converts thermal energy into electricity that can be used for subsequent actuation cycles. I highlight the potential of LCE-TED actuators in a tethered two-legged-walker demonstration in which the walker moves to a heat source to generate voltage. Lastly, these limbs demonstrate a form of physical intelligence in their ability to autonomously reconfigure themselves to increase the amount of energy harvested from an external heat source.

Future areas of improvement and current limitations center around thermal management. These actuators still require a prolonged cool down time in between cycles that can take over 3× the actuation time at low voltages (Figure 3.3b) and up to 6.5× when larger activation voltages are used. Each LCE sheet of the LCE-TED limb is not independent of the other,

with heat transferring across the 3D printed elastomer separation layer during prolonged actuation. This can lead to heat saturation within the actuator due to poor heat transfer through convection cooling and can produce high stresses at both interfaces, leading to delamination from the TED layer. One solution is increasing the bonding strength without increasing structural rigidity through stronger adhesives. Separately, decreasing thermal conductivity between the LCE sheets by taking full advantage of 3D printing for creating thermally insulating metamaterials may be another promising direction.

3.7.1 Limitations

While these approaches would allow the LCE-TED-based limbs to operate for longer cycles, they do not address the intercycle cooldown time limitations. For this, the focus must be shifted to a new generation of high thermal conductivity deformable heat sinks to aid in convective cooling. Liquid metal embedded elastomer (LMEE) composites have been shown to have high mechanical compliance along with high thermal conductivities [24]. Previous work has shown LMEE composite's potential in TED-based systems for thermal management[143, 28].Further efforts to incorporate such material architectures and manufacturing methods could lead to additional improvements in LCE-TED performance. Lastly, I see the potential for future work in the integration of these transducers into a soft robot to realize the potential of LCE-TED limbs more fully. Untethered soft robotic platforms such as those explored by Patterson et al. [139] are a potential candidate to more fully develop the energy harvesting and controls potential introduced here.

3.8 Lessons Learned

LCEs have attracted tremendous interest as actuators for soft robotics due to their mechanical and shape memory properties. However, LCE actuators typically respond to thermal stimulation through active Joule heating and passive cooling, which make them difficult to control. In

this chapter, LCEs are combined with soft, stretchable thermoelectrics to create transducers capable of electrically controlled actuation, active cooling, and thermal-to-electrical energy conversion. The thermoelectric layers are composed of semiconductors embedded within a 3D printed elastomer matrix and wired together with eutectic gallium–indium (EGaIn) liquid metal interconnects. This layer is covered on both sides with LCE, which alternately heats and cools to achieve cyclical bending actuation in response to voltage-controlled Peltier activation. Moreover, the thermoelectric layer can harvest energy from thermal gradients between the two LCE layers through the Seebeck effect, allowing for regenerative energy harvesting. As demonstrations, first, closed-loop control of the transducer is performed to rapidly track a changing actuator position. Second, a soft robotic walker that is capable of walking toward a heat source and harvesting energy is introduced. Lastly, phototropic-inspired autonomous deflection of the limbs toward a heat source is shown, demonstrating an additional method to increase energy recuperation efficiency for soft systems.

The concepts introduced in this chapter introduce a new direction for soft robotic actuators with embedded energy harvesting abilities and thermoelectric cooling. However, the TEDs introduced here do not have power densities sufficiently high enough to operate wearable health monitoring electronics such as PPG wearables, a goal of this thesis. To improve performance, better heat transfer is needed along with a improvements in semiconductor fill density. The next chapter will introduce how improved materials can enable this.

Chapter 4

Wearable Thermoelectric Generators for Self-Powered Medical Sensing

- **M. Zadan**, A. Wertz, D. Shah, D. K. Patel, W. Zu, Y. Han, J. Gelorme, H. J. Mea, L. Yao, M. H. Malakooti, S. H. Ko, N. Kazem, and C. Majidi, "Stretchable Thermoelectric Generators for Self-Powered Wearable Health Monitoring", *Advanced Functional Materials*, 2404861, 2024.

4.1 Introduction

In the previous chapters, the development of stretchable TEDs have been introduced with a focus on materials improvements including LMEE and LM interconnects to increase power output without sacrificing mechanical compliance. The testing for these devices has been exclusively conducted on laboratory bench-top setups for power output characterization. This gives precise values for power characterization at set temperature differential. The question still remains as to what the temperature differentials are that actually exist in field environments, namely when worn indoors or outdoors with environmental conditions at play. This is not currently understood. How environmental conditions effect performance and how much power improvement is needed to power battery-free health monitoring systems is still

an open question that I will address in this chapter.

Portable, wearable electronics for physiological monitoring, in contrast to their tethered counterparts in clinical settings, increasingly require larger power sources to support greater computational, sensing, and communication demands over long durations of continuous or frequent monitoring. Potential routes to address this problem include incorporating large batteries or requiring frequent recharging, which may become impractical for long term monitoring, especially for devices that are difficult to reach, remove, or reapply. An alternative route is to incorporate on-body energy harvesting to extend operational durations between battery recharging cycles and potentially eliminate the need for a battery all together. Such an approach requires wearable generators that are highly miniaturized or sufficiently soft and flexible to be worn on the body without interfering with natural motion. Recent research has developed methods for harvesting biomechanical energy through piezoelectric, triboelectric, and dieletric energy conversion methods, along with body heat through thermoelectric energy conversion [125, 144, 7, 145, 146].

Thermoelectric devices (TED)[45, 147] are especially promising due to their ability to harvest energy under a wide range of conditions, including for indoor, outdoor, active, and sedentary activities. TEDs operate on two main principles, the Seebeck and Peltier effects. In the Seebeck effect, a thermal gradient is applied across the semiconductor junctions of two oppositely doped semiconductors, inducing a current which can be used for energy harvesting. Conversely, the Peltier effect occurs when a voltage is applied across the semiconductor junctions inducing a temperature differential and enabling solid state cooling [148]. However, for TEDs to be seamlessly integrated into wearables, they must be elastically compliant in order to conform to the body, moderately stretchable so that they do not interfere with the user's natural mechanics, and sufficiently soft so that they can mechanically interface with skin without introducing air gaps or stress concentrations that could result in high thermal resistance or skin discomfort [149, 150, 93, 102, 151, 103]. To accomplish this, progress depends on a new class of soft high-performance materials to match or exceed the energy

harvesting performance of rigid TEDs while presenting minimal mechanical resistance to elastic deformation to ensure comfort and effective heat transfer [125].

Recent TEG research has focused on improving interconnects and thermal interface materials (TIM) for improving device performance. To replace traditional rigid copper interconnects, flexible and wavy copper[150, 93, 152, 94, 153], liquid metals (LM)[102, 103, 154, 155], and LM-based composite materials [156] have been introduced. Methods based on rigid metals like copper are highly promising but potentially suffer from limitations due to their intrinsic mechanical stiffness, which can lead to localized stress concentrations and may require complex manufacturing methods and geometries to achieve effective mechanical compliance at the meso/macroscale [157, 158]. Likewise, microfluidic channels of LM alloys like eutectic gallium indium (EGaIn) embedded within a soft elastomer allow for improved mechanical performance but can be prone to leaking and subsequent electrical short-circuiting during fabrication, lowering the potential for high semiconductor packing densities [103]. To overcome these limitations, a promising alternative is to use percolating networks of LM droplets embedded within a soft elastomer. In contrast to microfluidic channels of bulk liquid metal, these LM-embedded elastomer (LMEE) composites support high electrical conductivity that remains stable under extreme strain and are significantly less prone to leakage due to the robust encapsulation of LM droplets withing the surrounding polymer [159, 160]. Moreover, LMEEs can also be engineered to be electrically insulating and function as a high performance thermal interface material (TIM) to decrease the thermal resistance between the semiconductors within the TED and interfaces to the body and surrounding environment. LMEEs have previously been implemented as a TIM and heat sink for TEDs [20, 133, 161, 162], although researchers in the past have also explored other materials for thermal management including radiative absorbing materials [163], flexible phase change materials [164], graphene nano-platelets [22], Ag-Ni aligned networks [165], Ag and CNT-embedded elastomers [93], and fin based soft heat sinks [156, 161, 166]. Nonetheless, in spite of such advancements, the thermal conductivities of TIMs used in TEDs have been

reported to be at most ~ $1.1 W m^{-1} K^{-1}$, therefore representing another potential area for improvement.

Building on these material architectures, there have been several attempts in recent years to incorporate TEDs into wearable electronics to power health monitoring sensors. However, these demonstrations have largely focused on small-scale low-power implementations. Examples include implementations that perform temperature and humidity measurements on a flexible polyimide substrate TEG[167], ECG measurements [95, 153], a three-axis accelerometer[168], gyroscope measurements, and Bluetooth transmission[169]. However, there still remains to be demonstrated a mechanically soft and wearable TEG that can power a more energy-intensive physiological sensing capability like photoplethysmography (PPG), which is used to capture health vitals like heart rate and SpO2 blood oxygenation. Achieving photonic sensing in a battery-free wearable device that is also capable of energy storage, signal processing, and wireless transmission remains a key remaining challenge in the field [144].

In this work, I address this critical need by introducing a new framework to design battery-free wearable electronics that are capable of photonic-based physiological monitoring and fully powered using body heat. Each element of the system design has been selected to achieve high mechanical and thermoelectric performance along with seamless materials integration. This is accomplished through a comprehensive design and manufacturing framework that includes advancements in soft-matter material architectures, TEG array design, low energy circuit board design, and on-board power management (Figure 4.1). The devices comprise a high-aspect-ratio 3D printed elastomer matrix for mechanical compliance and high semiconductor fill factor, an elastomeric LM-epoxy composite for enhanced thermal conductivity between the TED and contacting surfaces, and an LM-Ag-SIS elastomer ink composite for mechanically robust electrical connectivity between Bi_2Te_3 thermoelectric semiconductor elements. Compared to past work with LM-based soft TEG architectures,

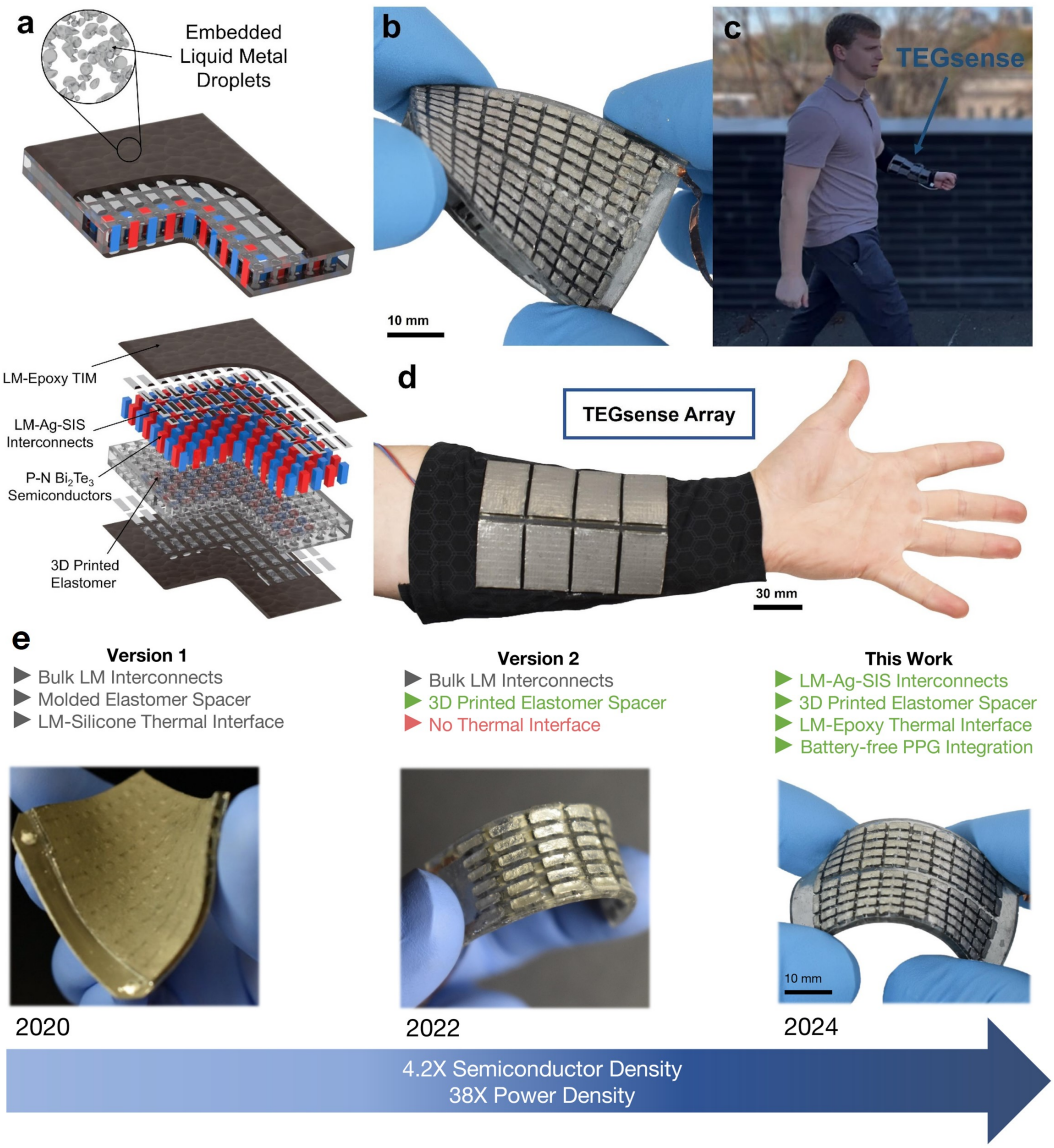

Figure 4.1: Design and overview of wearable thermoelectric device. **a**, TEG Schematic showing the key components of soft thermal interface materials, LM-Ag-SIS stretchable conductive inks, Bi_2Te_3 semiconductors, and 3D printed elastomer matrix. **b**, Image of TEG in flexure highlighting high semiconductor density of LM-Ag-SIS inks. **c**, Image of TEGsense being worn on the arm during operation. **d**, Image of TEGsense array made from 8 HA-HD + LM-epoxy TEGs. **e**, Design and performance comparison of previous stretchable TEG works. Reproduced with permission. [20] Copyright 2020, American Chemical Society. Reproduced with permission. [151] Copyright 2022, Wiley-VCH.

this approach allows for greater freedom in semiconductor densities and aspect ratio of the semiconductors. Moreover, it incorporates a stretchable LM-epoxy composite with the highest recorded thermal conductivity ($2.90 \pm 0.02 W m^{-1} K^{-1}$) of any TIM used for a wearable TEG. A

variety of soft TEGs were implemented using this general design framework and compared across their Seebeck, Peltier, and electromechanical properties. In particular, Seebeck, Peltier, and electromechanical performance was compared for semiconductor densities of 40% vs 22%, the incorporation of the stretchable LM-epoxy composite vs a non-thermally conductive epoxy, and the use of high-aspect ratio semiconductors (4:1.4) vs low-aspect ratio semiconductors (1.6:1.4) for heat transfer performance. This novel device framework, enabled by the material architectures introduced herein, produces TEGs that achieve the goal of combining mechanical compliance and elasticity (30% uniaxial strain), high semiconductor fill densities (40% fill factor), and high power outputs of 4.95 mW, (0.40 $mWcm^{-2}$) at 20 °C and 35.85 mW (3.32 $mWcm^{-2}$) at 60 °C.

While bench-top characterization can give accurate performance metrics, operation on the body introduces a host of parameters that must be understood in order for TEGs to be integrated with wearable sensors. There is still a gap in the literature on characterizing energy harvesting performance on the body [170, 150, 171]. To address this, I conducted comprehensive on-body characterization, analyzing the influence of TEG body placement and the influence of exertion and bio-mechanical movement on Seebeck output. Voltage output, heartrate, and surface and skin temperature are recorded during sitting, walking, and run tests mounted to the chest and forearm. The insights gained here are instrumental in designing a fully self powered vitals monitoring wearable powered by body heat. By integrating an array of eight TEGs with custom hardware I introduce TEGsense, the first device that demonstrates wireless and battery free photonic PPG wearable monitoring that can harvest energy from body heat, store harvested energy, boost to operational voltage, communicate with an optical PPG board, process data, and transmit data over BLE. This forearm worn sleeve can operate indefinitely without the need for charging or connection to a data-logger as long as an adequate temperature differential exists. (Figure 4.1c-d). Collectively, the work presented here exhibits a new milestone for battery-free wearables, acting as a first step to fill the gap of photonic-based PPG sensing powered solely by the body,

a key open target in the field [144]. This new framework for TED design generates an order-of-magnitude increase in power density over our previous designs [20, 151] (Figure 4.1e) and builds off of the past successes of implementing large TEG arrays in aquatic environments for sensing [137].

4.2 Experimental Section

4.2.1 Elastomeric Resin Composition

The center layers and stencils were 3D printed using a material composed of 49.02 wt% of epoxy aliphatic acrylate (EAA, Ebecryl 113, Allnex USA), 49.02% of aliphatic urethane acrylate (AUD, Ebecryl 8413, Allnex, USA) and 1.96% TPO (diphenyl(2,4,6-trimethylbenzoyl)phosphine oxide, Genocure TPO, RAHN USA Corp.) as the photoinitiator. TPO was dissolved in elastomeric monomers in a hot water bath at 86 °C.

4.2.2 3D Printing

A DLP 3D printer (PicoHD@27, Asiga) was used for all printing. Printing occurred at 40°C, with each layer irradiated for 0.5 s, with a layer thickness of 100μm. Once printed, the structures were sonicated in isopropyl alcohol (IPA) for 3 minutes to clean off uncured resin. Detailed printing parameters can be found in Table C.2 (Supporting Information).

4.2.3 Thermoelectric Device Fabrication

Images of the fabrication process can be found in Figure C.1 (Supporting Information). The center layer of the TEGs was first printed using DLP printing (Figure C.1i, Supporting Information). The dimensions for the active areas of the TED's various configurations were: 42.7 × 22.6 × 1.6 mm, 200 semiconductors, and a fill density of 40.6 % for LA-HD, 41 × 30 × 4 mm, 140 semiconductors, and a fill density of 22.3 % for HA-LD, 38.9 × 27.7 × 4 mm, 216

semiconductors, and a fill density of 39.2 % for HA-HD (Table C.3, Supporting Information). Next, p and n type semiconductors were placed into the printed holes in P-N π configuration (Figure C.1ii, Supporting Information). Depending on the configuration, the semiconductors used were $1.4 \times 1.4 \times 1.6$ mm 99.99% purity Bi_2Te_3 semiconductors (Wuhan Xinrong New Materials Co., Ltd.) and $1.4 \times 1.4 \times 4$ mm Bi_2Te_3 semiconductors (Ningbo Sen Ao electronic Technology Co., Ltd). A 1 mm thick DLP printed soft stencil was then placed over the device, forming a seal between the device and stencil (Figure C.1iii, Supporting Information). A light layer of EGaIn was then airbrushed onto the openings of the stencil to mitigate contact resistance (Figure C.1iv, Supporting Information).

Next, bi-phasic LM-Ag-SIS inks were formulated. Styrene-isoprene block copolymers (SIS, Sigma Aldrich) was dissolved in toluene (1.5:8.5) at 100°C for 1 hour. Once a clear and homogeneous solution was obtained, 1.54 Ag flakes (SF 94, Ames Goldsmith corp.) was added to 1 g SIS solution, then hand mixed for 30 seconds to disperse the micro-sized flakes. Then, 2.7 g EGaIn was added and hand mixed. This solution was then planetary mixed for 3 minutes at 2000 RPM. The ink was then loaded into a syringe for controlled injection into each of the interconnect wells created by the soft stencil layer (Figure C.1v, Supporting Information). To mitigate warping of the soft stencil and toluene evaporation, this process is done on a cold surface. The stencils were then removed, leaving the semiconductors (Figure C.1vi, Supporting Information). The trace width separation between interconnects was $700\mu m$. To evaporate the toluene, the device was placed on a hot plate for one hour at 60°C. Next, I used a planetary mixer to make a 65 vol% LM dispersion of LM in epoxy, and deposited a $700\mu m$ layer over the conductive interconnects using a thin film applicator (Figure C.1vii, Supporting Information). The LM-epoxy was left to settle overnight, followed by 1 hour curing at 60°C and 1 hour curing at 120°C. The control specimens were fabricated using an identical procedure, except the final LM-epoxy coating was substituted with neat epoxy. For devices without a coating (either LM-epoxy or neat epoxy), the UV curable ink used in the 3D printing process is coated onto the surface with a brush and then cured with

λ = 365 nm UV irradiation at 5 W for 12 minutes (Warson R838). This process was then repeated on the back side (Figure C.1viii, Supporting Information). Finally, copper tape or braided wire was affixed to form electrical leads.

4.2.4 Thermoelectric Testing

To measure the thermoelectric performance of the TEDs, I placed the devices on a hot plate with a computer heat sink applied to the opposite side (to improve the temperature differential), and simultaneously recorded the voltages and temperatures. Each device configuration was tested three times. Peak voltage values were recorded before the temperature differential degraded due to heat transfer. Power output was recorded by measuring voltage in parallel with an external load resistor, where $P = \frac{V^2}{R_{ext}}$. The peak voltage was again recorded. Peltier heating and cooling occurs when a current is applied across the TED [172]. For Peltier measurements, a representative spot temperature measurement was taken for three cycles at each current using a thermal camera (FLIR A35, Teledyne FlIR LLC). All tests were conducted at room temperature.

4.2.5 Mechanical and Thermal Testing

For mechanical testing, I extended the length of the non-active section of the TEGs, to allow the devices to be mounted into a universal materials tester (Instron 5969, with 50 N load cell). Euler's critical load is defined as $P_{cr} = \frac{2\pi EI}{K^2L^2}$ where $L = 46mm$ is the length of the beam and $K = 0.5$ is the column effective length factor. For peel tests, a sample of the 3D printed acrylate with active dimensions of $23.5 \times 35 \times 0.7$ mm coated with 0.5 mm of 60 vol% LM-epoxy. This was then placed in the Instron and subjected to a $\theta = 180^\circ$ T-peel loading condition. Work of adhesion (W) was defined as $W = (1 - \cos\theta)PL$ where P is the force of peel of 1.15 N and L is the width of the sample at 23.5 mm [173]. For thermal testing, I used a thermal interface material analyzer (TIMA5, Nanotest) to record the thermal resistance and thermal

conductivity of uncured 65 vol% LM-epoxy at various thicknesses from $500-1000\mu m$. The reported values at each bondline thickness are an average of 40 data points.

4.2.6 Finite Element Analysis Simulations

Contributions: I designed and fabricated the samples used for FEA. Youngshang Han conducted the FEA simulations.

We simulated the time-dependent energy harvesting of the TEG devices using FEA software COMSOL Multiphysics ®. The considered physics was heat transfer, electric currents, and thermoelectric effects. The representative volume element method was applied, to improve computational efficiency and scalability. To match the physical experiments, we set the simulation time-step to 0.855 s. The input boundary conditions were the temperatures on the TEG's bottom thermal interface, and the output was the thermoelectrically harvested voltages. For simulating the different types of LA-HD voltage output with respect to time, a 5 cm tall aluminum block was placed on top of the TEGs, matching the experimental condition, and the convective heat transfer coefficient of air is set to 10 Wům^{-2}ůK^{-1}. However, for simulating the wearable test, we used a root mean squared air velocity of 0.3 m/s, corresponding to a slow walking pace. See Table C.4 (Supporting Information) for a more complete listing of the parameters used in our simulations.

4.2.7 Wearable Testing

To test the performance of TEG devices when worn by a user who was operating a treadmill, our participant wore one HA-LD+LM-epoxy TED on the inside of their left wrist and another on the left side of their chest. A K-type thermocouple was integrated on each side of each HA-LD+LM-epoxy TED, and the final TEG+thermocouple pair was integrated into a compression garment. Each TEG was connected to an Ardiuno MKR Zero board that read voltage data from a ADS1115 16-bit ADC (Adafruit, LLC), read temperature data from two thermocouple amplifier MAX31856 boards (Adafruit, LLC), and finally logged all the data to a micro SD

card. Simultaneously, the user's heart rate was measured using an ECG (Zoll, Inc.). Two sets of initial tests were conducted: sitting (~375 s) followed by walking (2 mph for ~375 s), and sitting (~375 s) followed by running (5 mph for ~675 s). To reduce signal noise, the temperature data was pre-processed with manual outlier rejection followed by a low-pass filter with a cutoff frequency of 0.032 Hz when needed. Finally, a third test was conducted to provide more insight into the steady-state settling time: sitting (~320 s) followed by running (5 mph for ~1500 s).

4.2.8 TEGsense Board Design

A fully TEG-powered custom printed circuit board (PCB) was developed with integrated power management, sensing, and control hardware. In contrast to the PC-powered Arduino configuration just described for TED characterization, this circuit was designed to leverage those experiments and enable a fully body-heat powered device. The TEGSense board (see https://github.com/TEGSense and Figure C.18, Supporting Information) used a ultra low voltage step-up converter (Linear Technology LTC3108) to boost a low voltage TEG input (~50 mV) and charge a 10.8 mF capacitor bank to 4.1 V. To minimize energy loss and achieve sufficient surge current to power on the microcontroller, we used low equivalent series resistance (ESR) aluminum polymer capacitors (Elite UGS1C272MP51020F5RU, 10 mΩ). A hysteretic voltage monitor (Microchip MIC2779) was used to enable the 1.8 V and 3.3 V regulators once the capacitor bank reaches 4 V. If the charge fell below 3.3 V, the monitor disabled the downstream regulators, thus turning off the microcontroller. To capture sensor data over inter-integrated circuit (I2C) and then relay that data to an external PC via BLE, the circuit used a module (u-blox BMD-350) that had an integrated chip antenna and a Bluetooth Low Energy (BLE) enabled microcontroller (Nordic Semiconductor nRF52832). A finger-worn photoplethysmograph (PPG) sensor (Maxim Integrated MAX30101) sensed infrared (IR) and red light reflected by skin tissue at 100 Hz for a period of three seconds per sampling event. The first sampling event occured when the microcontroller turned on

(i.e., after the capacitor voltage reached 4 V). Subsequent measurements were recorded at six minute intervals, as long as the minimum capacitor voltage (3.3 V) was maintained. The red and IR PPG waveforms were received by an external PC for subsequent analysis.

4.2.9 TEGsense Demonstration

TEGsense was fabricated in the same way as previously described for HA-HD+LM-epoxy TEGs. TEGsense comprised 8 HA-HD+LM-epoxy TEGs wired in parallel into an array with overall dimensions of 12.7×9.5 cm. This is then integrated into an elastic compression sleeve and worn on the forearm. A hole was cut into the compression sleeve to allow for the TEG to be integrated and mounted directly on the skin when worn. To achieve highest efficiency, TEGsense's electrical resistance needed to be in the range of $2-10\ \Omega$ for impedance matching with the booster converter. Considering each TEG has an internal resistance of $8-10\ \Omega$, a series configuration leaves a large impedance mismatch. To circumvent this, TEGsense TEGs were configured in a parallel configuration decreasing overall impedance within the range. Low effective series resistance (ESR) of the capacitors was needed to decrease capacitor charge time. To accomplish this a parallel array of four 2.7 mF aluminum polymer capacitors was selected as opposed to a higher ESR super-capacitor.

4.3 TED Design and Fabrication

The high Seebeck, Peltier, and mechanical performance of the devices introduced here were enabled through a unique combination of LM-based material architectures and material integration approaches (Figure 4.1a and Figure C.1, Supporting Information). First, a deformable acrylate based resin [132, 174] was 3D printed using digital light processing (DLP), creating the center layer to enable complex internal structural designs to achieve mechanical deformability while maintaining a low thermal conductivity of $\sim 0.19\ Wm^{-1}K^{-1}$

to mitigate heat transfer. This material exhibits < 1% thermogravimetric loss at 220 °C and excellent mechanical compliance making it appropriate for wearable energy harvesting applications (Figure C.2). Bismuth telluride (Bi_2Te_3) semiconductors were then placed into the printed slots of the center substrate, in a p-n π configuration. A soft 3D-printed stencil of the acrylate based material was then placed over the semiconductors, forming sealed wells for the conductive ink to fill. Next, I airbrushed a thin layer of EGaIn onto the stencil to mitigate contact resistances. The LM-Ag-SIS ink solution was used to electrically connect the semiconductors with conductivity coming from the percolating network of EGaIn droplets and Ag flakes, along with regions of alloyed AgIn. This ink was introduced because of its low electromechanical coupling, high strain limit, and high electrical conductivity [175, 176]. The LM-Ag-SIS ink solution was injected into the wells of the stencil connecting together the LM coated semiconductors, producing traces. The ink's processability and stability during deposition allowed for greatly improved manufacturability and decreased chance of shorting, allowing us to achieve higher semiconductor densities compared to bulk LM approaches.

Once the ink was deposited, I removed the stencil and allowed the solvent to evaporate, leaving low-resistance connected traces. To protect the circuitry, an encapsulation layer of either an LM-epoxy composite (made by shear-mixing liquid metal and epoxy resins) or UV curable resin was deposited and cured on the top layer. By comparing the two encapsulation materials (in subsequent sections), I were able to determine the effects that improving the thermal contact resistance would have on device performance. The circuit fabrication process is then repeated on the backside. Images of the completed devices are given in Figure 4.2a-d, highlighting the various fill factors (fraction of semiconductor surface area over overall surface area), aspect ratios, and encapsulation layers compared in this work. Further fabrication details can be found in the Experimental Section.

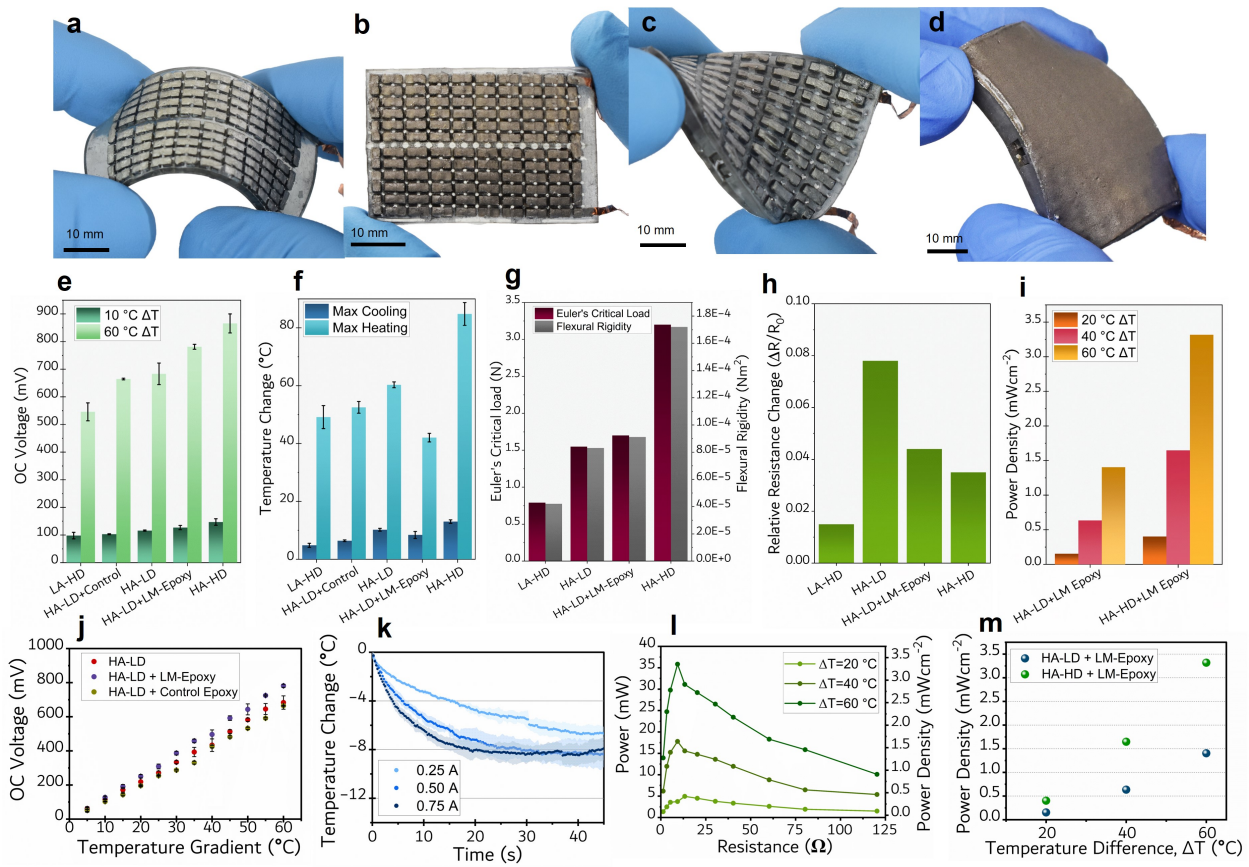

Figure 4.2: Characterization of TEG Configurations. Images of **a**, Low-Aspect High-Density (LA-HD), **b**, High-Aspect High-Density (HA-HD), **c**, High-Aspect Low-Density (HA-LD), **d**, and High-Aspect Low-Density+LM-epoxy TEG configuration. **e**, Seebeck open-circuit voltage performance at $\Delta T = 10°C$ and $\Delta T = 60°C$ for various TEG configurations. **f**, Peltier performance of max cooling and max heating for various TEG configurations. **g**, Mechanical performance of TEG configurations comparing flexural rigidity and Euler's critical load. **h**, Relative resistance change performance. **i**, Power density comparison between HA-LD + LM-epoxy and HA-HD + LM-epoxy TEG configuration at ΔT=20, 40, 60 °C. **j**, Open-circuit voltage vs temperature comparing HA-LD, HA-LD + LM-epoxy, and HA-LD + Control Epoxy configurations. **k**, Peltier cooling performance of High-Aspect Low-Density + LM-epoxy configurations. **l**, Power output vs external load Resistance for HA-HD + LM-epoxy TEG at ΔT=20, 40, 60 °C. **m**, Comparison of peak power outputs for HA-LD + LM-epoxy and HA-HD + LM-epoxy TEGs.

4.4 Thermoelectric Device Performance with Varying Design Parameters

4.4.1 Semiconductor Aspect Ratio Performance Comparison

To better understand the influence of semiconductor aspect ratio on holding a temperature differential and generating a high voltage output, I compared devices with high and low aspect ratio semiconductors. Both device types had similar fill factors (42% and 39%) but with two different semiconductor dimensions selected: $1.4 \times 1.4 \times 1.6$ mm and $1.4 \times 1.4 \times 4$ mm, respectively referred to as Low-Aspect High-Density (LA-HD) (Figure 4.2a and Figure C.3, Supporting Information) and High-Aspect High-Density designs (HA-HD) (Figure 4.2b and Figure C.4, Supporting Information). The HA-HD had the addition of a hollow center structure with pillars to increase mechanical compliance for this taller configuration.

For evaluating the Seebeck energy harvesting performance, I measured open circuit voltage (V_{oc}) vs. temperature difference (ΔT) (Figure 4.2e and Figure C.5a, Supporting Information), along with voltage density (Figure C.5b, Supporting Information). Seebeck voltage followed a linear relationship, as predicted by $V = n\alpha\Delta T$, where n is the number of thermocouples, α the difference in Seebeck coefficients between the p and n type semiconductors, and ΔT was the temperature differential across the device. HA-HD exhibited a 40% and 45% increase over LA-HD at ΔT=10°C and 60°C respectively. Increasing the distance between the depletion regions and decreasing the thermal conductance between the hot and cold faces of the device leads to a slower degradation of the thermal gradient and higher voltage output (Figure C.6a-b, Supporting Information).

Peltier cooling and heating improvements were also demonstrated with the use of high-aspect ratio (HAR) semiconductors (Figure 4.2f and Figure C.7a-b, Supporting Information). At 0.75 A, cooling ΔT peaks at -4.8±0.7 °C at 2.8 s for LA-HD compared to -13.0±0.6 °C at 8.8 s for HA-HD. Heating performance confirms this trend, with temperature increases at

0.75 A of 49.1±4.0 °C for LA-HD compared to 84.8±4.0 °C at 45 s for HA-HD (see Section S2, Supporting Information).

While Seebeck and Peltier performance increased with the HAR semiconductors, mechanical performance decreased due to the increase in bending moment. After 10 cycles of 20% compressive loads, Euler's critical load (P_{cr}) and flexural rigidity (EI) increased from $P_{cr} = 0.79\ N$ and $4.21 \times 10^{-5}\ Nm^2$ for LA-HD to $P_{cr} = 3.20\ N$ and $1.72 \times 10^{-4}\ Nm^2$ for HA-HD, with elastic and plastic regimes appearing in both curves along with relative resistance change staying under 0.05 for both devices (Figure 4.2g-h and Figure 4.3a-b). The use of HA-HD semiconductors produced a device with much better electrical performance but with the trade-off of increase mechanical rigidity.

4.4.2 Semiconductor Fill Density Performance Comparison

Mechanical compliance is important not only from a comfort and compatibility perspective but also to decrease the thermal resistance between the skin and device through constant contact with the body during movement. Decreasing the density of rigid semiconductors is one way to increase flexibility and potentially improve mechanical performance. A device with a lower fill density of 22% referred to as high-aspect low-density (HA-LD) TEG was fabricated and compared (Figure 4.2c and Figure C.8, Supporting Information) to HA-HD. HA-LD TED underperforms the HA-HD device by 24% at both 10 °C and 60 °C. When normalized over surface area, the HA-LD V_{oc} was within the margin of error of the LA-HD (Figure C.5b, Supporting Information). Still, voltage drop over time is improved over LA-HD (Figure C.6c, Supporting Information).

Peltier heating and cooling performance is given in Figure C.7c (Supporting Information) for HA-LD. For Peltier cooling and heating, the cooling performance (ΔT) at 0.75 A peaked at -10.2 ±0.5 °C @ 15.3 s with heating performance of 60.3±1.0 °C at 45s, performing in between LA-HD and HA-HD devices. Mechanically, performance for 10 cycles at 20% compression was

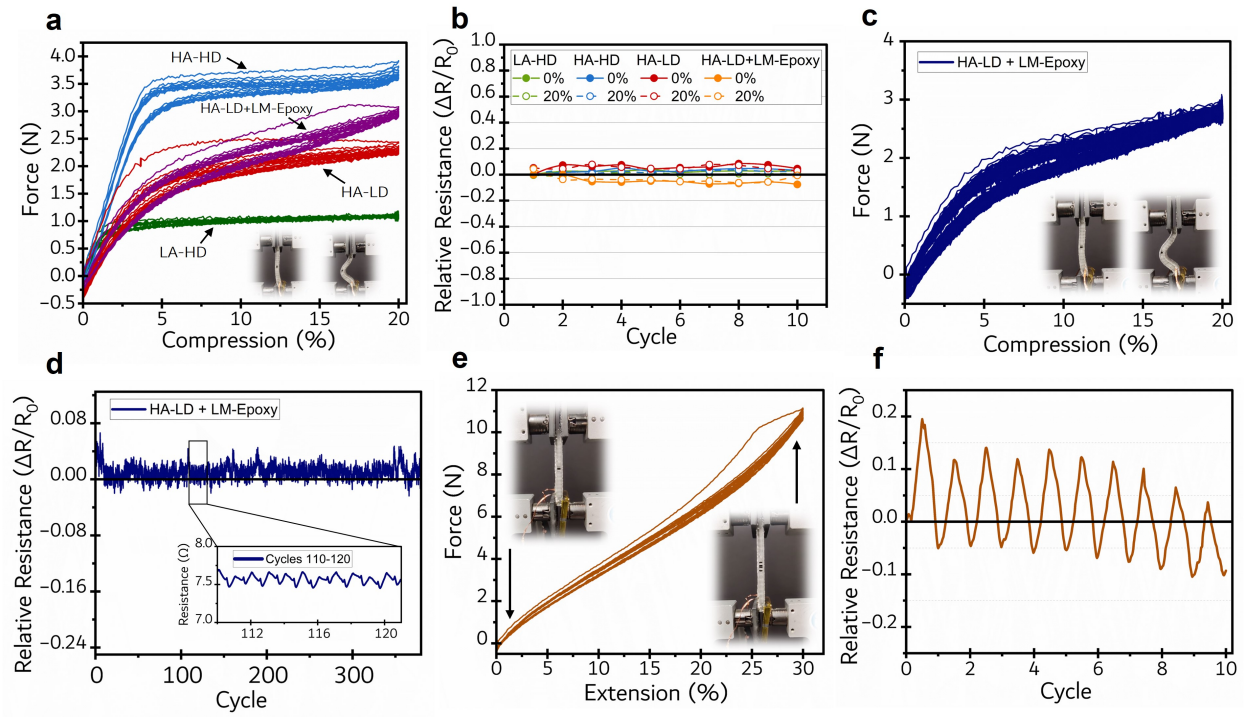

Figure 4.3: Electromechanical Characterization: **a**, Compression vs force comparison for 10 cycles at 20% compression. Inset shows a HA-LD device at 0% (left) and 20% compression (right). **b**, Comparison of change in relative resistance at 20% compression for 10 cycles. **c**, Mechanical performance at 20% compression for 380 cycles for HA-LD + LM-epoxy device. Inset: Images of device at 0 and 20% compression. **d**, Change in relative resistance over 380 cycles at 20% compression for HA-LD + LM-epoxy TEG. Inset: resistance at cycles 110-120. **e**, Mechanical performance at 30% uni-axial strain for 10 cycles for HA-LD + LM-epoxy device. Inset: Images highlighting 0% and 30% extension. **f**, Relative resistance change over 10 cycles at 30% extension for HA-LD + LM-epoxy TED.

in between LA-HD and HA-HD mechanical performance with a less defined Euler critical load of $P_{cr} = 1.55\ N$ and flexural rigidity of $8.31 \times 10^{-5}\ Nm^2$ with an intra-cycle relative resistance change of around 0.05 (Figure 4.2g-h). For operation on less curved and more stable surfaces such as the forearm for wearable energy harvesting, HA-HD is still ideal due to high Seebeck output.

4.4.3 Thermal Interface Performance Comparison

Contributions: Jeff Gelorme designed the LM-Epoxy TIM introduced here in collaboration with Arieca Inc. Dr. Hing Jii Mea conducted the thermal conductivity measurements for this material. I designed and built all devices using this material, conducted all characterization

of the TEGs, and designed how the LM-Epoxy was introduced into the TEDs.

The devices characterized in previous sections of this work relied on a thin ($\sim 300\mu m$) UV curable ink with a low thermal conductivity ($\sim 0.19\ Wm^{-1}K^{-1}$) that was applied onto the surface (Figure C.2, Supporting Information). This thin layer was prone to damage leaving interconnects exposed. To address this, we developed and utilized a custom formulated epoxy composed of polypropylene glycol and diglycidyl ether that allows for robust adhesion to the TED without embedding mechanical compliance. In order to achieve high thermal conductivity, we added a $\sim 65\%$ volume loading of EGaIn to the epoxy and shear-mixed to attain a homogeneous suspension. EGaIn was selected as the metallic filler since it has a high thermal conductivity of 26.4 $Wm^{-1}K^{-1}$ while being liquid at room temperature [177]. The thermal properties of the LM-epoxy formulation were measured using a Nanotest TIMA 5 thermal interface material analyzer. For a bondline thickness of 750 μm, a thermal resistance with respect to area and volumetric thermal conductivity of $257.5 \pm 1.6\ mm^2KW^{-1}$ and $2.90 \pm 0.02\ Wm^{-1}K^{-1}$ respectively were recorded (Figure C.9a-b, Supporting Information). This represents a ~2× improvement in thermal performance compared to previous thermally conductive elastomers that use liquid metal or other filler particles [20, 22, 93, 24, 161, 38]. Additionally, this LM-epoxy bonded well to the 3D printed elastomer used as the substrate, with a work of adhesion of $5.4 \times 10^{-2}\ Jm^{-2}$ and a peel force of 1.15 N. (Figure C.9c, Supporting Information). This material was developed to improve the lifetime of the devices by protecting the interconnects from damage along with improving heat transfer and voltage output.

A HA-LD version with LM-epoxy composite (Figure 4.2d and Figure C.10, Supporting Information) was fabricated along with control samples with an unfilled epoxy to compare the influence of using a TIM to coat the two sides of the TED (Figure C.11, Supporting Information). The device with improved thermal management generated improved Seebeck output by 21% and 16% at 10 °C and 60 °C respectively (Figure 4.2e,i). The experimentally measured Seebeck performance of TEDs is analytically supported by finite element analysis (FEA). As shown in Figure C.6d-e (Supporting Information), the thermoelectric simulation

confirms that employing LM-epoxy as a thermal interface improves peak voltage output compared to control epoxy. FEA and experimental results both indicate voltage output peaking quickly followed by a gradual descent as heat transfers through the device. The simulated voltages show similar trends with experimental results, computationally validating the Seebeck measurement (Section S1, Supporting Information).

Power output was characterized with an external varied resistor acting as the load. Power output is shown in Figure C.5c (Supporting Information) with power (P) being determined by $P = \frac{V^2}{R_{ext}}$ where V is the voltage across the external load resistor and R_{ext} is the external resistance. Power peaked at 1.89 mW, 7.81 mW, and 17.27 mW at a 20, 40, 60 °C ΔT along with a 0.154 $mWcm^{-2}$, 0.635 $mWcm^{-2}$, and 1.404 $mWcm^{-2}$ power density respectively.

TEDs with the addition of the LM-epoxy TIM exhibited improved Peltier cooling performance over the control epoxy device and decreased heating with peak cooling ΔT of -8.4±1.2 °C @ 0.50 A at 44.3 s for HA-LD + LM-epoxy vs. -6.4±0.3 @ 0.50 A at 41.3 s for HA-LD + Control Epoxy (Figure 4.2f,k, Figure C.7d, and Figure C.12a-b, Supporting Information). Thermal imaging has shown improved thermal performance in distributing heat over the area of the Peltier cooler compared with the control (Figure C.13, Supporting Information).

HA-LD + LM-epoxy mechanical performance was similar to that without LM-epoxy (Figure 4.2g-h) with $P_{cr} = 1.70N$ and flexural rigidity of $9.11 \times 10^{-5}\ Nm^2$ similar to samples without LM-epoxy composite. No mechanical or electrical failure occurred (Figure 4.3a-b). Similar results were recorded for a high-loading cycle test that was conducted for 380 cycles at 0% and 20% strain, again with no mechanical or electrical failure at the end of this test (Figure 4.3c-d). A 10-cycle uniaxial strain test at 30% was conducted with a peak relative resistance increase of ~ 0.20 (Figure 4.3e-f).

LM-epoxy improved Seebeck harvesting, Peltier cooling, and mechanical robustness. A final HA-HD device with LM-epoxy was fabricated. The power output of a HA-HD + LM-epoxy harvester at 20, 40, and 60 °C with an external resistor as a load was characterized

(Figure 4.2l). Power outputs are 4.95 mW (0.402 $mWcm^{-2}$), 17.79 mW (1.647 $mWcm^{-2}$), and 35.85 mW (3.318 $mWcm^{-2}$) respectively. This was a large improvement in power density over HA-LD harvesters without LM-epoxy (Figure 4.2m). Comparisons of electrical and mechanical performance with other TEG research can be found in Table C.1 (Supporting Information).

4.5 On-Body Wearable Integration

Contributions: I designed the wearable tests, built the devices, and conducted wearable testing. Dr. Dylan Shah assisted in wearable testing along with test design and coding.

To determine real-world compatibility of the proposed TEGsense design, I characterized the device with user studies in both a laboratory setting and an outdoor environment. Importantly, our data suggests that various environmental (windspeed, temperature) and physiological conditions (correlated with heartrate, as measured) influence TEG voltage output. I designed the study to probe at the general influence of bio-mechanical movement, physical exertion, and device location on the user's body to better understand the average and peak power outputs. Specifically, we ran tests with TEGs integrated into wrist-worn and chest-worn garments while sitting, walking, and running, and asked our user to walk outdoors at a normal pace while wearing a completed 8 TEG TEGsense array plus TEGSense circuit board for processing and Bluetooth data transmission. I should note that these studies involved heartrate tracking, they did not directly measure metabolic energy consumption or influence of the worn TEG device on metabolic cost.

To test the influence of bio-mechanical and physiological factors, I conducted trials on a treadmill with TEGs integrated into the subject's clothing. In particular, the influence of human motion on increasing the convective cooling rate on the outside of the TEG, the role of exercise on conductive heating from the body onto the inside of the TEG, and the influence of TEG body location on Seebeck performance were all explored (**Figure 4.4a-b**).

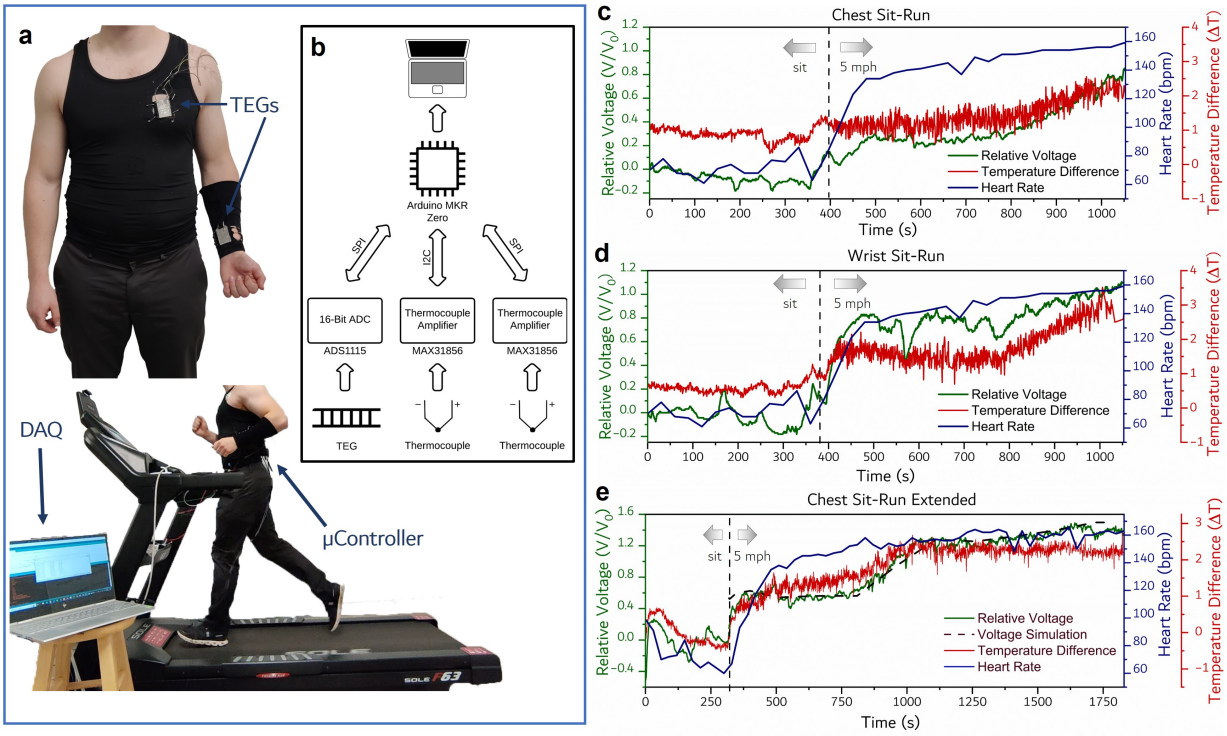

Figure 4.4: Wearable Testing. **a**, Top: image of experimental set up for TED placement on the wrist and chest. Bottom: image taken during a run test at 5 mph highlighting placement of one of the μcontrollers. **b**, Block diagram of circuitry used for data collection. **c-e**, Results of wearable treadmill testing for wrist and chest worn devices during sit-run testing.

To accomplish this, an experimental setup was designed with HA-LD + LM-epoxy TEGs mounted on the wrist and chest embedded with a thermocouple temperature sensor on each side and integrated into compression clothing. Heart rate was also monitored during these tests (see Experimental Section). Wrist and chest placement were chosen due to their differences in relative motion during walking and running along with these placements corresponding to the locations of wearable health monitoring systems.

4.5.1 Sit-Walk Test Results

We investigated Seebeck performance during sitting and walking tests with TEGs mounted on the wrist and chest. The influence of increased convective cooling from bio-mechanical movement on the wrist-worn device was clear. For the wrist sit-walk test, movement across the device's outside face during walking lowered the surface temperature leading to a ~ 0.2

increase in relative voltage (Figure C.14a and C.15a, Supporting Information). For the chest-worn device, temperature stayed consistent for both sitting and walking (Figure C.14b and C.15b, Supporting Information) from no additional airflow across the device as chest movement is limited.

4.5.2 Sit-Run Test Results

Data for the sit-run chest and wrist test are given in Figure 4.4c-d. Both cooling from bio-mechanical motion and heating from exercise played a major role in TEG Seebeck output with a > 1.0 relative voltage change for the wrist-worn device and 0.8 relative voltage change for the chest worn device (Figure C.15c-d, Supporting Information). Sweat was also found on the inside of the device after testing which may help to decrease thermal resistance.

While these initial tests helped to inform the influence of bio-mechanical motion and exertion on TEG Seebeck performance, no sit-run tests reached a steady state for voltage or temperature values. A longer test was conducted to determine if the Seebeck improvement would plateau. Results are shown in Figure 4.4e and Figure C.16 (Supporting Information). When comparing voltage, temperature differential, and heart rate, one can see that these all began to plateau around 1000 s indicating a steady state and stable voltage output. Based on these wearable tests, I can predict large ($> 2X$) consistent Seebeck improvement during exertion. To investigate a general trend of the harvested voltage, FEA for the sit-run test is conducted. While the inside and outside temperatures are determined as boundary conditions, the simulated voltage agreeably matches with the experimental output. It also demonstrates that the estimation on wearable TEG is possible even with the complicated working conditions, including both sedentary and running subject as a heat source. See Section S3 (Supporting Information) for expanded discussion on wearable testing. For integration into a fully functional wearable devices, the wrist-worn orientation was selected as it exhibits superior Seebeck performance during testing.

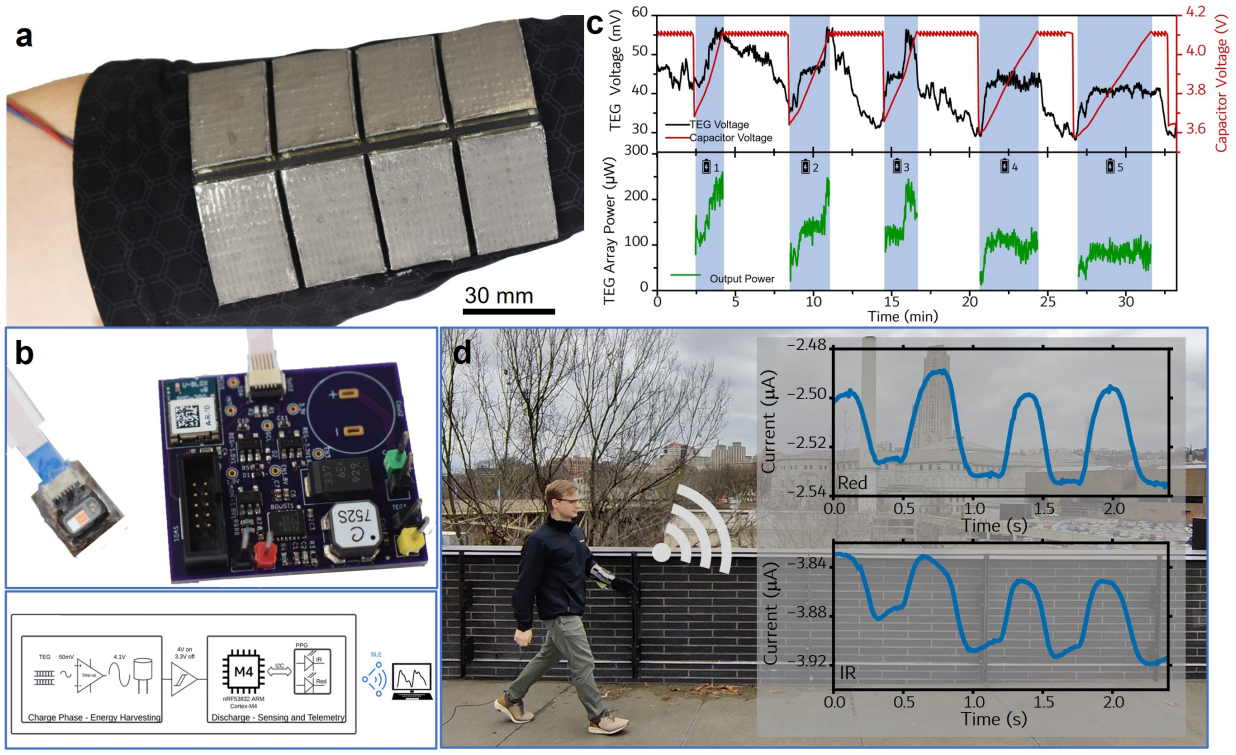

Figure 4.5: TEGsense implementation and testing. **a**, Image of 8 HA-HD+LM-epoxy TEGs intergrated into TEGsense array. **b**, Top: Image of TEGsense board integrated with processor, BLE, boost converter, and photonic chip. Bottom: TEGsense board block diagram. The thermoelectric generators use the temperature gradient between the body and the environment to generate a low voltage potential (~50mV), which is boosted by a step-up voltage converter to charge a capacitor bank to 4.1V. A hysteretic switch powers on the microcontroller and sensor when the capacitors rise above 4 V. Once on, the microcontroller collects red and infrared light reflection measurements from a photoplethysmograph sensor. This waveform is telemetered to an external laptop over Bluetooth. Finally, when voltage drops below 3.3 V, the switch disconnects power to the microcontroller and sensor. Once on, the microcontroller collects red and infrared light reflection measurements from a photoplethysmograph sensor. This waveform is telemetered to an external laptop over Bluetooth. **c**, Voltage vs. time data for both the TEGsense array voltage into the step-up converter, and the boosted voltage from the step-up converter into the 10.8 mF capacitor bank. The bottom concurrent plot shows the power output during the blue-shaded charging periods. **d**, Red and IR PPG waveform data being transmitted over BLE after energy harvesting and data collection during testing.

4.5.3 TEGsense Wearable Performance

Contributions: Anthony Wertz designed and built the TEGsense board including board design and firmware along with testing the device with myself. I designed and built all TEGs and TEGsense armband along with testing the TEGsense system.

To address the lifespan and data transmission issues associated with battery powered

wearables, I introduce a large TEG array (TEGsense) to demonstrate battery free medical sensing and wireless data transmission. TEGsense consists of 8 HA-HD+LM-epoxy TEGs integrated into a forearm sleeve connected to a capacitor array and custom low power photonic PPG board (Figure 4.5a-b). As shown during wearable testing, the wrist location was chosen as limb movement leads to a significant increase in convective cooling leading to a Seebeck energy harvesting boost. Power generated from the TEG array is initially boosted to 4.1V using a low power boost converter to charge a 10.8 mF cap array. Once charged, the TEGsense board records the photoplethysmogram (PPG) wave form. This data is then sent over Bluetooth low energy (BLE) with the board reentering a hibernation state. This repeats indefinitely while a temperature differential is held across the device. Further details can be found in the Experimental Section.

Results of the TEG array's charge rate is show in Figure 4.5c. TEGsense is run for 5 cycles with alternating standing and walking conditions on a cold day (6.6 °C) to understand the approximate charge times need to run the TEGsense board. TEGsense output voltage and capacitor charge voltage are shown indicating the short charge times for TEGsense board operation. During charging cycles, the wearer walks and charges the capacitor array for ~3 minutes. During cycles 4 and 5 the limb began to get cold due to outdoor exposure, leading to an increase in charge time, highlighting the influence of physiological conditions on performance. Because of the variability in charging time, complete discharging of the capacitors to power the circuit board were timed to occur every 6 minutes. In general, this resulted in time periods of ~2-3 minutes where the user was either walking or standing and no longer charging the capacitors. Following this validation of the device power management, we performed a separate set of experiments on another day in 2 °C weather in which TEGsense was used to operate a photonic PPG-sensing wearable. Capacitors were charged up during ~4 minutes of walking and then discharged to operate a circuit with a photonic pulse oximetry chip for PPG data collection, microcontroller for signal processing, and Bluetooth transmitter for wireless output of PPG waveforms to an external receiver. PPG waveforms were collected

recorded for both Red and IR (Figure 4.5d). The corresponding voltage data with the 4 minute charge time can be found in Figure C.17 (Supporting Information).

4.6 Conclusion

In this work, I introduce a framework for creating soft, flexible, and stretchable TEGs for powering body-mounted electronics. This includes the development of TEGsense, an integrated health monitoring wearable that converts energy from body heat into electricity used for battery-free operation of a photonic sensing device. Using this framework, I introduce new material architectures and design approaches for fabricating high-performance bendable and stretchable TEGs, explore the influence of biomechanical movement on device performance, and integrate these TEGs into a PPG monitoring wearable. To enable development of these TEGs stretchable LM-Ag-SIS inks were integrated, enabling low internal electrical resistance and high semiconductor densities [176]. Additionally, a thermally conductive ($2.90 \pm 0.02 W m^{-1} K^{-1}$) and mechanically compliant LM-epoxy composite was used as an interface material and 3D printing was utilized to design hollow internal structures to decrease device stiffness.

A peak power output of 35.85 mW (3.318 $mW cm^{-2}$) is achieved at 60°C ΔT. Mechanically, these harvesters were found to operate with no mechanical or electrical failure at 30% uniaxial strain, and they showed no electrical or mechanical performance degradation after 380 cycles at 20% compression. As a Peltier cooler, a maximum change in temperature of $\Delta T = -13.0 \pm 0.6°$ C was generated at 0.75 A. Bio-mechanical testing with the wearable TEGs were performed to better understand the relationship between physical exertion, bio-mechanical movement, and TEG placement on device Seabeck harvesting. These tests concluded that wrist-worn TEGs experience large improvements (2×) in voltage output during running (5.0 mph).

4.6.1 Limitations and Next Steps

Current limitations of this work center on a few main areas of improvement. First, for flexible TEGs to gain adoption in the commercial space, these generators need to be produced using automated manufacturing methods compatible with production-grade electronics manufacturing lines. Future efforts to address this can include using pick-and-place machines to improve precision and decrease manufacturing time. Second, to increase power output, the internal resistance of the devices must be further reduced. In particular, new approaches are needed to mitigate the semiconductor-interconnect contact resistance. This will require improvements in surface coatings of the semiconductors along with improving the conductivity of LM based inks. High percentage oxide LM formulations of EGaIn (OGaIn) are potentially one direction to have scalable and repeatable fabrication, while simultaneously improving electrical conductivity to more closely approach the bulk conductivity of LM [178]. Such an improvement could lead to greater performance in ambient indoor conditions since decreased internal resistance would allow for improved impedance matching with boost converters.

Separately, coupling with other wearable energy harvesting modalities such a triboelectric or piezoelectric harvesting is another avenue for improved performance. Another consideration that needs to be better explored and addressed in future work is the impact of liquid metal wearables on human skin over a long period of time. With repeated use on the body, the LM-epoxy layer has a tendency to rub off onto the skin. Although previous work suggests that LM-polymer composites are not cytotoxic [179], further study is required. Additional work will need to be conducted to better understand LM's introduction into wearables. Waterproofing of these energy harvesters will also need to be explored for underwater applications along with their use in rainy or snowy environments [137]. Lastly, while most components of TEGsense were made soft and stretchable, the semiconductors are still rigid, leading to stress concentrations on the semiconductor-elastomer interface. To address this, progress depends on further miniaturization of the thermoelectric semiconductors or the use of semiconductor materials that are intrinsically soft and deformable. One particular direction would be to

focus on 3D printed thermoelectric semiconductors prepared in a slurry and direct-ink-write printed to directly replace their rigid counterparts [180].

4.7 Lessons Learned

Past efforts in wearable TEGs have been held back from generating enough power to run small wearable health monitoring systems due to the low power densities of the used. Previous work has only been able to show non-energy intensive applications for battery free wearbles such as temperature and humidity sensing. In this chapter, I introduce TEGsense, a TEG wearable system that integrates novel soft electronic materials, a new TEG design, and a PPG health monitoring board to enable a forearm worn PPG monitoring system that can operate outside on a cool afternoon. The system is designed using various custom TEG design configuations to generate power from body heat to charge a capacitor array, record PPG waveforms from an LED array mounted to the finger, process this data with an onboard microcontroller, and send this data over BLE.

The materials and device improvements that I have introduced in this chapter have the potential to open new directions in battery-free wearable electronics. I have made use of Ag and LM based inks and 3D printed elastomers for forming the electrical interconnects connecting the semiconductor elements and for the thermally insulating substrate in which the semiconductors are embedded. I have introduced a novel LM-epoxy composite for the thermal interface material to seal in the interconnects and increase heat transfer from the skin to the thermoelectric elements. However, to continue improving TED performance, further improvements on electrically and thermally conductive materials are required to improve power output and to perhaps even replace the rigid semiconductor elements used. A novel LM based soft composite material will be introduced in the next chapter.

Chapter 5

MXene-Coated Liquid Metal Composites for Soft Electrical and Thermal Interfaces

- **M. Zadan**, Y. Hu, J. Lipp, N. Lewis, D. Shah, D. Nepal, K. Dayal, C. Tabor, and C. Majidi, "MXenes as an Aggregation Mechanism for Thermal and Electrical Liquid Metal Composites", *Submitted*.

5.1 Introduction

So far in this dissertation, liquid metal (LM) has been incorporated into polymers to form composites that function either as an electrical conductor or as a thermal interface material. In both cases, enhanced thermal or electrical properties are achieved while maintaining a high mechanical compliance due to the liquid nature of the inclusions [181]. With the introduction of LM into silicone based elastomers, thermal conductivity has been shown to be improved by over an order of magnitude compared to unfilled bulk elastomers [182]. Thermal interface composite materials containing rigid fillers such a aluminum, copper, or carbon black oftentimes form shear stress concentrations at the soft rigid interface that can lead to

lower yield stresses compared to LM based composites [183]. These liquid metal embedded elastomer (LMEE) composites have enabled a new generation of thermal interface materials for the semiconductor and wearable electronics fields [184]. Even with these improvements, the composites are still inherently electrically insulating as a self limiting layer of insulating gallium oxide (Ga_2O_3) forms at the surface of all LM droplets in the presence of oxygen species [26].

Additionally, the low aspect ratio of LM droplets requires exceedingly high volume fractions, upwards of 80%, in order to form percolating electrically conductive networks [183]. To bypass this, various methods including shock transmission [161] and mechanical shearing have been used to rupture the oxide layer and form conductive pathways [104, 20]. As droplet size decreases and the surface area to volume ratio increases, the Ga_2O_3 shell becomes exceedingly more difficult to shear and become conductive. When LM composites are fabricated with both low volume fractions (~ 25 %) and small evenly dispersed droplets (~ 1 μm), these composites act as dielectrics making it exceedingly difficult to be made conductive through mechanical activation [29]. In addition, at low volume fractions ($< 25\%$), they exhibit low thermal and dielectric properties as confirmed by effective medium theory [185] with relative permittivities of < 10 @ $100kHz$ [38, 29] and thermal conductivities of < 0.4 $W/m/K$ [24].

One potential method to modify the thermal and electrical characteristics of multi-functional LM composites at such low fill factors and particles sizes would be to introduce a conductive additive that can wrap around the particles and induce aggregation. In the past, to modify composites properties and stabilize LM particles, organic and inorganic polymers along with 2D materials have been introduced to wrap and coat the surface of LM droplets and functionalize them. This has included polydopamine-coated inclusions [186] and polymer based approaches [187, 188] including ATRP synthesized particles [189]. Insulating graphene oxide has also been explored [190]. Still, these insulating materials do not offer improvements over bulk LM composites in thermal or electrical performance. More recently

developed 2D materials, such as MXenes, may offer a potential way forward due to their high electrical and thermal properties.

MXenes are a class of 2D conductive materials including transition metal carbides, nitrides, and carbonitrides made of alternating intercalated metallic layers capped with a termination layer [191, 192]. These materials exhibit strong negative surface charges and high stability when exfoliated and introduced into polar aprotic solvents [193]. Thermal and electrical performance of $Ti_3C_2T_x$ MXene flakes has been reported as high as $2.4 \times 10^6 S/m$ [194] and 42.2 W/m/K [195, 196] for MXene films respectively. Previous work has introduced this materials for a whole host of applications in including energy storage [197], flexible electronics [198], and recently soft composites [199]. The interactions and influence on morphology and material properties of these highly conductive 2D materials on insulating LM composites has yet to be properly understood.

In this work I investigate $Ti_3C_2T_x$ MXene nano-sheets as a coating and binder for LM composites along. In addition, I investigate how MXene coated LM particles act as an aggregation mechanism in soft composites to explore how small MXene volume fractions (0.25 vol %) effect composite morphology and performance changes. I demonstrate that even at low volume percentages (25%) of liquid metal, the introduction of small amounts of MXenes (0.25 vol %), induces an aggregation of LM particles (Figure 5.1a). This enables an improvement in thermal conductivity and shifts the composite from acting as an insulator to conductor at low bond length thicknesses (BLT). A novel synthesis method for MXene-LM composites is introduced, which enables wrapping of MXenes sheets around micron sized liquid metal droplets (Figure 5.1b). Once wrapped, these MXene-LM particles become electrically conductive mitigating the Ga_2O_3 insulating skin that has caused LM composite to be electrically insulating in the past. In addition, the MXene coating functionalizes the surface causing these particles to become "sticky". Once introduced into a silicone matrix material and processed, the MXene coated particles form large aggregates as opposed to samples without the MXene additive (Figure 5.1c). This is shown to greatly effect the bulk

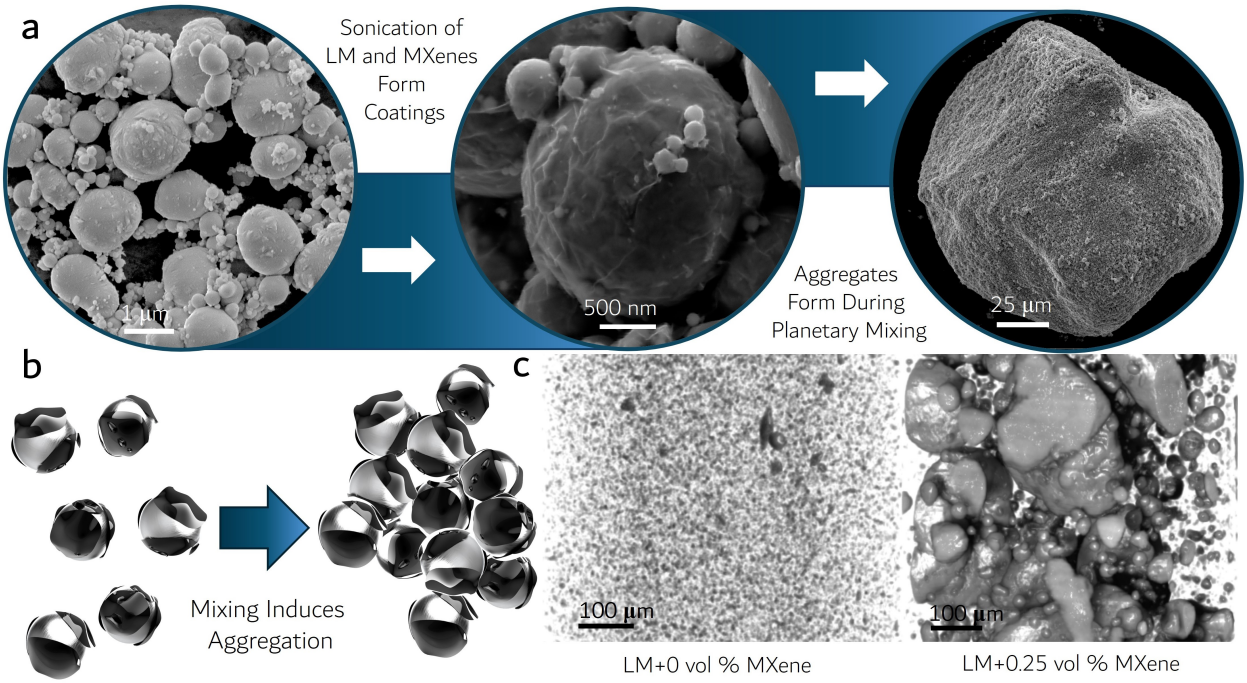

Figure 5.1: **a**, This diagram describes the synthesis Process of MXene-LM composites. Left: EGaIn particles are shown after being broken up by probe sonication. Middle: Image of LM+9.7 vol % MXene-LM composite after $Ti_3C_2T_x$ MXene sheets were probe sonicated with the EGaIn nano-droplets creating a coating of MXenes around the LM. Right: a silicone oil matrix was then added to the composite and mixed causing the functionalized MXene-LM composites particles to aggregate into large clusters as shown in the image of the LM+0.5 vol % MXene sample. **b**, Graphic highlighting, left: the MXene sheets coating the LM droplets followed bt, right: the sticking together of the MXene-LM composites after mixing in a silicone oil matrix material. **c**, calibrated microCT reconstructions showing the influence of a small amount of MXenes on particle aggregation vs an LM control sample.

thermal and electrical properties of the material.

5.2 Experimental Section

5.2.1 MXene Synthesis

MXene preparation was adapted from Shuck et al. [200]. The preparation of pristine $Ti_3C_2T_x$ involved the selective etching of the chemical bonds between transition metals and aluminum elements in the Ti_3AlC_2 MAX phase. The first key step is the in-situ generation of HF with highly concentrated LiF and HCl, which selectively removes the Al layer, resulting in accordion-like two-dimensional layered structures. Subsequent intercalation in DMSO

with ultra-sonication and washing steps resulted in 8-10 wt% of exfoliated $Ti_3C_2T_x$ sheets in a colloidal dispersion of 80:20 DMSO: H_2O. The termination layers (T_x) were a mix of -OH, -O, and -F.

5.2.2 MXene-LM Composite Synthesis

MXene-LM composite synthesis began with preparation of the EGaIn liquid metal (75 wt % Ga and 25 wt % In). Ga and In ingots (Rotometals, 99.99 % purity) were alloyed at 180°C on a hotplate overnight and periodically mixed by hand. For processing, a colloidal suspension of 80:20 DMSO (dimethyl sulfoxide, Sigma-Aldrich ≥ 99.99%): H_2O was prepared. 30 mL of the DMSO: H_2O solution was added to a 60 mL glass vial with a 30 mm base diameter. This solution was then degassed for 6 minutes in a desiccator using a vacuum pump. 14 g of EGaIn was then added to the solution. Next the liquid metal was processed using a probe sonicator (Sonics, VCX 500). The EGaIn was sonicated for 1 hour using using a 3.2 mm diameter microtip probe (Qsonica, 418A 1/8") placed approximately 1 cm above the base of the vial in an ice bath. The probe sonicator parameters were, 20 kHz, 500 W, 40 % amplitude, with a 8 s on and 1 s off cycle time. For the Liquid metal control sample, the contents were then vacuum filtrated. For samples with MXenes added, the correct amount of MXene solution was added to the vial. For example, for a LM+1 vol % MXene sample, 2.715 g (0.674 g MXene solution for the LM+0.25 vol % sample) $Ti_3C_2T_x$ solution was added. This was then hand mixed for 15 s. The solution was then sonicated again this time using a larger 6.4 mm diameter microtip probe (Qsonica, 420A 1/4") at 20 % amplitude for 30 minutes in an ice bath. The solution as then removed and vacuum filtrated using a 200 nm pore size filter (Nalgene vacuum filtration system) until the solvent was removed and the remaining material resembled a paste like consistency. The remaining material was then added to a planetary mixing cup and 6.586 g silicone oil was added (Dow Corning Corporation 200 ®fluid, 60,000 cSt @ 25 °C). for the low viscosity sample 7.207 g silicone oil were added (Smooth-On Dragon Skin ™10 Slow Part A, 23,000 cSt). The composite material was then hand mixed for 1 minute. The

material was then planetary mixed (Thinky, AR-100 conditioning mixer) for 5 minutes at 2000 rpm. This mixing process was then repeated 2 more times. Lastly, the composite was placed in an oven at 60 $^{\circ}C$ overnight to evaporate any remaining DMSO:H_2O solution and loaded into a syringe.

5.2.3 MXene Control Composite Synthesis

7.074g MXene solution and 4.390g silicone oil were added to a mixing cup. This solution was placed on a hot plate at 170$^{\circ}C$. An overhead shear mixer was then placed into the solution with a 24 mm diameter mixing head (Scilogex , OS20-SO). The solution was then mixed for 3 hours at 200 rpm. This was followed by being placed in an oven at 60$^{\circ}C$ overnight to remove any additional solvent.

5.2.4 Thermal and Electrical Characterization

For thermal testing, a thermal interface material analyzer was used (TIMA5, Nanotest) to record the thermal conductivity of MXene-LM composites at various thicknesses from 50-1000 μm. The heated head was set to 50 $^{\circ}C$ and the cooled head chilled to 15 $^{\circ}C$. Electrical conductivity measurements were conducted in parallel to thermal measurements with leads connected to the test heads (Keithley 2100 6 1/2 digit multimeter). For the electrical and thermal data, samples were averaged by MXene filler content and graphed. Error bars are the standard deviation with only the positive error being shown on the log scale electrical conductivity graph.

5.2.5 MicroCT Imaging

MicroCT Imaging was conducted using a Zeiss Xradia CrystalCT. Samples for imaging were prepared by extruding material into a 10 μL auto-pipette tip. The tip was then cut with the top section being mounted to the chuck. The sample was left to settle for a few hours before

imaging to limit the amount of drift in the silicone oil suspension. Depending on x-ray beam intensity counts during setup, the voltage and power were set to 70 kV at 6 W or 60 kV at 5 W. Pixel resolution was 1.4 μm. Imaging was conducted with 3600 projections and then reconstructed. Separately, SEM imaging was conducted using the FEI Quanta 600 and EDS measurements were taken using the Tescan Mira 3.

5.2.6 MicroCT Data Processing

The LM+0.25 vol % MXene sample was used as the calibration control with all other samples (aside from the MXene control) intensity calibrated to this sample. For intensity calibration, the plastic pipette tube and the LM based clusters were used as the controls, allowing for linear fitting. An upper Otsu image thresholding method was used on the LM+0.25 vol % MXene sample with this calculated intensity threshold then being used on all other calibrated samples [201]. Volumes of $500 \times 500 \times 1200$ μm were cropped for images in the paper. For determining particle size of the LM+0 vol % MXene control sample, an upper Otsu threshold was applied to the intensity calibrated sample as before. The sample was segmented leaving only particles above the Otsu threshold. A multiple region of interest (ROI) was generated from the segmentation. Regions of high density with multiple particles in contact acting as outliers were manually disconnected by deleting connecting voxels. The process was repeated for the LM+0.25 vol % MXene sample. Due to the large aggregates formed, multiple aggregates were in contact with each other and not able to be differentiated during segmentation. Voxel erosion was used to shrink the particles and separate them using a "cross" method with a kernal size of 3. Once eroded, additional aggregate outliers were manually separated as before. For both samples a histogram was then generated to determine mean particle size. For both samples the binning was set to 1024.

5.2.7 Zeta Potential Testing

Liquid metal and MXene zeta potential were measured in a DTS1070 folded capillary zeta cell by a Malvern Zetasizer Nano ZS particle size analyzer. $10\,\mu L$ of the liquid metal and MXene suspension were diluted with $10\,mL$ of distilled water before zeta-potential measurements.

5.2.8 Data Processing

We perform 2D image particle size analysis on SEM images using ImageJ software. The image was thresholded to create a binary image, where the filler appears as bright areas and the matrix as dark areas. A built-in particle analysis is utilized to calculate these separated areas. The radius is calculated assuming circular areas and is plotted as histograms.

5.3 Composite Synthesis

Contributions: I led material design, fabrication, and characterization. Yafeng Hu assisted in material design, fabrication, and characterization.

MXene-Liquid metal composites were first prepared by alloying gallium (75 $wt\%$) and indium (25 $wt\%$) to form room temperature liquid eutectic gallium indium (EGaIn). I used tip sonication for processing of bulk EGaIn into nano-droplets. An 80:20 DMSO:DI water solution was used for MXene-LM processing. DMSO is a polar aprotic solvent that stabilizes, and when introduced with sonication, exfoliates MXene sheets and mitigates MXene aggregation and crashing out during synthesis [193]. This DMSO solution was degassed, removing additional oxygen species to eliminate the growth of additional oxide which can prohibit breakup of EGaIn droplets to the micron and sub-micron scale during tip sonication [29]. The EGaIn was then added and tip sonicated breaking up the bulk LM into droplets. A small microtip was used as this tip size focuses the acoustic energy to break up the relatively large amount of EGaIn (14g). Due to the oxygen in the solution, a Ga_2O_3 layer immediately formed

on the EGaIn, coating the particles with this self limiting layer, stabilizing the particles and stopping recombination.

The MXene solution was then added to the vial. The MXene solution itself was prepared using an HF etching technique from a MAX precursor, in this case being Ti_3AlC_2. Once etched and exfoliated using sonication, the MXene sheets were on the order of 500 nm-5 μm in diameter and 5 nm thick [200, 192]. The MXenes were suspended in an 80:20 DMSO:DI water solution with 10 wt % $Ti_3C_2T_x$ MXene. The MXenes exhibited a strong negative zeta potential of -52 mV when diluted in DI water, indicating strong stability of the colloidal suspension (Figure D.1a) [193]. The bulk conductivity of the $Ti_3C_2T_x$ MXenes after vacuum filtration into a film was $5.2 \times 10^4 \pm 2.0 \times 10^3 S/m$.

To wrap the MXenes around the LM droplets, the MXene-LM solution was sonicated a second time to fully exfoliate the MXenes and to coat them onto the EGaIn. I hypothesized that wrapping occurs due to van der Waals interactions in particular, the London dispersion force. Electrostatic interactions may also play a role as MXenes and LM have large differences in zeta potential surface charges (Figure D.1a-b). It should be noted that these zeta potentials are pH and solvent dependent with the data shown in Figure D.1 conducted after the particles were diluted heavily in DI water without DMSO. Results in other solvents indicated lower zeta potentials for LM. This leaves inconclusive evidence of electrostatic interactions. This zeta potential data more so highlights the colloidal stability of MXenes and the colloidal instability of LM with its strong negative and near zero surface charges respectively. Separately, $50\mu L$ of the sonicated MXene-LM solution was dropcast into 10 mL DMSO:DI Water solution to heavily dilute the composite. The solution was then planetary mixed at 2000 rpm for 2 minutes. When dropcast and SEM imaged, the MXene-LM coatings were strong enough that virtually all of the visible MXene was coated around and between the LM clusters forming small scale aggregates on the order of $5-30\mu m$ (Figure D.2a-b). This was done to evaluate adhesion between the MXenes and LM.

Once second stage sonicated, the MXene-LM solution was then vacuum filtrated removing

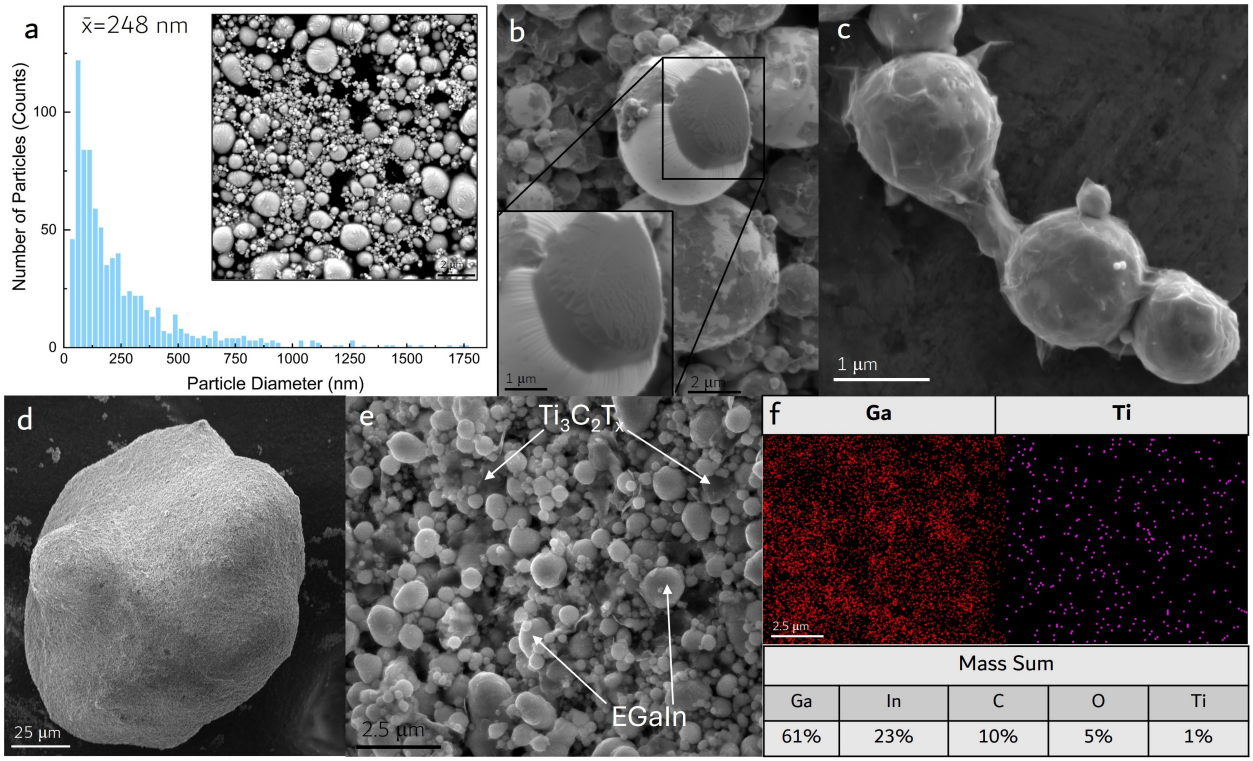

Figure 5.2: **a**, Particle size statistics histogram of a representative sample of LM droplets after probe sonication for one hour with an average diameter of 258 nm. Inset: SEM Image of EGaIn micro-droplets after sonication used in particle size analysis. **b**, 1kV low accelerating voltage SEM image of EGaIn droplets with a partial $Ti_3C_2T_x$ coating adhering to the LM surface after processing. Inset: high-magnitude image highlighting the MXene sheets generating a tension and wrinkling on the Ga_2O_3 skin of the partially coated EGaIn droplet. **c**, SEM image of LM droplets being coated and connected with a network of conductive MXene flakes. Image taken from a sample with 5.8 vol % MXenes. This particular sample was prepared in a fairly low oxygen environment (200 ppm O_2) with a nitrogen purge of the MXene solution followed by the addition of bulk LM. The MXenes and LM were then probe sonicated together for 5 minutes in a low O_2 environment. **d**, SEM image of a conductive MXene-LM aggregate formed after planetary mixing in silicone oil. The aggregate was recovered through toluene dilution and the composition contains 5 vol % MXene. **e**, Surface profile of the 5 vol % aggregate shown in Figure 5.2d highlighting intermixed MXene and LM regions. **f**, Top: elemental mapping of the aggregate surface in Figure 5.2e with gallium representing the EGaIn regions, and titanium representing $Ti_3C_2T_x$ regions. Bottom: The total mass sum of all elements present is shown.

the solvent and leaving the wrappped MXene-LM particles in a paste form. The material was then immediately transferred to a mixing cup with silicone oil then added. A high viscosity silicone oil was selected as the matrix material to decrease settling and phase separation (60,000 cSt @ 25 $°C$). A non-curing matrix material was selected for ease of characterization and testing since the material could repeatedly be used in compressive thermal and electrical

testing as well as microCT imaging without curing. The composite was then hand mixed and planetary mixed for three cycles, causing the MXene-LM particles to aggregate. The sample was placed in an oven to evaporate any remaining solvent.

5.4 Particle Characterization

Size analysis was conducted on LM particles after first stage sonication to better understand size and size distribution. The sonication parameters produced EGaIn particles with an average diameter of 248 nm (Figure 5.2a). The size and monodispersity of these LM droplets as shown in the inset of Figure 5.2a were small enough to where individual MXene flakes ($500nm - 5\mu m$ diameter) can wrap and coat the droplets making them conductive and functionalizing their surface.

As discussed in the fabrication process, when even a small amount ($> 0.25wt\%$ MXene) of $Ti_3C_2T_x$ MXenes were added to the LM micro-droplet solution and sonicated for the second time, the MXenes-wrapped around the surface. In one example, multiple MXene sheets were shown to have partially adhered to the surface of the LM. The MXenes bonded so well to the Ga_2O_3 skin that the MXenes induced a tension, which caused a wrinkling on the Ga_2O_3 surface. Full wrapping around the Ga_2O_3 skin of the LM droplets is shown in Figure 5.2c with conductive pathways being formed around and between the LM droplets. This MXene wrapping also induced a clustering of LM droplets together forming micro-clusters of conductive networks of LM particles. Even after dilution and mixing at 2000 rpm for 2 minutes the LM particles were still held together and wrapped by the MXene flakes (Figure D.2a-b). Due to the 2D nature of MXenes, I discovered that SEM microscopy of individual MXene sheets can oftentimes be difficult, since high accelerating voltages will cause the electron beam to penetrate through the surface giving false surface profiles. 1 kV SEM microscopy was conducted to characterize the surface morphology and interactions of the MXene-LM boundary layer with superior resolution (Figure D.3).

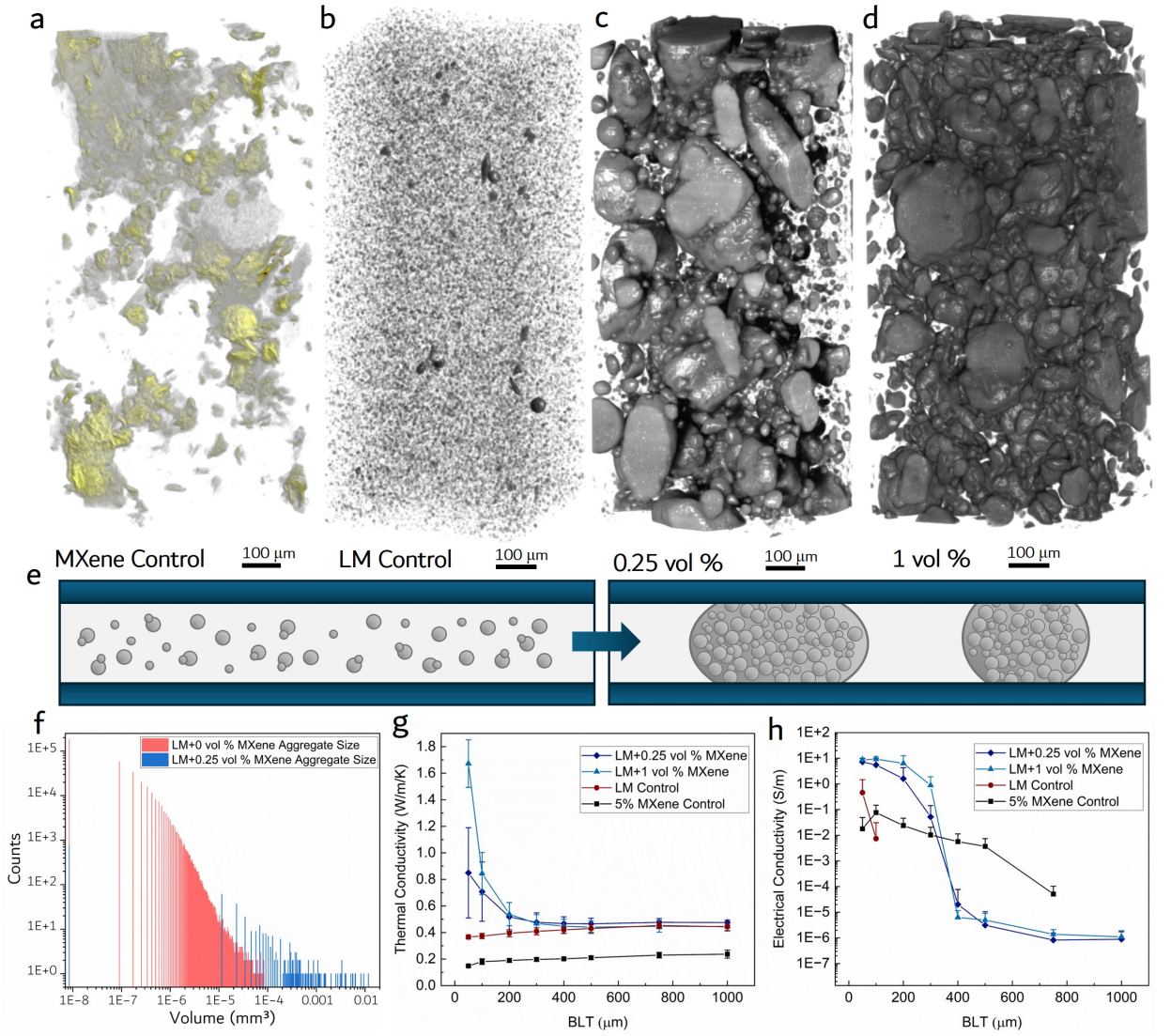

Figure 5.3: **a**, Intensity based heat map of a MicroCT 3D reconstruction of 5 vol % MXene control sample. **b-d**, Intensity calibrated grey-scaled MicroCT 3D reconstructions of LM+0 vol % control, 0.25 vol % MXene, and 1 vol % MXene suspended in a silicone oil matrix material. **e**, Diagram indicating the change in the percolation threshold with and without the MXene coatings functionalizing the surface and inducing aggregation. This change leads to emergent thermal and electrical properties. **f**, Histogram of individual aggregate volumes for LM+0 vol % control sample and LM+0.25 vol % sample with a 3 order of magnitude average aggregate size increase. **g**, Thermal conductivity measurements vs BLT for control and MXene-LM samples highlighting an exponential increase in thermal conductivity as BLT decreases. **h**, Electrical conductivity vs BLT for control and MXene-LM samples indicating a large increase in conductivity with a small volume fraction of MXenes.

5.5 Cluster Aggregation

Silicone oil was then added to act as a matrix material for the composite. This was followed by planetary mixing, which caused the micro-clusters within the matrix material to form large aggregates. MicroCT imaging was conducted to analyze particle aggregation of the MXene-LM composites as the MXene content was varied (Figure 5.3a-d). See the experimental section for additional details on the microCT Imaging. A low MXene filler sample and high MXene filler samples were prepared along with a liquid metal control and MXene control (Figure 5.3a-b). The MXene control contained 5 vol % MXene suspended in silicone oil, and the LM control contained 25 vol % LM. The low MXene filler sample contained 0.25 vol % MXene as a total volume fraction of the entire composite and 25 vol % LM. The high MXene filler sample contained 1 vol % MXene and 25 vol % LM. MicroCT imaging was conducted for each sample (Figure 5.3c-d). The LM control samples indicated no aggregation when compared to functionalized MXene-LM composites (Figure 5.3e). The LM control sample had an average EGaIn cluster size on the order of $10^{-7} mm^3$ (Figure 5.3f). These small droplets and clusters are evenly distributed and well below the percolation threshold needed for electrically conductive composites. These microCT reconstructions were intensity calibrated and threshold segmented.

Due to the instability of MXenes sheets and their tendency to crumble and crash out in non-polar non-aprotic solvents or in environments with non-neutral pHs, the MXene control sample was prepared separately. Without EGaIn particles present for the MXenes sheets to wrap around and stabilize, it is not possible to remove the solvent without a large film of intercalated MXenes forming. To circumvent this issue, the MXene solution was added to silicone oil directly during the fabrication process. This solution was then placed on a hot plate and shear mixed, to mitigate the aggregation of the MXenes as the DMSO:H_2O solution evaporated. The resulting MXene control sample was imaged using microCT (Figure 5.3a). The reconstruction instead indicated the formation of large MXene layered sheets throughout the sample. These most likely formed during solvent evaporation. I believe this

occurs as the removal of the stable DMSO solution and the addition of the silicone matrix material induced a charge instability on the MXenes in the colloidal solution. This led to "crashing out" and aggregation of the material. Images of the crumpled MXene clusters after they have been removed by diluting the sample in toluene to remove the silicone oil are shown in Figure D.4.

When a small amount of MXene was added to the LM (0.25 vol % MXene), the composite formed large aggregates dissimilar from the MXene and LM control samples (Figure 5.3c). The aggregates were made of tightly packed micron sized MXene wrapped LM droplets as shown in Figure 5.2e. Particle analysis conducted on the low 0.25 vol % MXene aggregate sample (Figure 5.3c) showed an average cluster size of $10^{-4}mm^3$, a three order of magnitude increase over the LM control (Figure 5.3g). This large aggregate formation was hypothesized to be a function of the planetary mixer's centrifugal forces generating friction in the high viscosity silicone oil (60,000 cSt), inducing interactions between the "sticky" micro-clusters forming larger aggregates during mixing. When a LM+1 vol % MXene sample was prepared (Figure 5.3d) was prepared and compared against the same filler content prepared in a lower viscosity silicone oil (23,000 cSt), the aggregates were not found to have formed (Figure D.5). The low viscosity sample resembled that of the LM control (Figure 5.3b) and not the sample shown in Figure 5.3d.

To analyze the individual aggregate properties, aggregates themselves were recovered from the matrix material for analysis. This was done by orbital shaking of the composite material in a toluene bath for 15 hours. SEM imaging revealed the surface properties and morphology of the aggregates as shown in Figure 5.2d. A higher resolution image of the aggregates surface (Figure 5.2e) highlights the dense EGaIn particles connected by the $Ti_3C_2T_x$. EDS of this surface confirms this (Figure 5.2f) with large large gallium, indium, and oxygen emissions emanating from the EGaIn along with carbon, oxygen, and titanium emissions emanating from the intermixed and coated $Ti_3C_2T_x$ sheets (Figure D.6).

5.6 Thermal and Electrical Characterization

Lastly, I used a thermal interface material analyzer to measure thermal and electrical conductivity measurements vs BLT of our samples. To understand the implications of aggregate formation on bulk thermal and electrical properties, samples were compressed from $1000\mu m$ to $50\mu m$ with electrical thermal measurements being recorded. LM control thermal conductivity was stable vs BLT with an average of $0.41 \pm 0.03 W/m/K$ (Figure 5.3g). This is in line with effective medium theory which predicts a thermal conductivity of $0.50 W/m/K$ at a $25 vol\ \%$ [185]. Performance was stable vs BLT since the micron scale EGaIn droplet diameters are a 2-3 orders of magnitude below the BLT measurement range. At these sizes, the bulk properties of EGaIn, namely a thermal conductivity of $26.4 W/m/K$ [177], are not a major factor. For TIMs with large inclusions, compression of the TIM below the inclusion size would induce an increase in thermal conductivity as the bulk properties of the material begin to dominate performance. The 5 vol % MXene control sample indicated similar BLT independent properties with an average thermal conductivity of $0.20 \pm 0.03 W/m/K$ showing no improvement over bulk silicone oil or elastomers.

In contrast, With the addition of 0.25 vol % and 1 vol % MXene, thermal conductivities increased exponentially as the BLT began to decrease below $300\mu m$ (Figure 5.3g). Additional data of trials of other MXene filler contents highlighting similar trends are given in Figure D.7 along with corresponding microCT images in Figure D.8. A vol % of 0.1 indicated similar results to the LM control but with still some aggregation occurring at such a low vol % (Figure D.8). For samples with 0.25 vol % MXene or more, when the BLT was compressed to distances approaching the diameters of the individual aggregates, the bulk properties of the compressed aggregates began to play a role in composite performance. This led to a large increase in thermal conductivity. This increase occurs at $300\mu m$ near the size of the MXene-LM aggregates, as expected. At $50\mu m$ the 1 vol % MXene-LM composite had a thermal conductivity of $1.67 \pm 0.18\ W/m/K$ a 4.6× and 11.3× improvement over the LM control and MXene control respectively. Due to the stochasticity of this material system, I

are not making claims on the comparative performance of the MXene fill content but only that the addition of MXene above 0.25 vol % produces an exponential increase in thermal performance at low BLT.

Electrical conductivity indicated a similar trend. The LM control sample acts as a dielectric and was not electrically conductive until 100 μm. This electrical conductivity may have been caused by LM droplets that were not properly sonicated during fabrication. the MXene control sample was exhibited a less dramatic increase in electrical conductivity with a peak conductivity on the order of 10E-2 S/m. The 0.25 vol % and 1 vol % MXene-LM composites again indicated an exponential increase in electrical conductivity generally below 400μm (Figure 5.3h). Conductivities improved 7 orders of magnitude from $10^{-6} S/m$ to $10^{1} S/m$. Again the stochasticity of these composites made it such that differentiating between electrical conductivity and MXene content was not possible. Additional data can be found in Figure D.7.

5.7 Conclusion

In conclusion, this work investigated the introduction of $Ti_3C_2T_x$ 2D MXenes sheets onto EGaIn micro-droplet liquid metal composites, for the enabling of MXene wrapped EGaIn particles. These functionalized MXene-LM micro-cluster particles have a sticky surface with a tendency to aggregate when introduced to a silicone oil matrix material, inducing large clusters on the order of a few hundred μm. SEM imaging confirmed and highlighted the MXene wrapped LM particles. MicroCT was conducted, comparing the non-aggregated LM composites with the aggregated MXene wrapped LM composites. Individual clusters were recovered from the matrix material with EDS confirming the existence of MXenes and LM in the large aggregates. Lastly, thermal and electrical characterization was conducted indicating exponential BLT dependent properties of the composites with increase in thermal conductivity and electrical conductivity at low thicknesses.

5.8 Lessons Learned

Various soft material architectures have been introduced thus far in this thesis highlighting their ability to replace many of the rigid components found in electronics devices. Continuing to increase the electrical and thermal performance of soft materials is of the utmost importance to continue to move this field forward. One potential way to address this is to introduce 2D conductive materials into soft composites. In this chapter, I introduce $Ti_3C_2T_x$ 2D MXenes into soft composites materials to better understand how 2D materials can influence the performance of LMEE composites. I introduce a synthesis method to wrap MXenes sheets around LM particles. These MXene-LM composites are then shown to aggregate into large clusters influencing the thermal and electric properties of the composite. These results are confirmed through a combination of SEM and microCT imaging. The material architecture introduced in this chapter aims to be a fundamental study on how to prepare MXene-LM composite materials.

This work is important in the overall context of this thesis because future improvements in soft electronic devices, including TEDs, will need continued improvements in the soft materials used. This chapter introduced MXenes as one such option for how soft composite material properties can be controlled and improved for future applications. The MXene wrapped LM particles indicated large aggregation and morphology changes when compared with soft composites that contained just LM. This material architecture has applications in the TIM space. In particular, MXene-LM soft composites open new directions to replace the TIM materials used in the TEDs introduced in this thesis. In the future, TIMs, such as the LM-Epoxy introduced in Chapter 4, may be replaced with more advanced MXene-LM composites.

Chapter 6

Conclusions and Future Work

6.1 Summary of Research Directions

With the expansion of wearable health monitoring systems for long-term patient monitoring, a new generation of power sources is needed to power these wearable devices. Wearable TEDs are a potential solution to this need. These devices are usually made from rigid materials that are not conformable or comfortable to the wearer. To bridge this divide between performance and conformability, this thesis introduced a new generation of soft material-based energy harvesters designed and built to power wearable sensors. In particular, TEGs were designed from a materials first perspective to replace the rigid device packaging components of traditionally rigid TEGs. This included replacing TIMs and interconnects with soft and stretchable liquid metal soft composite materials. Three generations of these devices were introduced here with large improvements being made in power output. Applications in thermally responsive LCE actuation along with demonstrations of these TEGs powering a PPG monitoring system were demonstrated. Lastly, to explore future improvements in TIMs, MXene 2D sheets were introduced to augment LMEE composite performance. MXenes were introduced as a novel method to influence the morphology and performance of these soft thermal composites.

6.2 Limitations of Current Research Directions

This thesis has introduced soft TEDs, replacing rigid components with soft and stretchable ones. Future research efforts in the field of wearable thermoelectric energy harvesting should move away from the last rigid component: rigid semiconductors. Rigid thermoelectric semiconductors are prone to fracturing and shearing along grain boundaries leaving them exposed to damage when introduced into wearable applications. This is especially true for commonly used Bi_2Te_3 which have a vickers hardness (Hv) of 0.62-0.79 GPa [202]. Traditional thermoelectric materials are fabricated by various crystal growth methods[203] and high temperature annealing processes including hot pressing[204]. This process requires temperatures often times above 500 °C. While effective for fabricating crystals with high figures of merit, the fabrication process produces rigid and brittle materials. The rigid and brittle nature of Bi_2Te_3 leads to small thermoelectric elements with low aspect ratios. This is a weakness for energy harvesting, as increasing the distance between the opposite ends of the semiconductors is important to mitigate heat transfer.

Rigid TEDs mitigate this issue through the rigid device packaging components that are surrounding the thermoelectric legs (i.e. ceramic or metal TIMs and copper interconnects as described in this thesis). Further more, traditional TEG applications do not require bending of the harvester during operation i.e. use cases in refrigeration, automotive waste heat recovery, and CPU and diode cooling [205]. Wearable TEDs lack this advantage as these devices continually need to be deformed during movement. As this thesis has demonstrated, all of the device packaging components including TIMs, interconnects, and substrate can be made bendable and stretchable.

These devices still require rigid semiconductors. This has two potential issues. 1) contact resistance at the soft rigid interface. While the stretchable TEGs introduced in this thesis have been shown to perform well under strain, with trivial to no changes in resistance increase during cyclical loading, a large part of the overall device resistance is still caused by contact resistance. 2) The elastomers and stretchable electronic materials introduced

here will not protect the semiconductors from impacts. To address issues for rigidity and aspect ratio, a new generation of soft thermoelectric materials is needed to address these drawbacks.

6.3 Future Directions for Wearable Thermoelectrics

The semiconductors themselves will need to be made deformable for improved performance. Additive manufacturing of thermometric materials has arisen to address these issues [180]. Semiconductor powders embedded in epoxies are one approach that has been of interest in recent years. While flexible this architecture leads to high resistances with peak power outputs of less than 50 nW for 10 $K\Omega$ load resistances and the ability to screen print only thin layers[206]. A recent paper has focused on oxidizing Bi_2Te_3 particles to increase their zeta potential to zero to mitigate instability when combined with ChaM ion additives[207]. This allows for printable inks with an excellent viscosity for DIW printing. Once printed, the ChaM additives promoted sintering which occurred at 450 °C with a 36 % volume contraction. The completed thermoelectric was not deformable or flexible. ChaM additives have become popular with other approaches using the advantages of DIW printing to print multilayered devices with each layer corresponding to a different peak ZT (figure of merit) temperature. Each semiconductor exhibits peak properties at different temperature ranges to optimize overall figures of merit over a larger temperature range. This novel approach highlights the advantages of DIW but again requires high-temperature annealing making rigid devices [208].

6.3.1 Liquid Metals as a Potential Solution for Printable Thermoelectrics

Separately liquid metals have been explored for their ability to wet onto surfaces through a gallium oxide layer that forms on the surface when exposed to air[209]. This oxide layer

modulates the surface tension. Work has shown that this surface tension can be controlled by removing the oxide layer through chemical and electrolytic approaches. This has enabled EGaIn-based actuators in which the modulation in the surface tension in an electrolytic solution is able to generate fast repeatable actuation. Research has shown that a redox reaction occurs when EGaIn is submerged in a bath of KOH with $V = \pm 2.5V$ allowing for volumetric changes of EGaIn. Using this low surface tension to researchers' advantage EGaIn has shown abilities to wet onto copper and silver to form new alloys such as AgIn. when strained, the EGaIn fills in any cracks caused by the silver layer[98, 210]. This approach creates material architectures that can be aligned with high tolerances and operate under extreme strains.

There is the potential to address the issues of high-temperature annealing that lead to losses in flexibility and deformability post-sintering. By introducing EGaIn as a binder material for Bi_2Te_3 powders and embedding these particles inside a SIS:toluene solution, there is the potential to fabricate 3D printable semiconductors that can stretch and deform without losing significant performance. Recent work has shown that SIS:toluene is an excellent candidate for conductive DIW inks[176, 175, 211]. Once deposited the toluene evaporates, inducing a volumetric contraction on conductive traces.

Separately, recent work has shown Bi_2Te_3 and EGaIn electrostatic bonding caused by oppositely charged surface zeta potentials. Zeta potentials are the electric potential at the slipping/shear plane of a colloid particle when under an electric field[212]. By controlling surface potentials of the Ga_2O_3 or functionalizing the surface using thiol based chemistries there is the potential to introduce LM as a binder for thermoelectric particles. Recent work has shown a similar phenomenon with reduce graphene oxide (rGO) and LM nano-particles (LMNP) electrostatically self-assembling [213]. While EGaIn has a strong positive zeta potential, Bi_2Te_3 has a negative potential similar to rGO making it potential candidate for electrostatic self-assembly. Recent work on direct ink writing thermoelectrics has shown that non-oxidized Bi_2Te_3 has a zeta potential of $\sim -25mv$ [207]. Zeta potentials are often

solvent and pH dependent making the choice of solvents and pHs used important during synthesis. A recent study has shown a similar ability of Bi_2Te_3 to self-depose onto EGaIn. By submerging EGaIn in an HCl solution, the interfacial Ga atoms increase in their oxidation state generating an interfacial potential of $\sim -400mV$ and reacting with Bi_2Te_3 once the solution is deposited [214]. In conclusion, to develop thermoelectric semiconductors that can be DIW printed and stretchable, LM additives have the potential to act as one such solution.

Appendix A

A.1 Predicted Power Loss due to Internal Resistance Change

A simple model is used to predict the change in power of stretchable thermoelectric generators (TEGs) as a function of resistance change. The generated power can be expressed as $P = R_{int}(\frac{V}{R_{int}+R_{ext}})^2$, where R_{int} is the internal resistance of energy the harvester and R_{ext} is the external load resistor in parallel with TEG device, while V is the measured voltage across the load resistor[109, 215]. The maximum power is produced when the load resistor is equal to the internal resistance (resistive impedance matching). After determining the optimal resistor (for example $R_{ext} = R_{int} = 15\Omega$), the wearable TEG can be subjected to various mechanical deformations (such as bending, torsion, tension, and compression) leading to an increase/decrease in the overall internal resistance. For instance, a compression force can reduce the contact resistance and improve the electrical connectivity, while tensile deformation of the TEG leads to increased contact resistance at the interconnects. If we assume a constant voltage of 130 mV and a resistance fluctuation of $\pm 5\Omega$ from the initial internal resistance value (equivalent to $\pm 33.3\%$ resistance change for this TEG device), the changes in power will remain below 4%. This result is shown in Figure A.1, indicating that deviation from a fixed optimal load resistor will lead to a small power loss under the assumption of constant output voltage from device.

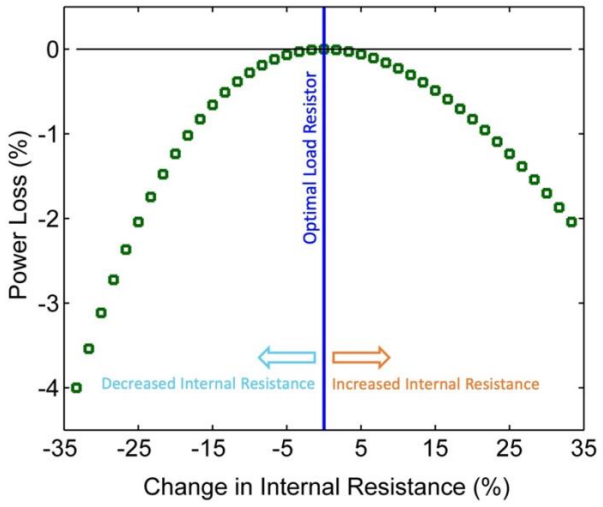

Figure A.1: Estimated power loss in stretchable thermoelectric devices under mechanical deformations that can lead to an increase/decrease in the electrical resistance of TEG device.

Appendix B

B.1 Soft Robotic Walker Supplementary Figures

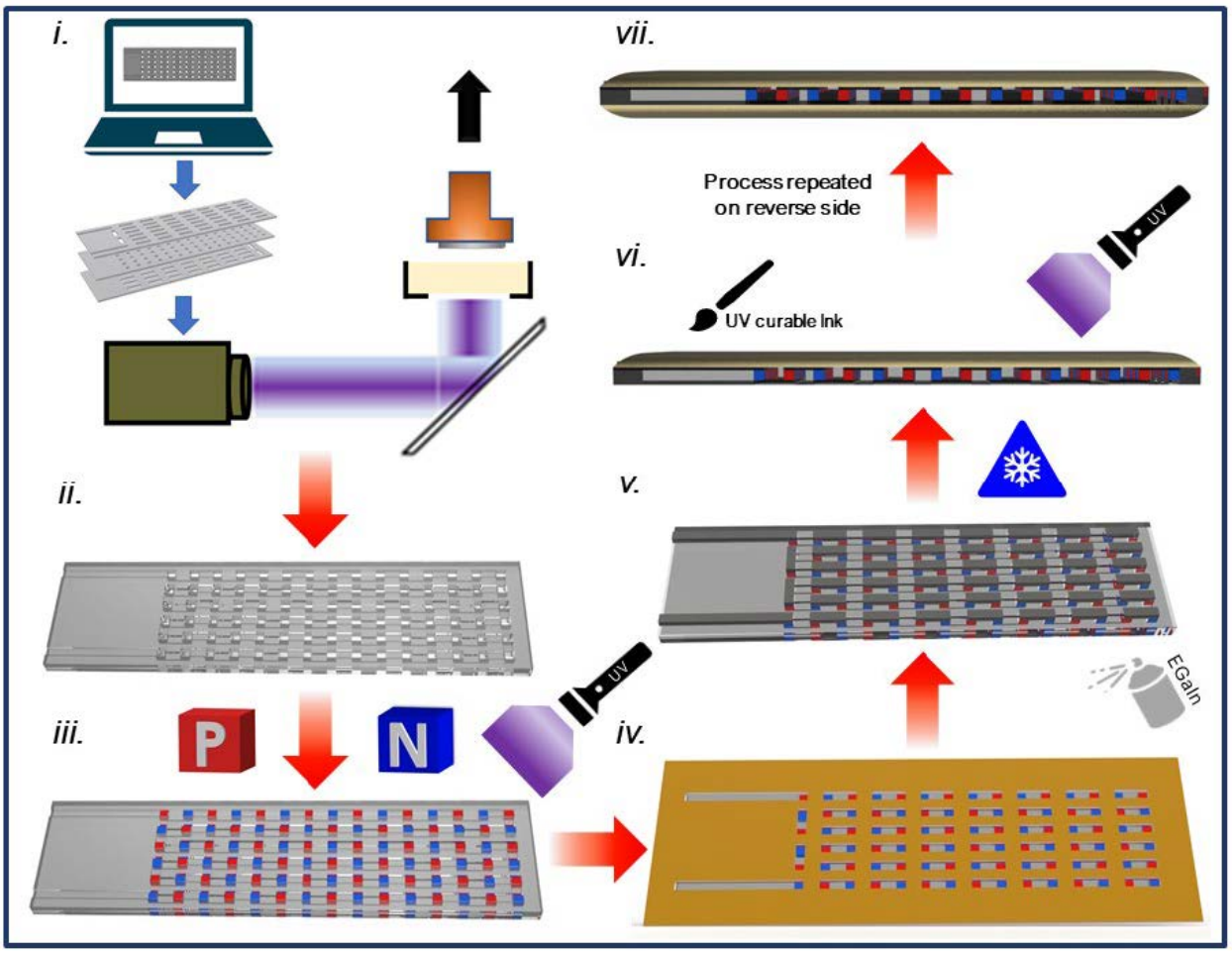

Figure B.1: **i-ii**, center layer and semiconductor substrate is printed using DLP printing process **iii**, P and N doped semiconductors are placed into the center layer and UV cured sealing them **iv**, A stencil is place overtop the center layer and EGaIn is airbrushed into the channels **v**, the stencil is removed and the device is placed in the freezer **vi**, a UV curable ink is brushed on in a thin layer and cured at 365nm for 12 mins **vii**, the process is repeated on the back side

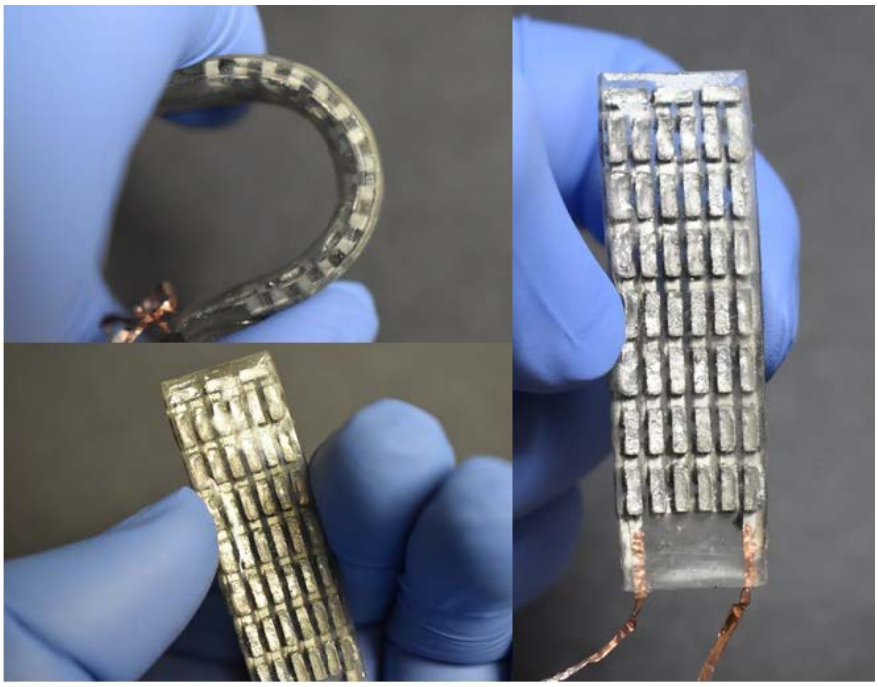

Figure B.2: Images of completed 90 semiconductor TED before LCE has been adhered

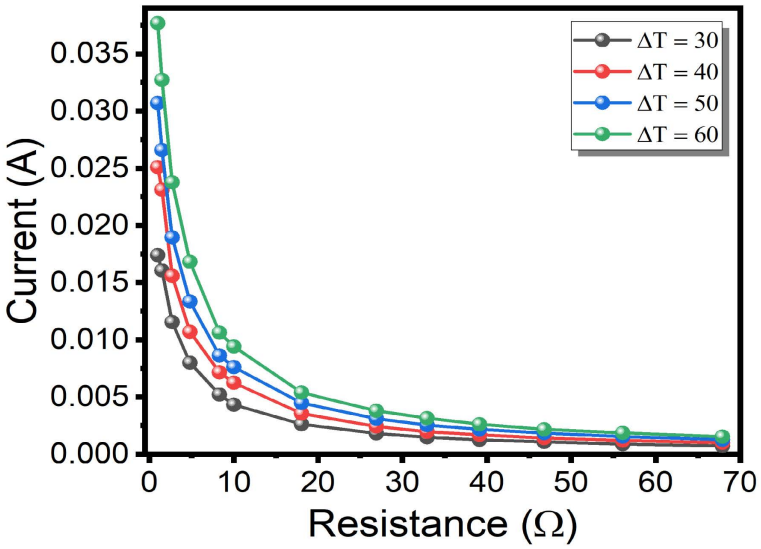

Figure B.3: External resistance vs current for varying temperature differentials generated by a 90 semiconductor TED. At a max temperature differential of 60 ℃ 38 mA was recorded at resistance of 1Ω with current decreasing as resistance increased.

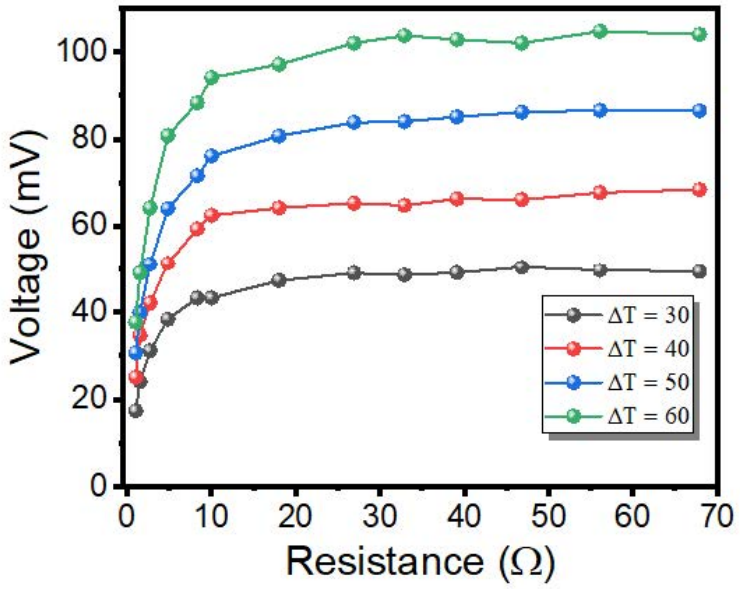

Figure B.4: External resistance vs voltage for varying temperature differentials generated from a 90 semiconductor TED. An increase in resistance corresponds to a voltage that approaches the open circuit voltage above 10Ω.

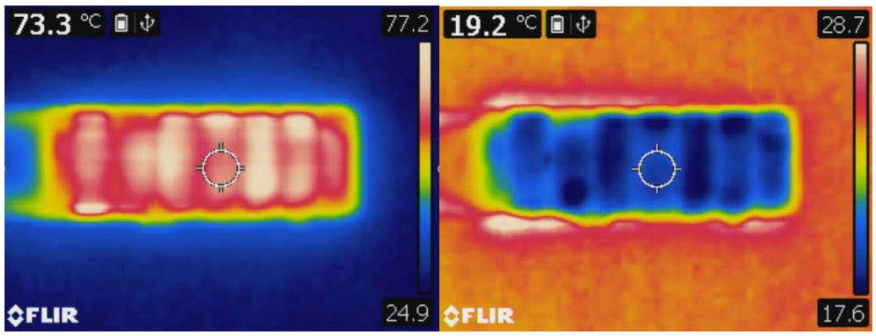

Figure B.5: **a**, 90 semiconductor TED heating at 1.75A after 40s. **b**, 90 semiconductor TED cooling after 14s.

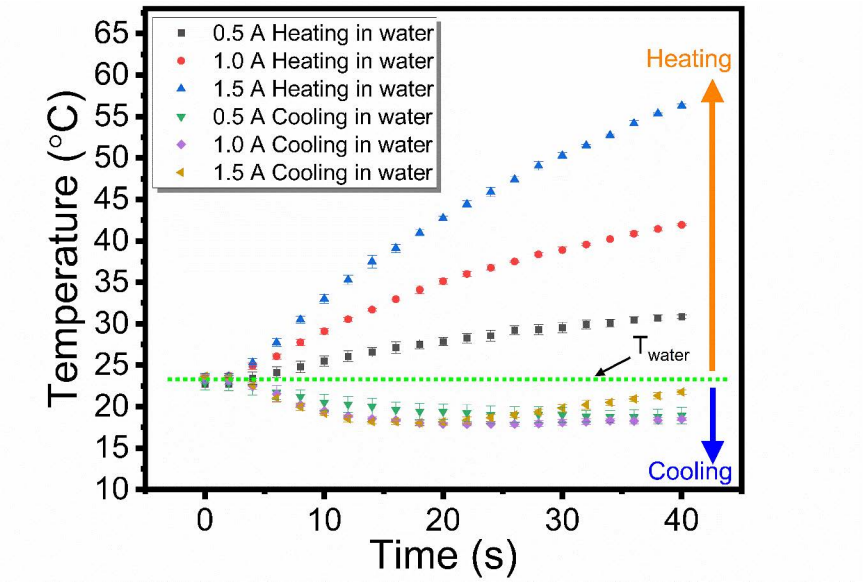

Figure B.6: Comparison of Peltier heating and cooling for various currents. This test was conducted with the underside of the device in contact with water acting as a heat sink, and data recorded from the top side (n=3).

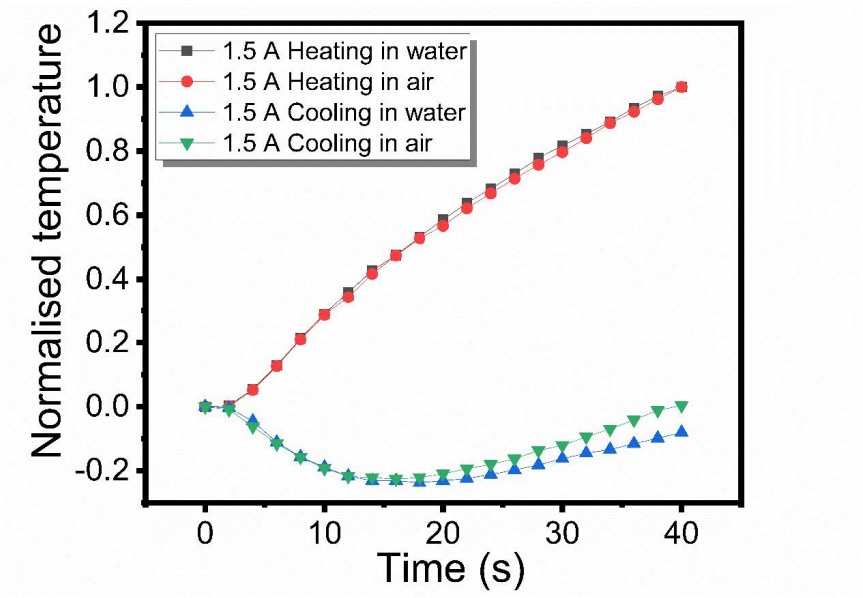

Figure B.7: Comparison of Peltier heating and cooling data for ambient air conditions at 1.5 A (Figure 3.2c-d) and bottom side in water (Figure B.6).

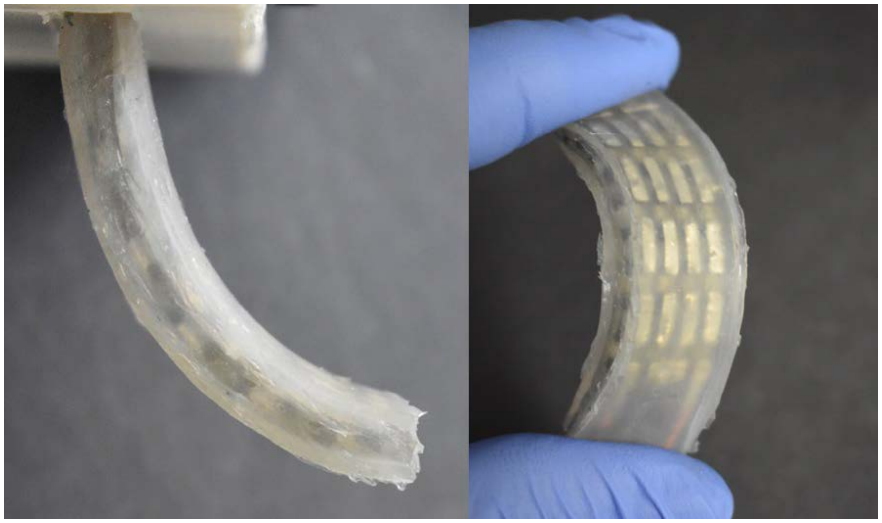

Figure B.8: Images of TEG-LCE Actuator

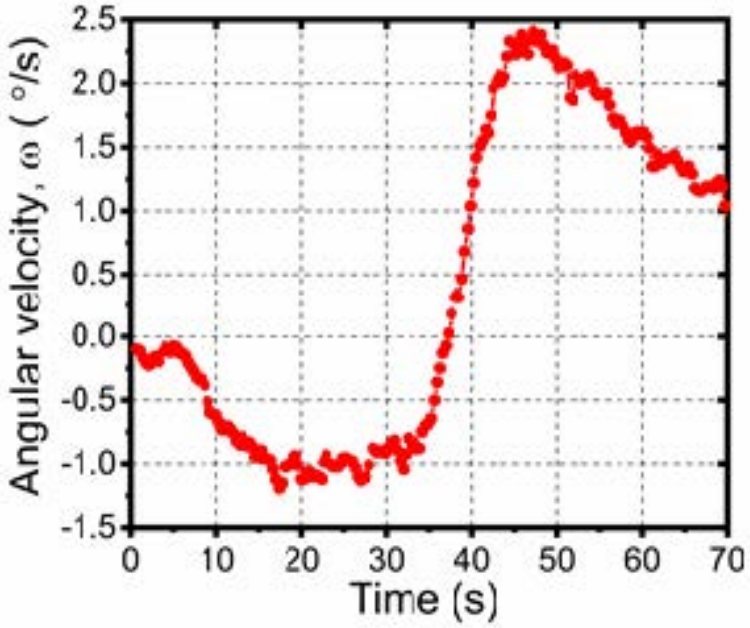

Figure B.9: Angular velocity of 60 semiconductor actuator at 2.9V corresponding to Figure 3.3a

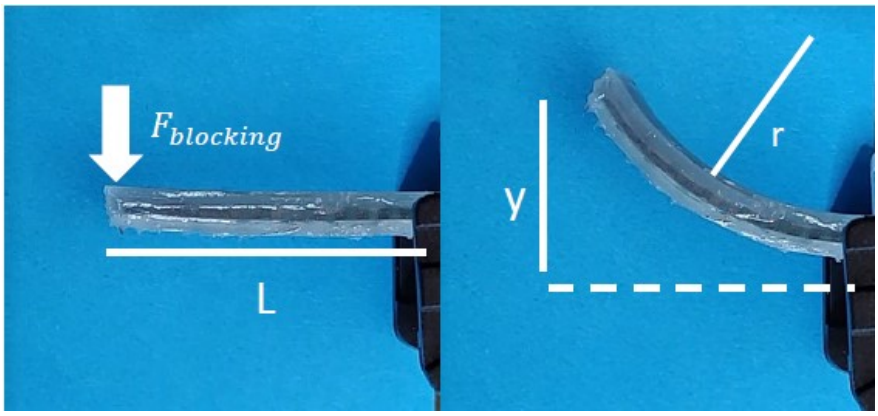

Figure B.10: Diagram of actuator in initial vs actuated position with relevant dimensions for FoM calculations.

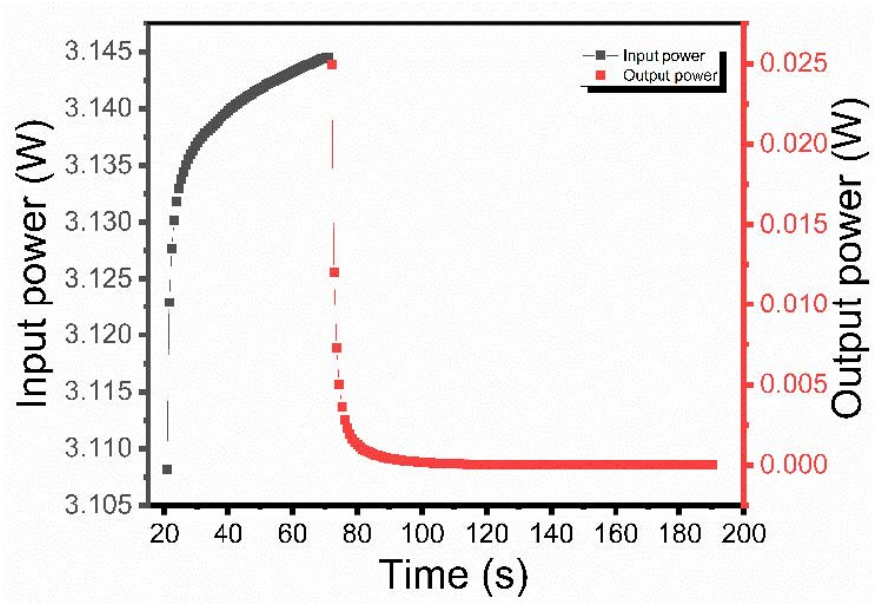

Figure B.11: Input and output power for the regenerative energy harvesting test for one cycle.

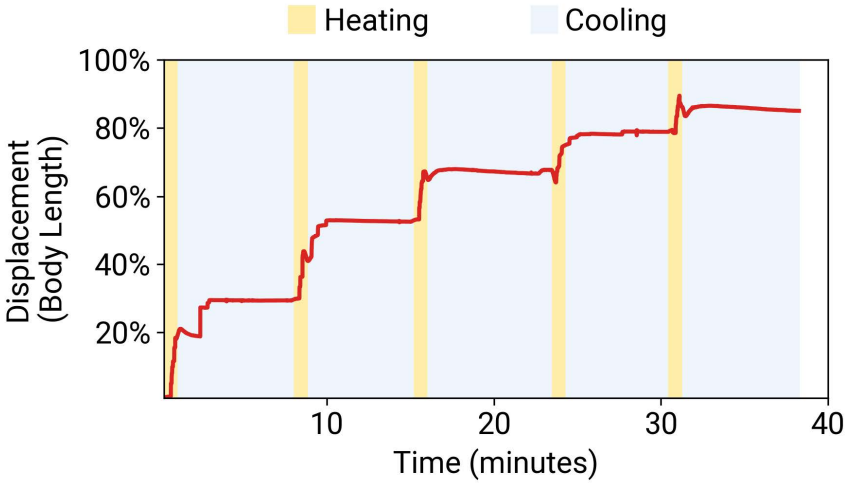

Figure B.12: Graph of position vs time for 5 cycles of the soft robotics walker. Yellow heating sections are represented by the gait mechanics in Figure 3.4c. This is followed by a prolonged cool down time where the actuators passively regenerate energy.

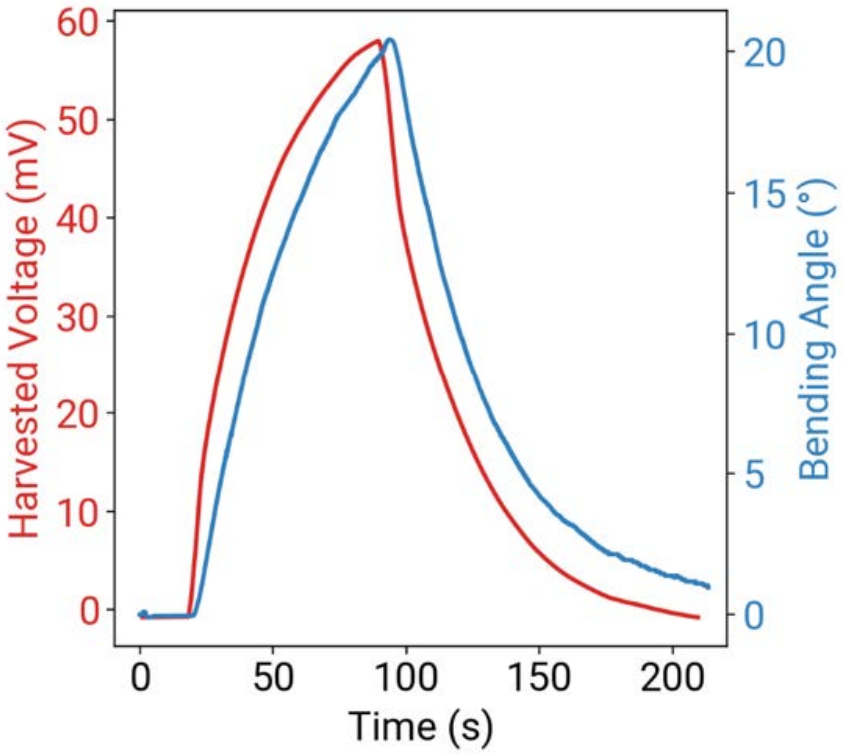

Figure B.13: Bending angle and harvested voltage of LCE-TED bending towards a heat source exhibiting phototropism for increased harvested voltage. See Figure 3.4f for corresponding figure.

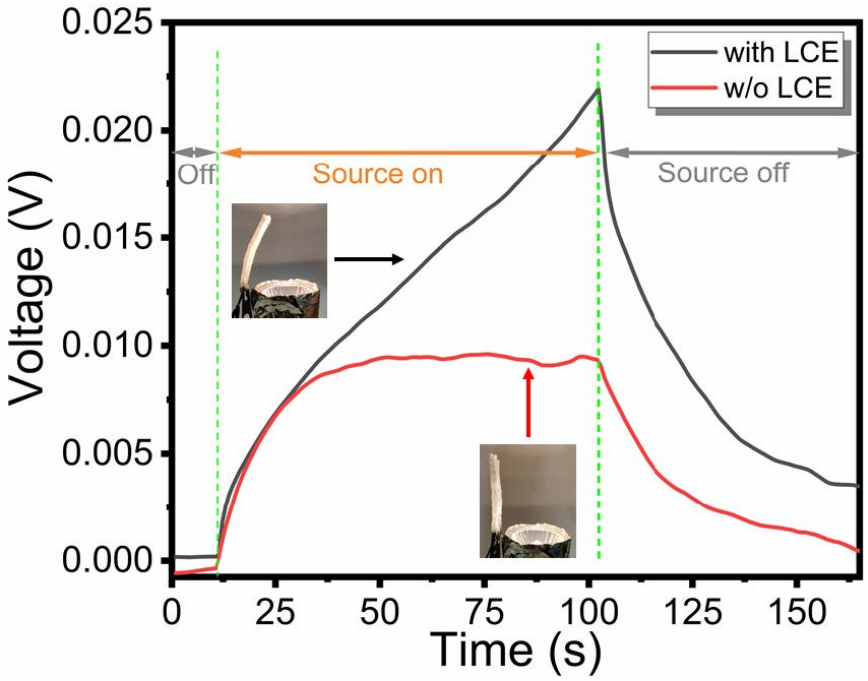

Figure B.14: Results of phototropism inspired energy harvesting test. The transducer was placed above and parallel to a heat source with voltage collected with and without the LCE layer, highlighting the physical intelligence of this system track towards a heat source and increase voltage output.

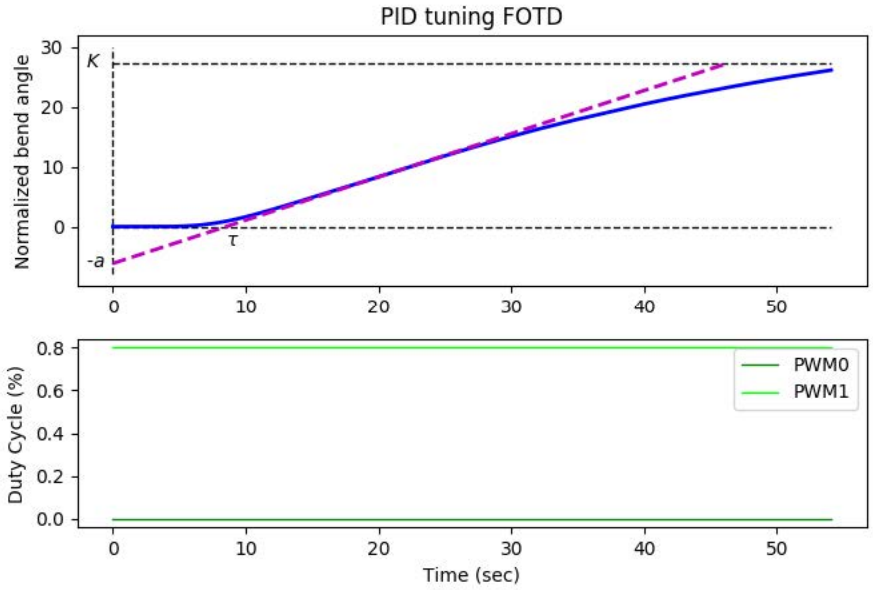

Figure B.15: Step response test for tuning the proportional-integral (PI) controller for the LCE-TED soft limb. An 80% duty cycle PWM signal was applied to the forward-voltage gates of the H-bridge circuit for 55 sec., and the constants $alpha$, K, and τ were measured for use with the first-order plus time delay (FOTD) tuning methods.

B.2 Transducer Efficiency

Following the arguments in Lee et al. [138], we define the figure of merit (FoM) of this transducer as:

$$FoM = \frac{U_e}{U_e + U_t} \tag{B.1}$$

where elastic energy and thermal energy is defined as

$$U_e = \frac{1}{2} D k^2 \tag{B.2}$$

$$U_t = c_p m \Delta \mathrm{T} \tag{B.3}$$

Here, D is the flexural rigidity, k is the bending curvature, $c_p = 1000\ JKg^{-1}K^{-1}$ [65, 51] is the specific heat capacity for the heated LCE layer, ΔT = 43 ºC is the increase in temperature, and $m = 8.4 \times 10^{-4} kg$ is the LCE layer mass for one side.

We determine D and k from our empirical studies on actuator bending and blocking force. First, we note that for a cantilevered beam with an end load $F_{blocking}$, vertical displacement is described as

$$y = \frac{F_{blocking} L^3}{3D} \tag{B.4}$$

where $L = 4.3 \times 10^{-2}$ m is the length of beam and D is flexural rigidity. This relationship is based on Euler-Bernoulli beam theory, which relates a transverse point load and displacement for a beam that is initially straight. However, when the LCE-TED actuator is activated, it bends to form a circular arc. Nonetheless, based on the principle of linear superposition for a Euler-Bernoulli beam, we assume that Equ. B.4 is a reasonable approximation even for a beam that is initially curved.

For an unloaded actuator that is able to freely bend, the maximum bending angle of 27 º occurs at 35s when run at 2.9 V (Figure 3.3a). To estimate the corresponding displacement (y) we must first determine the curvature (k) of the bending actuator in the absence of a block

force load. At 27 º the radius formed by the arc length is $r = 4.1 \times 10^{-2} m$. The curvature k is defined as

$$k = \frac{1}{r} = 24.4 m^{-1} \tag{B.5}$$

and noting that the actuator bends into a circular arc, the vertical displacement that the blocking force load must overcome is calculated as

$$y = \frac{1 - \cos kL}{k} = 0.021 m \tag{B.6}$$

Referring to Figure 3.3e, an actuator that is constrained from bending will exert a blocking force of $F_{blocking} = 0.076N$ when activated at 2.9 V for 35s. Assuming that the actuator behaves like an Euler-Bernoulli beam, this implies that 0.076 N is approximately the force required to displace the tip of the beam by the amount y calculated in Equ. B.6. Combining Equ. B.4 and B.6 implies that

$$\frac{F_{blocking} L^3}{3D} = \frac{1 - \cos kL}{k}$$

Next, solving for D and inserting the values for $F_{blocking}$, L, and k yields

$$D = 1.6 \times 10^{-4} N m^2$$

Lastly, solving for U_e and U_t gives:

$$U_e = 4.80 \times 10^{-2} J$$

$$U_t = 36.12 J$$

This implies a figure of merit (FoM) = 0.0008.

B.3 Regenerative Energy Harvesting Efficiency

To estimate the energy efficiency of the LCE-TED transducer, a 60 semiconductor transducer, external power supply, external resistor, and multimeter (Agilent-34401a) were placed in the below circuit configuration (Figure B.16). This setup allows for continuous data collection in both the Peltier and Seebeck modes. The internal resistance of the device was $R_{TEG} = 2.3\Omega$ with an external resistance of 2Ω for impedance matching. The power source voltage was $V_{tot} = 3.2V$ with V_{ext} being recorded by the multimeter during both Peltier and Seebeck modes (Figure B.8). The power source was cycled on for 50s and off for 6 minutes. P_{input} and P_{output} were calculated:

$$P_{input} = V_{tot} V_{ext} \left[\frac{1}{R_{TEG}} + \frac{1}{R_{ext}} \right] - \frac{V_{ext}^2}{R_{ext}} \tag{B.7}$$

$$P_{output} = \frac{V_{ext}^2}{R_{ext}} \tag{B.8}$$

which were obtained from the relationship

$$P = VI = I^2 R = \frac{V^2}{R} \tag{B.9}$$

Energy was then calculated by numerical integrating power over input and output cycle times with energy efficiency calculated as η:

$$E_{input} = \int P_{input} dt \tag{B.10}$$

$$E_{output} = \int P_{output} dt \tag{B.11}$$

$$\eta = \frac{E_{output}}{E_{input}} \times 100 \tag{B.12}$$

Circuit Diagram

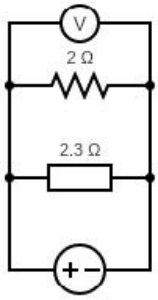

Figure B.16

B.4 Feedback Control Design

Our proportional-integral (PI) feedback controller was tuned using well-known methods from the literature. Thanks to our ability to apply a control input that cools the device - a negative voltage - these tuning rules are now applicable. With heating alone, a PI controller would attempt to apply a negative control input and would incorrectly saturate at 0V.

Tuning of a PI controller can be performed in a number of ways. We chose to use the time domain step response method [216], where a constant control input was applied and various properties of the resulting trajectory are used to estimate the proportional (K_p) and integral (K_i) constants. We chose an 80% duty cycle input step, representative of the actuator during its aggressive operation, mapped to the PWM that controlled the "forward" signal of the H-bridge circuit.

Figure B.15 shows the step response alongside the three tuning constants that are used in the first-order plus time delay method. Note that the approximated time delay, τ, is very large (approx. 8.5 sec), making high-performance control challenging without an accurate system model. Since our actuator can overheat after application of significant power over a long period of time, we chose not to perform a step response test where the system fully settled to a steady-state value.

We used three methods [216] to estimate feedback gains from these step response parameters. These included the Zeigler-Nichols method and its two modifications to include

the settling value of the step response, K (Figure B.15). Averaging the estimated gains gave $K_p = 0.096$, $K_i = 4 \times 10^{(-2)}$. It is well known that these gains, when applied to a nonlinear system, provide only an initial guess. Executing our controller with these gains showed significant oscillations, primarily due to the time delay. After adjustments by hand, our final controller used $K_p = 0.08$, $K_i = 2 \times 10^{(-6)}$, representing significantly lower integral control.

Finally, note that although our PI controller could potentially saturate above 100% or below -100% duty cycle, we did not observe such behavior (Figure 3.4b, main text). As a result, integral windup was not observed and no compensation is needed, though there would be simple techniques to do so if required [217]. Similarly, our controller did not perform the most aggressive actions possible for fast operation: control inputs never reached maximum power, and so the actuator necessarily responded slower than could have otherwise been possible. Many improvements can be made for better performance, including sliding mode control or other model-based methods. However, our simple controller validates the concept while highlighting the benefits of active cooling.

Appendix C

C.1 Voltage Characterization

For TEGs at lower temperatures differentials of 10 °C, the V_{oc} of the LA-HD and HA-HD device was 98±11.8 mV and 147±11.8 mV respectively. The maximum tested voltage output of 545.7±32.5 mV for LA-HD and 865.7±34.3 mV for HA-HD at 60 ºC was recorded. We believe that this peak voltage improvement in HA-HD over LA-HD comes from increasing the amount of thermoelectric material vertically with the incorporation of HA semiconductors. HA-LD under-performs the HA-HD device. At lower temperatures differentials of 10 °C, the V_{oc} was 116±2 mV along with a max tested voltage output of 683.3±39.1 mV at 60 °C. Still, for HA-LD the voltage drop over time is improved over LA-HD.

For HAR devices, increasing the distance between the depletion regions and decreasing the thermal conductance between the hot and cold faces of the device leads to a slower degradation of the thermal gradient and higher voltage output. This was seen in Figure C.6a-b (Supporting Information). Not only was the peak voltage low in the LA-HD device but the percent drop in voltage 60 seconds after the peak is 29.1% at 40 °C and 30.4% at 60 °C compared to 9.5% at 40 °C and 10.5% at 60 °C for the HA-HD device. Similar results were seen for the HA-LD device at 9.4% @ 40 °C and 8.5% @ 60 °C) (Figure C.6c, Supporting Information) much more in line with HA-HD voltage output. This was due to poor thermal management and decreased thermal resistance when compared with the HA-HD device.

HA-LD + LM-epoxy device recorded a V_{oc} at T 10 and 60 °C of 127.0±7.5 mV and 781.3±9.0 mV respectively. When replaced with a control epoxy, V_{oc} decreased to 102.8±1.9 mV and 664.6±2.8 mV at ΔT 10 and 60 °C highlighting the improvements of LM-epoxy in heat transfer into and out of the semiconductor junctions (Figure 4.2e,i). Voltage vs time performance was also improved. An 11.7% @ 40 °C and 8.2% @ 60 °C voltage drop for HA-LD + LM-epoxy compared with 15.3% @ 40 °C and 13.2% @ 60 °C voltage drop after 60 s for HA-LD + control epoxy was found (Figure C.6d-e, Supporting Information). For all HAR devices fabricated, a hollow internal structure of pillars introduced to decrease rigidity as shown in Figure 4.1a. By conducting thermal FEA between simulations involving hollowed vs filled in center layers, a none to negligible decrease in heat transfer for the pillared hollow internal structure was found when compared with the full filled in layer. The corresponding voltage outputs are shown in Figure C.19 (Supporting Information).

C.2 Peltier Performance

For Peltier cooling, mitigating heat transfer across the device was was key. The heat rate (Q_c) extracted from the cold side can be described as $Q_c = Q_p - Q_K - Q_J$ where Q_p is the Peltier cooling term, Q_J is the Joule heating, and the natural heat flux Q_K can be defined as $Q_K = K\Delta T$, where ΔT is the temperature differential across the device, indicating the importance of decreasing conductance to increase thermoelectric cooling. This same principle applies to Seebeck Energy harvesting. This improvement is demonstrated experimentally for both Peltier heating and cooling. At 0.50 A and 0.75 A cooling ΔT peaks at -3.9 ± 0.6 °C at 3.5 s and -4.8 ± 0.7 °C at 2.8 s respectively for LA-HD compared to -10.7 ± 0.5 °C at 13.0 s and -13.0 ± 0.6 °C at 8.8 s respectively for HA-HD. Heating performance confirms this trend with temperature increases at 0.50 A and 0.75 A of 21.5 ± 1.9 °C and 49.1 ± 4.0 °C respectively for LA-HD compared to 39.9 ± 0.5 °C and 84.8 ± 4.0 °C respectively at 45 s for HA-HD.

C.3 Wearable Testing

For wearable testing, the variables considered are bio-mechanical movement, body temperature, and device placement. While it is outside the scope of this work to decouple these parameters, it is of interest to understand generally the influence of these parameters on device Seebeck output. In particular, bio-mechanical movement's influence on increasing the convective cooling rate, the role of exertion on conductive heating from the body onto the TEG, and the influence of device placement on comfort and convective cooling are explored. To accomplish this, an experimental setup was designed with a HA-LD + LM-epoxy TEG embedded with thermocouple temperature sensor on each side. A TEG was integrated into a sleeve with the TEG mounted on the inside of the left wrist. A second device was integrated into a compression shirt and mounted on the left part of the chest (Figure 4.4a). To collect data, each TEG was connected to a wearable ADC for voltage and temperature measurements, a micro-controller, and an SD card writer for data processing and collection (Figure 4.4b). In addition, heart rate was used to measure exertion and was recorded using an ECG (Zoll).

Tests were conducted for sitting, walking (2.0 mph), and running (5.0 mph) conditions on both the wrist and chest. For each test, a baseline test was conducted while sitting followed by either a walk or run. Relative voltage change was given to normalize for differences in manufacturing variance or small changes in ambient conditions. The wrist and chest were chosen for two reasons 1) these locations are both potential and common candidates for wearable sensors, and 2) for their differences in bio-mechanical movement during exercise. We expected the chest TEG to experience less airflow and therefore convective cooling than the wrist-worn TEG.

When comparing wrist and chest-worn harvesters, the influence of increased convective cooling on the wrist-worn device was clear. For the wrist sit-walk test, movement across the device's outside face during walking lowered the air-facing and wrist-facing temperatures

(Figure C.15b, Supporting Information). This increases the temperature differential leading to a 0.2 increase in relative voltage over sitting. For the same test, the chest worn device temperature stayed consistent for both sitting and walking (Figure C.15 a, Supporting Information). This is believed to be attributed to no additional airflow across the device during walking as chest movement is limited while walking on a treadmill. For both wrist and chest-worn devices, there was no increase in body temperature during walking, leading to no Seebeck harvesting increase that would have come from an elevated temperature during exertion. This was confirmed with no increase in heart rate detected during either tests (Figure C.14a-b, Supporting Information).

In contrast to the sit-walk test, the chest worn sit-run test TEG decreased in temperature during running (Figure C.15d, Supporting Information). This was most likely due to the vertical movement of the chest during running. At the start of the run, the chest worn voltage increased with a drop in outside and inside temperature which then began to plateau at 650 s as the inside temperature began to plateau. This was followed by an increase in inside temperature which led to a sharp increase in both temperature difference and relative voltage at the 800 second mark (Figure 4.4c) . This was highlighted further in the wrist worn TEG sit-run test with an initial increase in temperature difference from convective cooling followed by a secondary increase in temperature difference due to the inside temperature increase from skin temperature rise (Figure 4.4d and Figure C.15c, Supporting Information). This rise corresponded to an increase in blood flow and heart rate during the run leading to an increase in skin temperature and ΔT. At 1100 s the relative voltage change was > 1.0 for the wrist-worn device and 0.8 for the chest worn device. These tests indicated a significant Seebeck voltage performance boost during movement, especially on wrist-worn devices and during exercise. Both cooling from bio-mechanical motion and heating from exertion played a major role in TEG Seebeck performance.

While these initial tests helped to inform the influence of bio-mechanical motion and

exertion on TEG Seebeck output, no sit-run tests reached a steady state for voltage or temperature values. A longer test was conducted to determine if voltage would plateau. Additional chest sit-run test data was conducted with a 5 minute walk and 25 minute run. Results are shown in Figure 4.4e. Outside temperature initially dropped due to convective cooling followed by an increase in inside temperature due to the body heating. This led to a large temperature differential which began to reach a steady state at 1000 s (Figure C.16, Supporting Information). When comparing voltage, temperature differential, and heart rate, one can see that these all began to plateau around 1000 s indicating a steady state and stable Seebeck performance. Based on these tests, we can predict large ($> 2X$) consistent Seebeck improvements during exertion. For integration into a fully functional wearable devices, the wrist-worn orientation was selected as it exhibits superior Seebeck performance during testing. These tests help to inform general trends of device placement and exertion on voltage performance along with better understanding how skin temperature will influence voltage output. Other factors such as wind, humidity and an individual's metabolic rate are not explored here and are outside the scope of this work [171]. Future work should focus on a more complete large user study to understand the influence of these factors.

C.4 Supplementary Figures

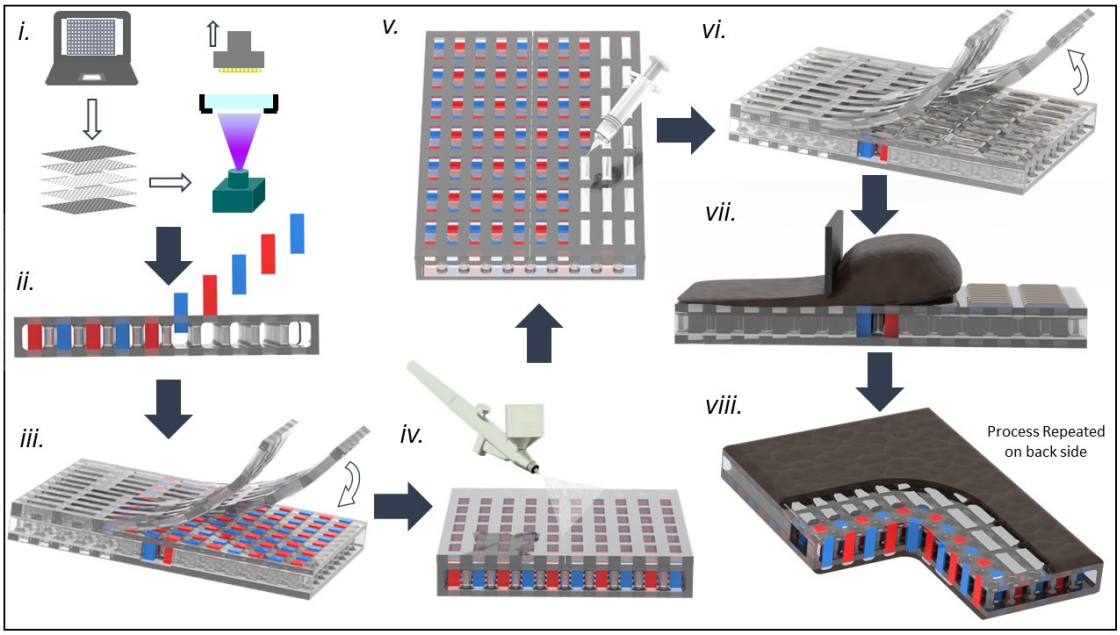

Figure C.1: **i**, The center elastomer layer is printed using a DLP 3D printer. **ii**, Bismuth telluride semiconductors are placed into printed holes in alternating p-n configuration. **iii**, A soft 3D printed stencil is placed over the device leaving semiconductors and interconnects exposed. **iv**, A light coating of EGaIn is air brushed over the stencil to decrease contact resistance between semiconductors. **v**, LM-Ag-SIS ink is formulated and injected into the stencil wells. **vi**, Stencil is removed followed by solvant evaporation to form stable interconnects between the semiconductors. **vii**, LM-epoxy, a liquid metal embedded elastomer thermal interface material, is applied over the device to improve thermal performance and strengthen device. **viii**, The process is then repeated on the back side with leads being attached to the corner semiconductors for interfacing with electronics.

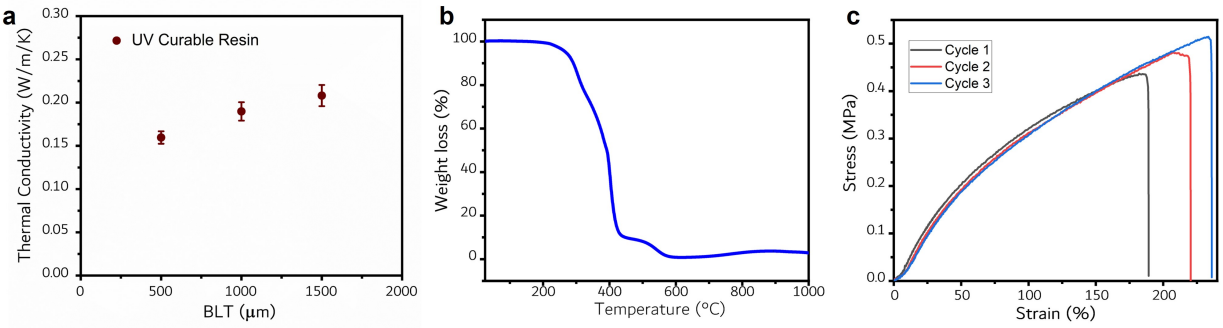

Figure C.2: **a**, Thermal conductivity measurements for center DLP printed layer. **b**, Thermogravimetric data for center DLP printed layer used in TEG fabrication. **c**, Stress-strain curve for center DLP printed layer.

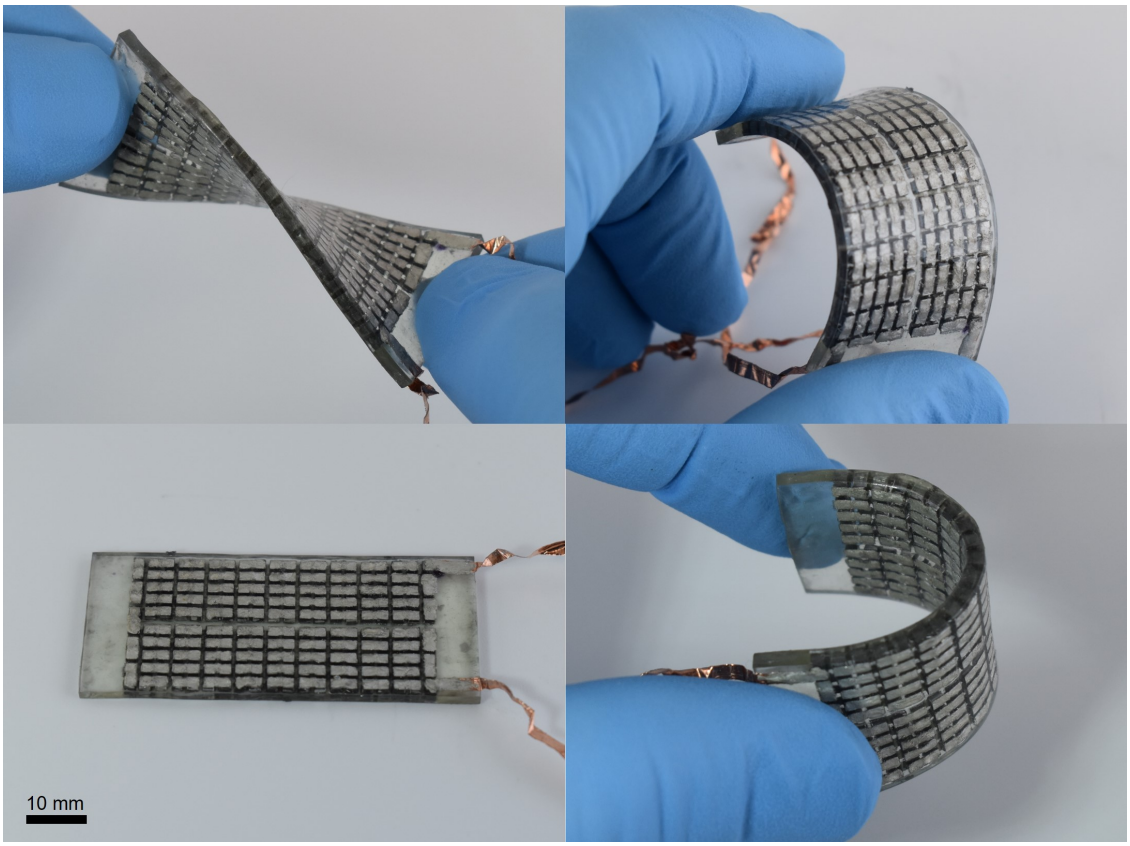

Figure C.3: Additional images of completed Low-Aspect High-Density (LA-HD) Device

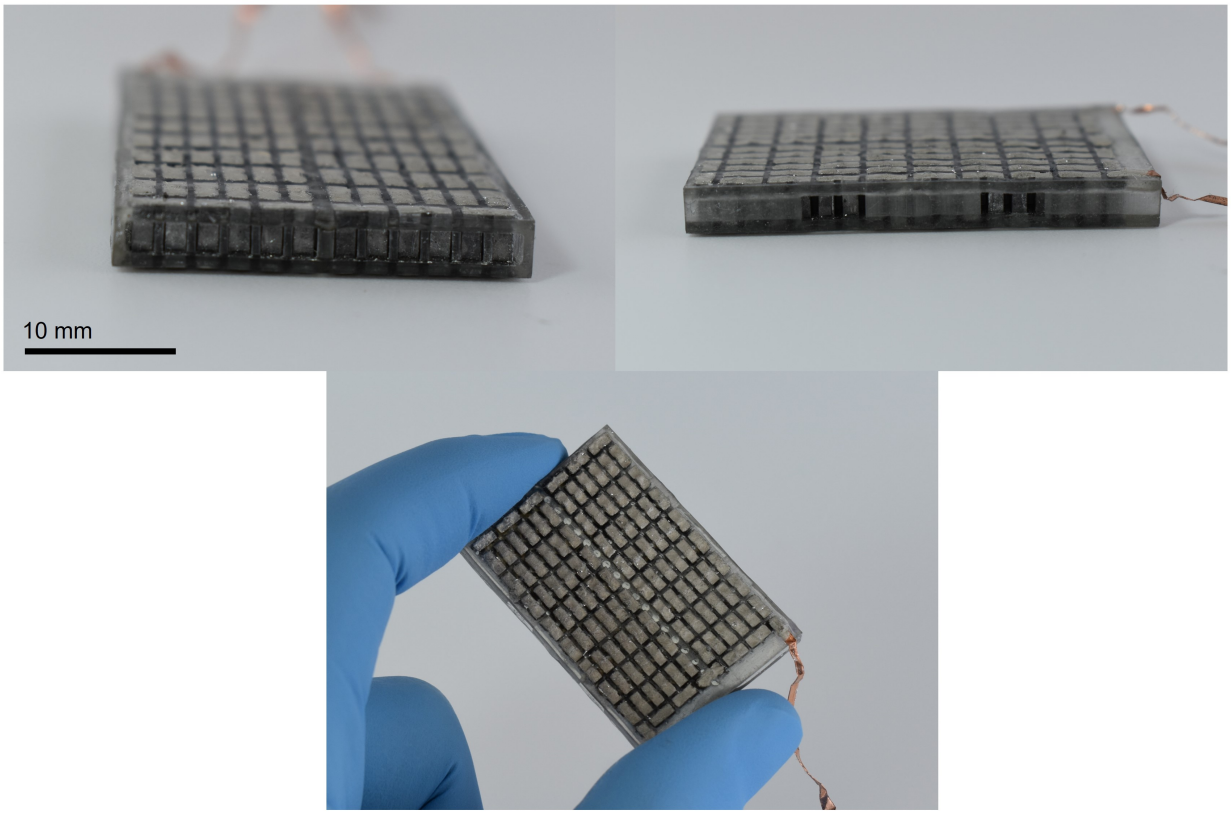

Figure C.4: Additional images of completed High-Aspect High-Density (HA-HD) Device

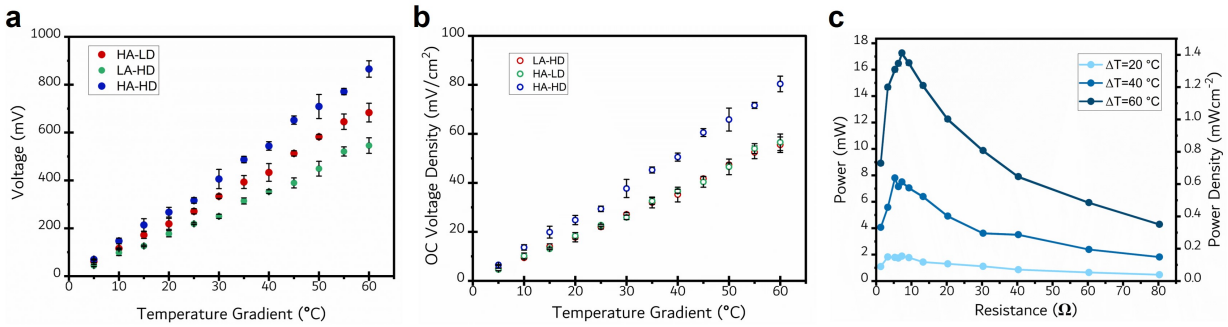

Figure C.5: Seebeck Characterization: **a**, Open-circuit voltage vs temperature and (**b**) voltage density vs temperature for HA-LD, HA-HD, and LA-HD TEG devices. **c**, Power output vs external load resistance for HA-LD + LM-epoxy TEG at ΔT=20, 40, 60 °C.

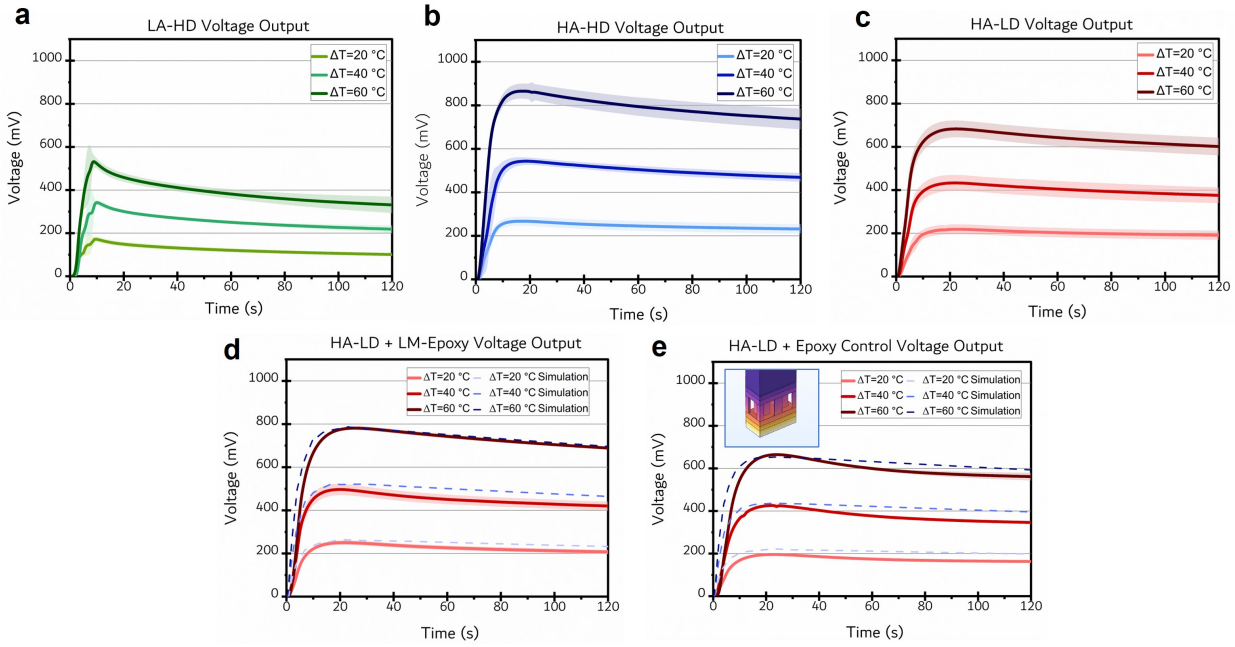

Figure C.6: **a**, LA-HD voltage output vs time for varying temperature differentials. **b**, HA-HD voltage output vs time for varying temperature differentials. **c**, HA-LD voltage output vs time for varying temperature differentials. **d**, HA-LD + LM-epoxy voltage output vs time for varying temperature differentials along with FEA comparison. **e**, HA-LD + Epoxy Control voltage output vs time for varying temperature differentials along with FEA comparison. Inset: Image of representative volume elements used for d and e.

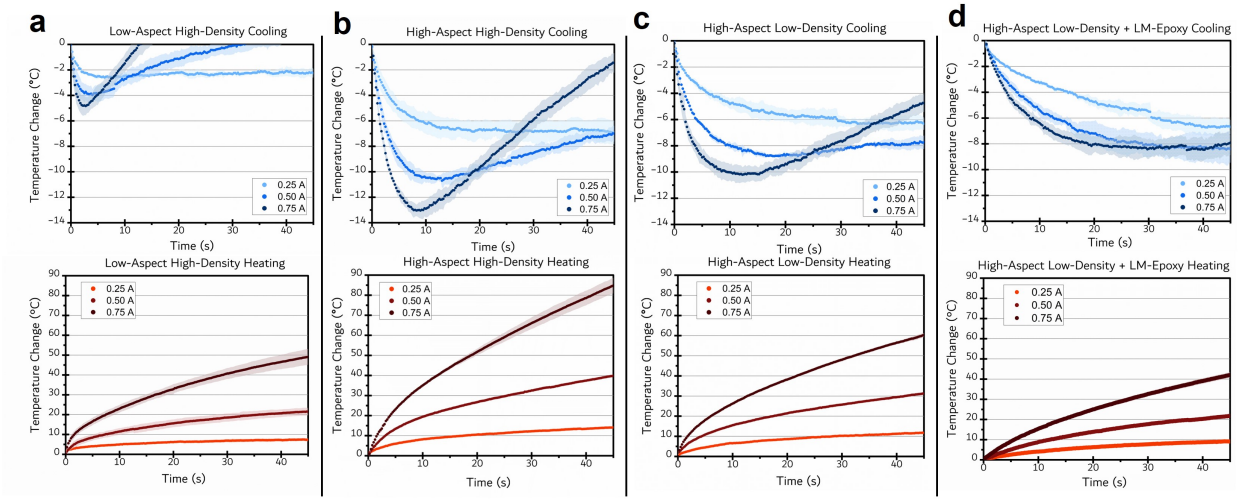

Figure C.7: Peltier Characterization: **a** Peltier cooling and heating performance of low-aspect high-density (LA-HD), **b** high-aspect high-density (HA-HD), **c** high-aspect low-density (HA-LD) TEG and **d**, high-aspect low-density (HA-LD) + LM-epoxy TED at 0.25, 0.50 and 0.75 A.

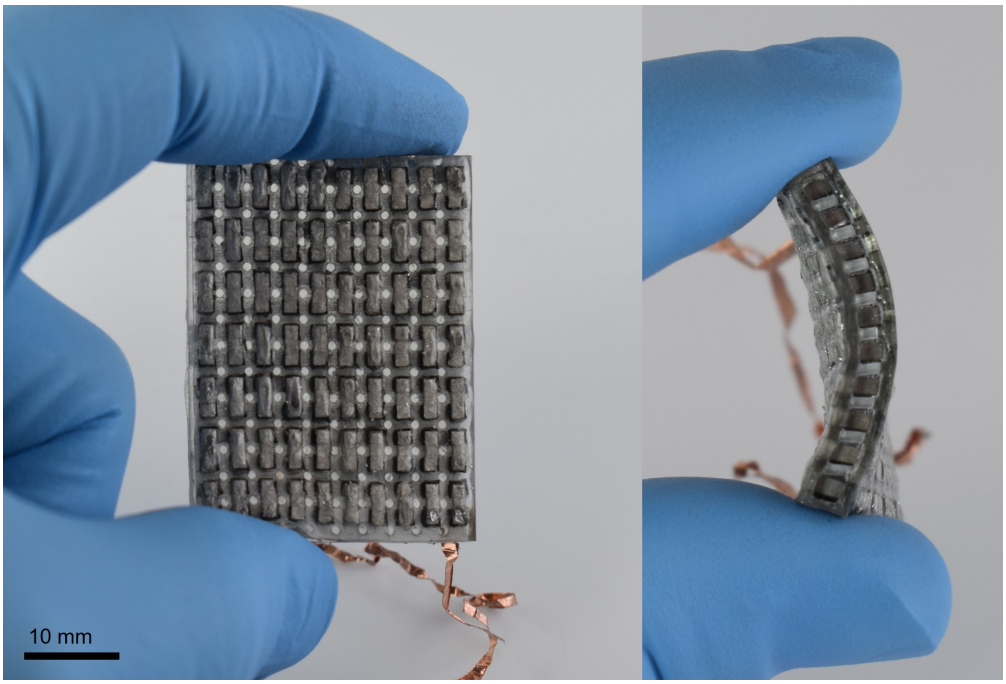

Figure C.8: Additional images of completed High-Aspect Low-Density (HA-LD) Device

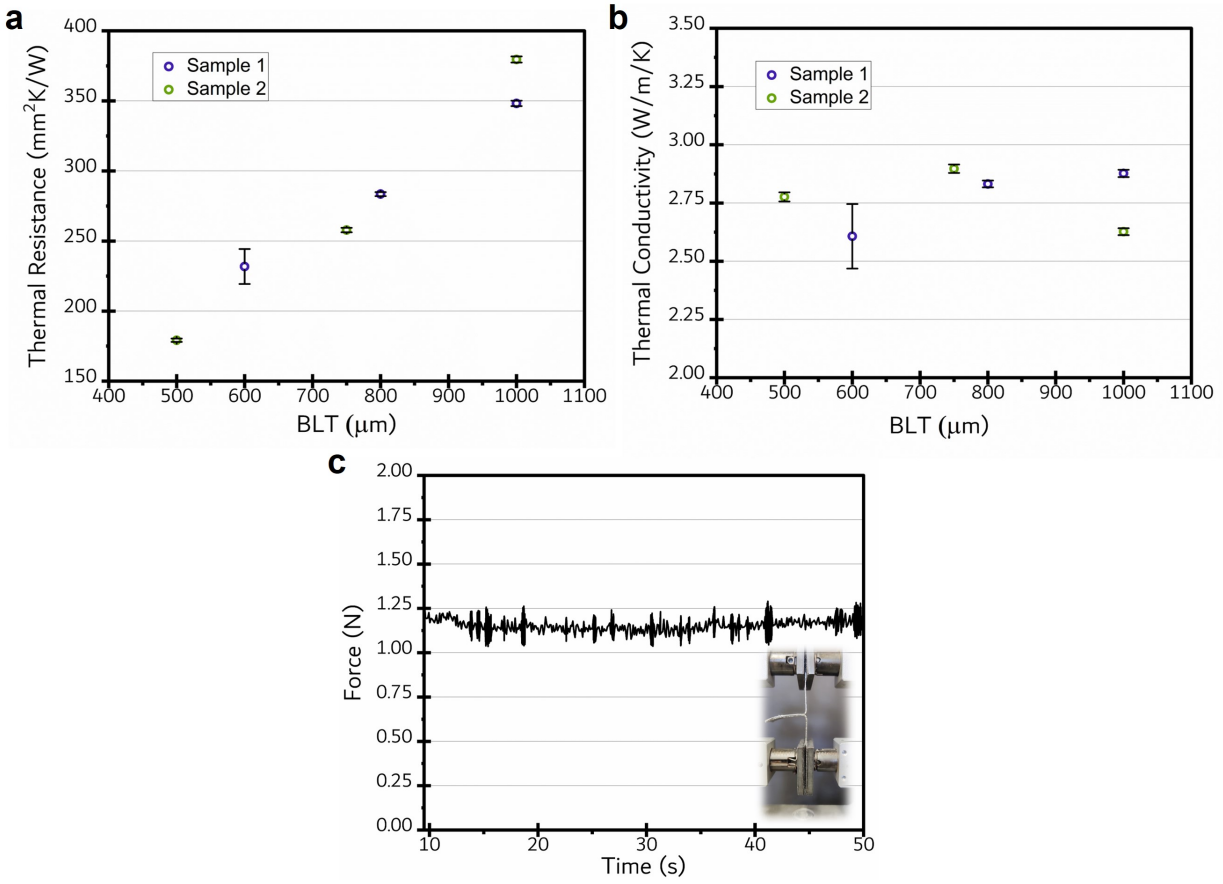

Figure C.9: **(a)** Thermal resistance vs BLT (bond length thickness) and **(b)** Thermal conductivity vs BLT for uncured LM-epoxy epoxy at 65 vol% loading and **(c)** Peel test for 0.5 mm thick LM-epoxy composite and 0.5 mm thick DLP printed elastomer, measuring force output for 180 ° peel test

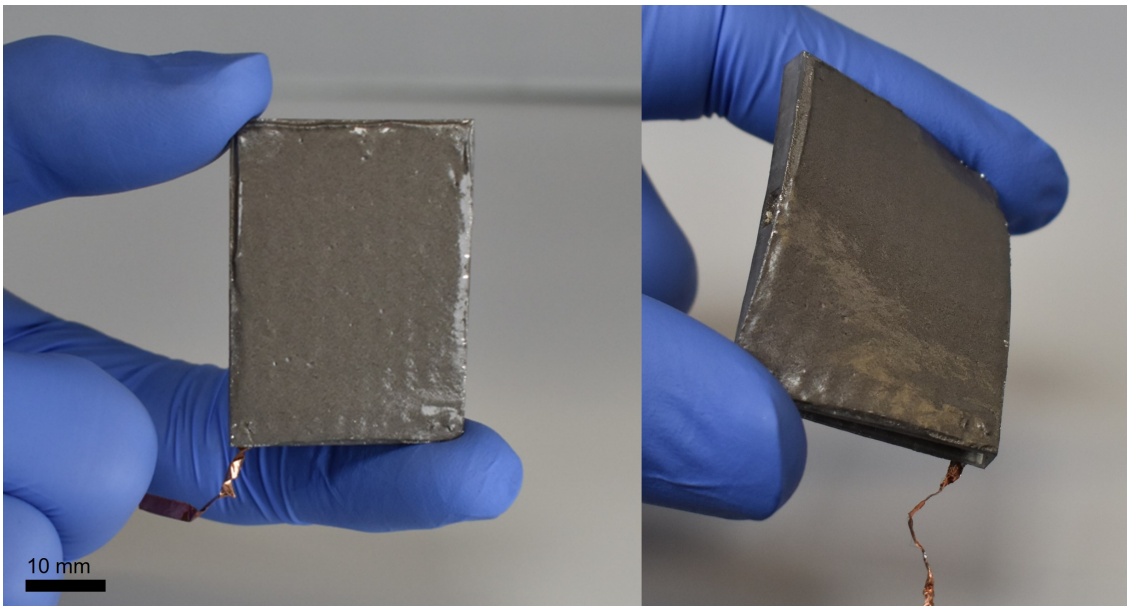

Figure C.10: Additional image of completed High-Aspect Low-Density + LM-epoxy Device

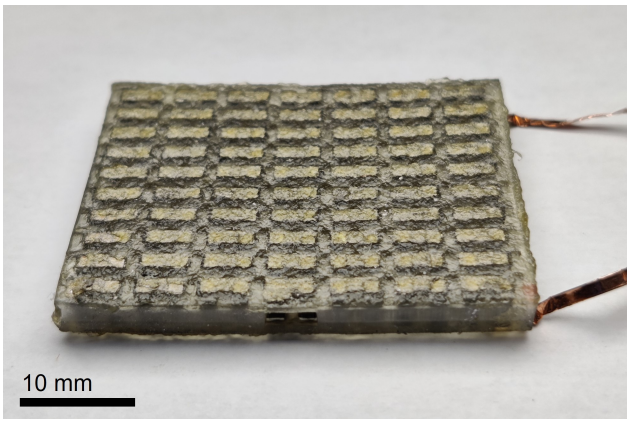

Figure C.11: Image of completed High-Aspect Low-Density + Epoxy as control device

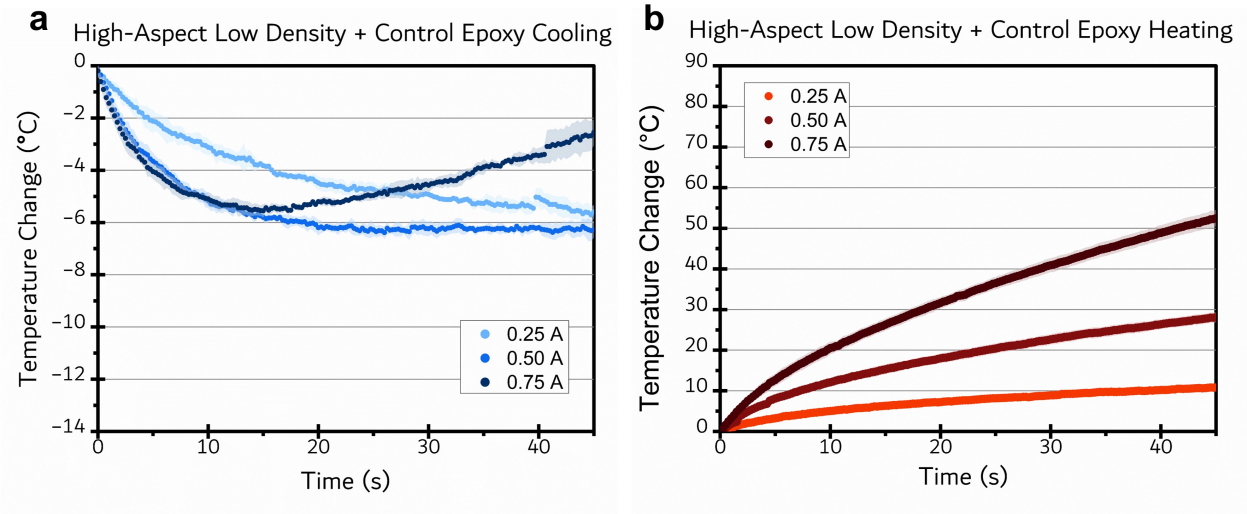

Figure C.12: **(a)** Peltier cooling and **(b)** heating performance of HA-LD+control epoxy TED at 0.25, 0.50, and 0.75 A.

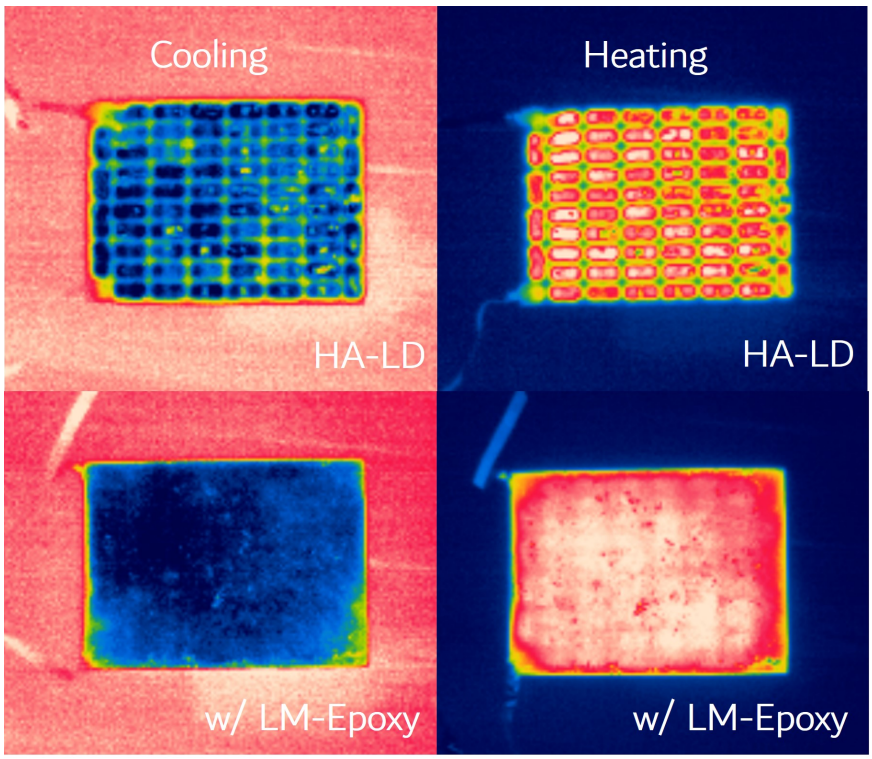

Figure C.13: Comparison of heating and cooling profiles with and without LM-epoxy layer.

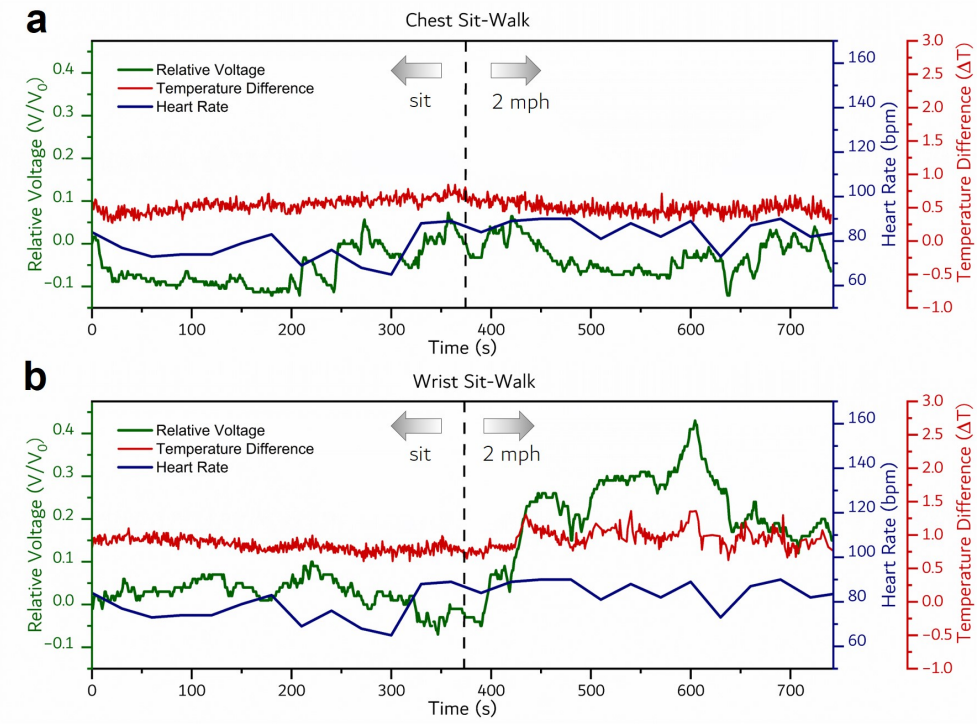

Figure C.14: **a-b**, Results of chest and wrist worn TEG trials for sit-walk tests measuring relative voltage, temperature difference, and heart rate.

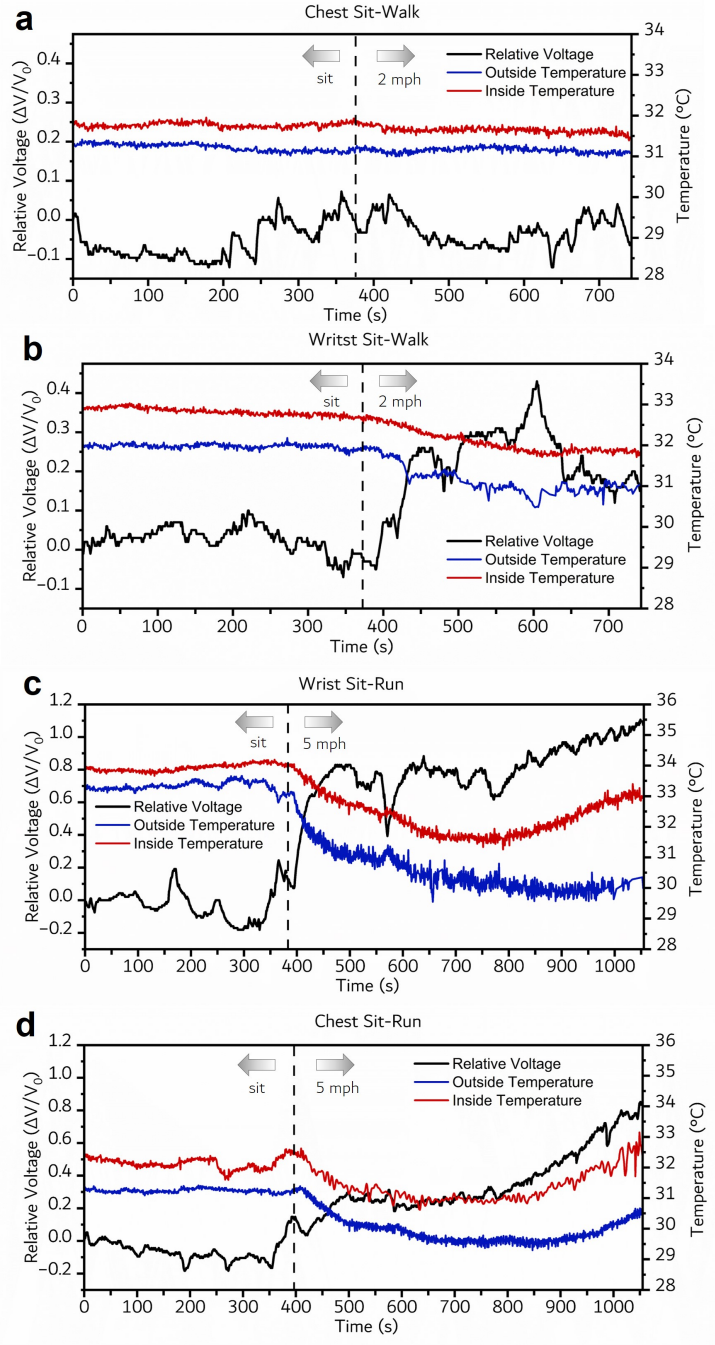

Figure C.15: **a-d**, Results of chest and wrist worn TEG trials for sit-walk and sit-run tests. Relative voltage change and outside and inside TEG temperature are recorded, highlighting the influence of physical activity in TEG performance.

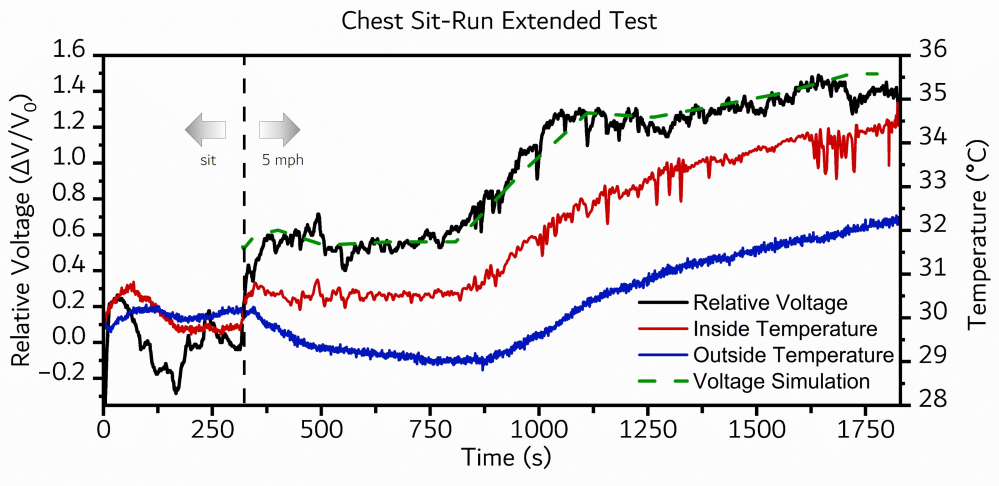

Figure C.16: Results of chest TEG trial for sit-run tests. Relative voltage change and inside and outside temperatures of the TEG are given along with an FEA simulation comparison.

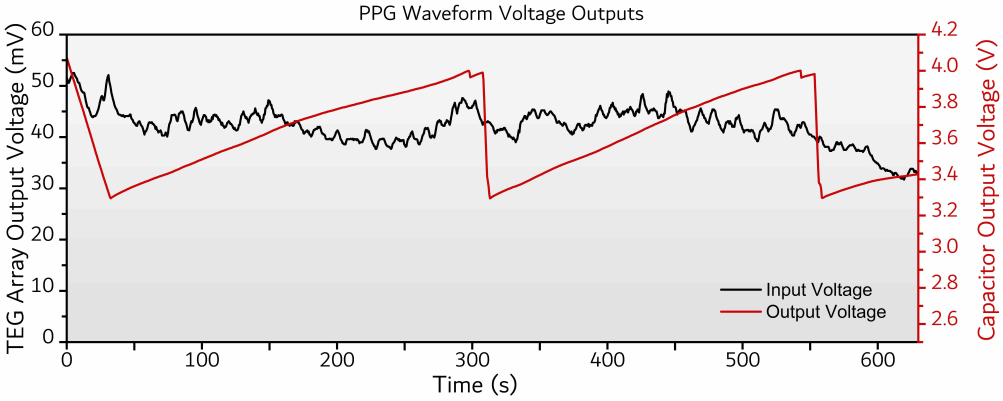

Figure C.17: Boost converter input voltage and capacitor output voltage corresponding to the two PPG waveform cycles in Figure 4.5d.

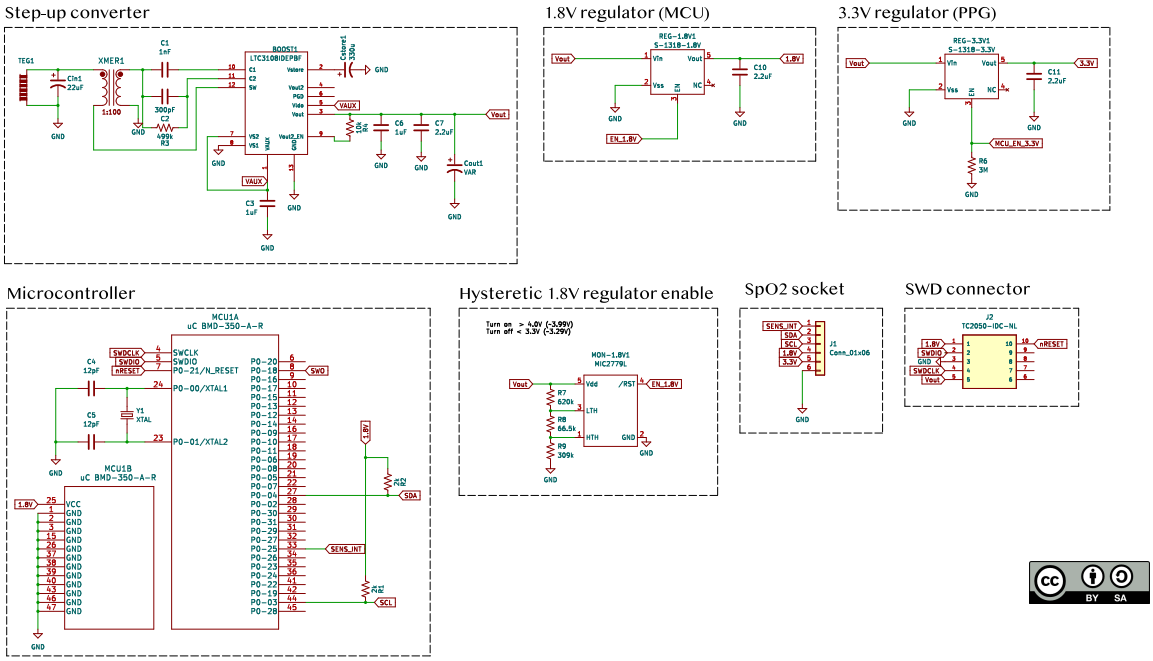

Figure C.18: TEGsense schematic broken into the functional parts.

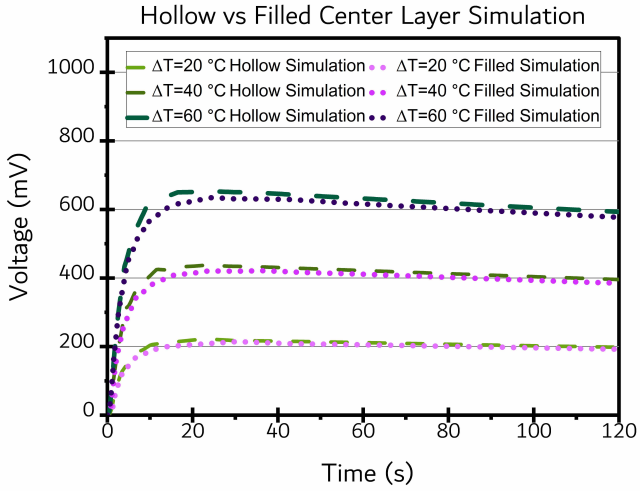

Figure C.19: High-aspect ratio TEGs are fabricated with a DLP 3D printed hollow internal layer supported with pillars to decrease stiffness of the overall device. This figure compares FEA simulations for a fully filled in vs hollow center layer to compare heat transfer and TEG performance. The hollow internal layer has a negligible impact on thermal and energy harvesting performance.

Table C.1: Comparison of electrical and mechanical characteristics of various deformable TEG publications (Note: P.D. stands for Power Density and LMEE stands for liquid metal embedded elastomer).

V_{oc} (mV)	P. D. $(\mu W/cm^2)$	Mechanical Performance (mode, strain, $\frac{\Delta R}{R_0}$, cycle #)	Peak Peltier Cooling (ΔT)	Fill Density	TIM $(Wm^{-1}K^{-1})$	Ref.
866 @ 60 °C	3318 @ 60 °C	buckling, 5.9mm, 0.05, 1000	-13.0 °C @ 0.75 A	40%	LMEE, 2.9	This work
290 @ 60 °C	86.6 @ 60 °C	uniaxial, 30% 0.21, 1000	N/A	10.1%	LMEE, 1.6	[20]
107.1 @ 60 °C	236.7 @ 60 °C	buckling, 6.5 mm 0.05, 1000	-6.5 °C @ 1.75	28%	UV curable elastomer, 0.18	[151]
2120 @ 40 °C	419 @ 40 °C	buckling, 15mm, 0.13, 1000	N/A	26%	Ag–Ni particle-PDMS, 1.1	[165]
N/A	25.1 @ 22°C	buckling, 30 mm, 0.017, 1000	-7.3 °C @ 0.14 A	5.8%	Ecoflex and AlN particles, 0.77	[93]
392 @ 60 °C	650 @ 60 °C	uniaxial, 30%, 0.014, 15,000	N/A	14.3%	LMEE, 1.1	[156]
7.4 @ 8.5 °C	8.3 @ 8.5 °C	buckling, 22.5 mm, N/A, N/A	-5.4 °C @ 1.33 A	50.4%	PDMS and Hydrogel	[218]
22 @ 20 °C	19.8 @ 20 °C	uniaxial, 20%, -0.89, 1000	N/A	62%	Ecoflex, 0.16	[102]
25 @ 10 °C	23 @ 10 °C	buckling, 3.5 mm, 0.07, 100	N/A	20%	LMEE, 0.84	[154]
971 @ 50 °C	3420 @ 50 °C	uniaxial, 30%, 0.30, 18,000	-19 °C 2 A	50%	Silver embedded Ecoflex, 0.4	[137]
N/A	2.5 @ 30 °C	buckling, 5 mm, 0.01, 1000	N/A	5.8%	PDMS, 0.15	[103]
630 @ 60 °C	8 @ 60 °C	buckling, 3.5 mm, 0.00, 1000	N/A	20%	polyimine, 0.12	[219]
86 @ 25 °C	44 @ 25 °C	N/A	N/A	38%	water absorbent bead armband	[95]
370 @ 20 °C	2700 @ 20 °C	buckling, 30 mm, 0.01, 10,000	N/A	28%	PDMS, 0.15	[94]
600 @ 20 °C	356 @ 20 °C	buckling, 10 mm, 0.0, 1000	N/A	22%	polyimine, 0.11	[220]
8.8 @ 1.4 °C	5.6 @ 1.4 °C	buckling, 11.3 mm, N/A, N/A	-4.4 °C at 1.33 A	22%	Gel heat sink	[221]
123.3 @ 18.5 °C	160 @ 18.5 °C	uniaxial, 40%, <0.05, 100	N/A	23%	Ecoflex, 0.16	[150]
236 @ 50 °C	1309 @ 50 °C	buckling, 6.5 mm, 0.01, 7400	N/A	16%	Au coated Cu film	[152]

Printing parameter	Center layer
Slice thickness (mm)	0.1
Exposure time (s)	0.5
Burn-in layers	1
Burn-in exposure time (s)	1.050
Light intensity (mW/cm^2)	27.84
Heater temperature (°C)	40
Separation velocity (mm/s)	1.000
Separation distance (mm)	10.000
Approach velocity (mm/s)	2.000
Slides per layer	1
Slide velocity (mm/s)	10.000
Burn-in wait time (after exposure)	5.000
Burn-in wait time (after separation)	5.000
Burn-in wait time (after approach)	3.000
Burn-in wait time (after slide)	5.000
Normal wait time (after exposure)	5.000
Normal wait time (after separation)	5.000
Normal wait time (after approach)	5.000
Normal wait time (after slide)	5.000

Table C.2: Table of Asiga (PicoHD@27) printing parameters for 3D printed DLP center layer.

Configuration	Length (mm)	width (mm)	Height (mm)	Semi-conductor #	Semi-conductor density (%)	Area (mm^2)
HA-HD	38.9	27.7	4	216	39.3	1078
LA-HD	42.7	22.6	1.6	200	40.6	965
HA-LD	41	30	4	140	22.3	1230

Table C.3: Table highlighting key metrics of various TEG configurations.

Parameter	Value	Unit
Bi_2Te_3 thermal conductivity	3	W/mK
Bi_2Te_3 electrical conductivity	87000	S/m
Bi_2Te_3 Seebeck coefficient	$\pm$160	μV/K
Thubber thermal conductivity	2.9	W/mK
Aluminium thermal conductivity	236.2	W/mK
Interconnect electrical conductivity	6.38 x 10^5	S/m
Interconnect thermal conductivity	15	W/mK
Epoxy thermal conductivity	0.18	W/mK
Air thermal conductivity	0.0242	W/mK
Heat transfer coefficient	10	W/m^2K
Air velocity (while running)	0.3	m/s
Room temperature	23	°C

Table C.4: Parameters used in COMSOL simulation

Appendix D

D.1 Supplementary Figures

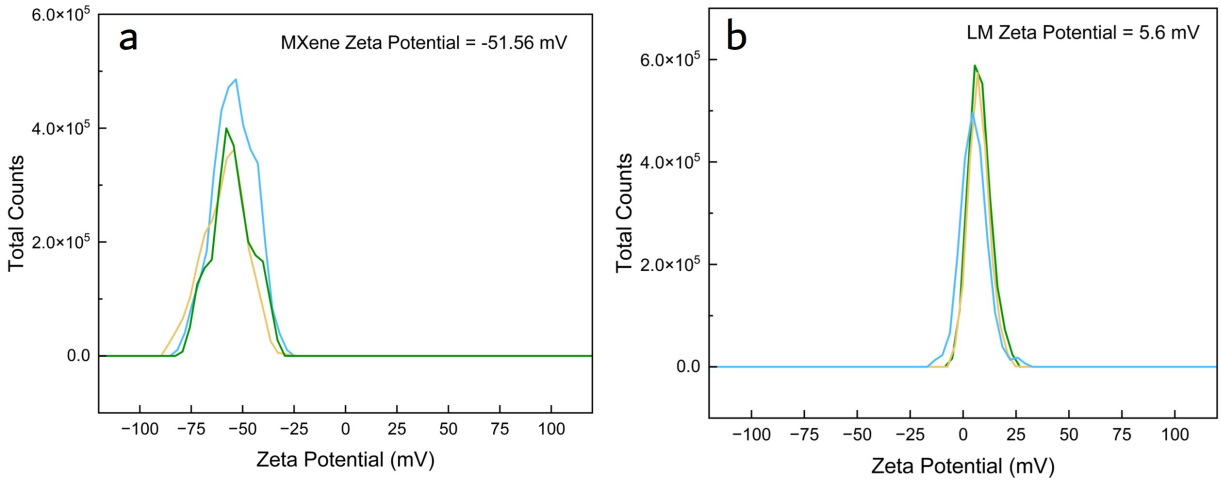

Figure D.1: **a**, Three cycles of zeta potential measurements for MXenes synthesized in a 80:20 DMSO:DI water solution and diluted in DI water, indicating strong negative charge and colloidal stability. **b**, Three cycles of zeta potential measurements for LM sonicated in 80:20 DMSO:DI Water and diluted for testing in DI water indicating weak surface charges.

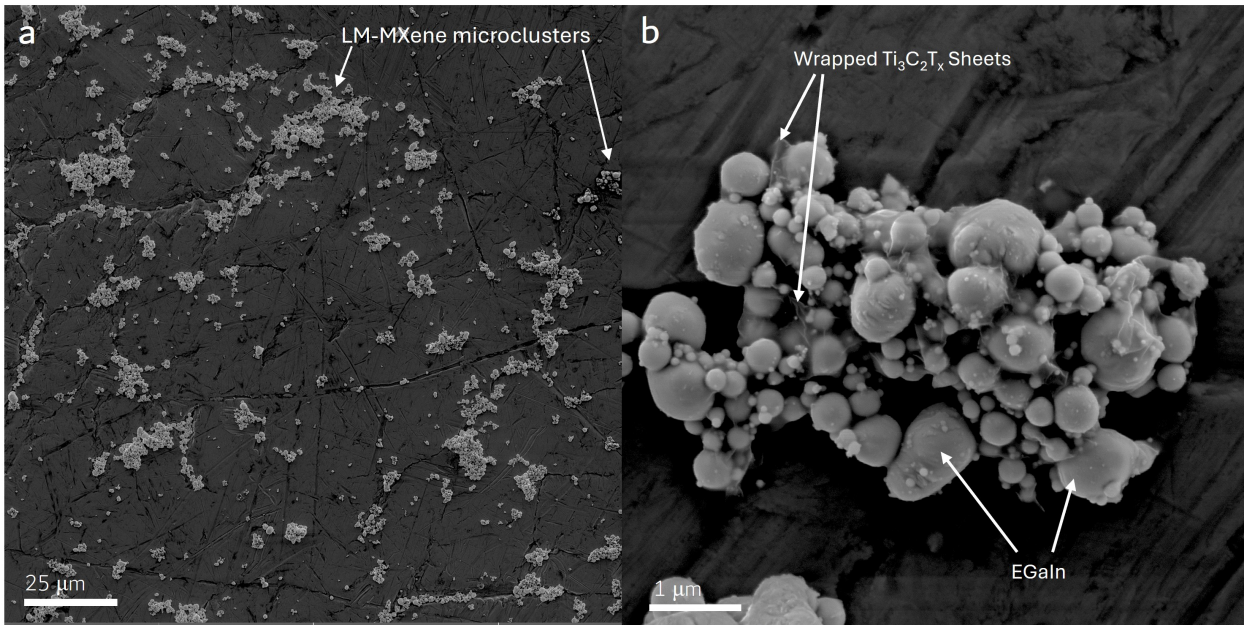

Figure D.2: **a**, SEM Image of MXene-LM microclusters on an Al stub after sonication of MXenes and LM in a DMSO:DI water solution. After sonication, the solution was then diluted and planetary mixed before drop-casting onto the Al stub. B) Image of one individual microcluster highlighting the MXene sheets wrapping and binding the LM droplets together.

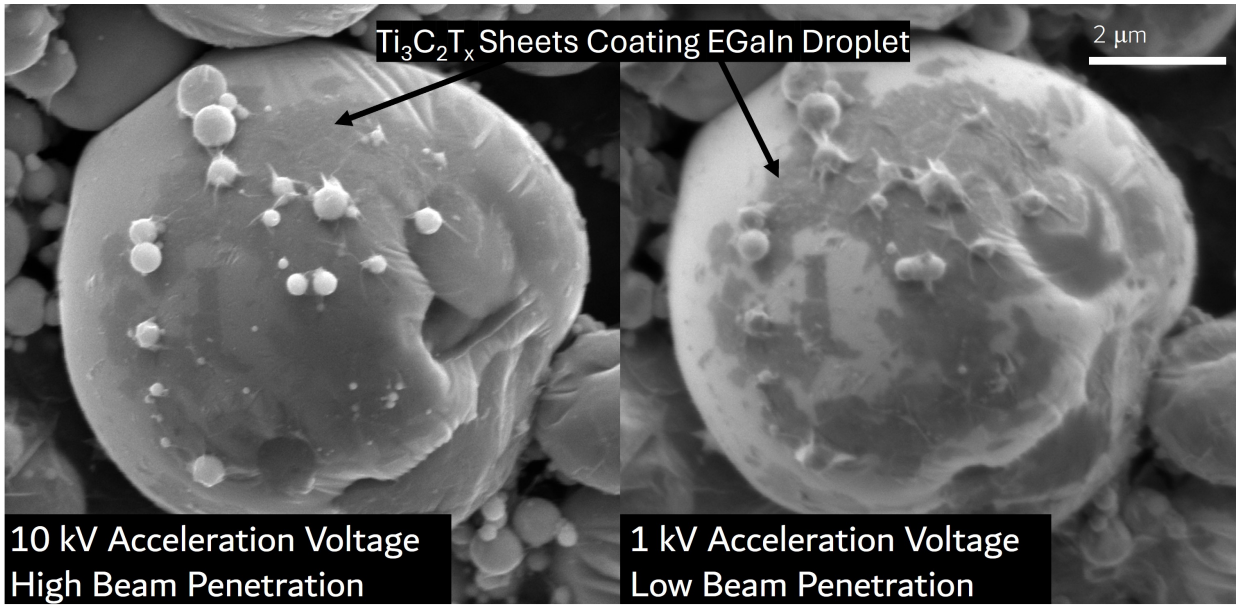

Figure D.3: Image of a large liquid metal droplet and smaller liquid metal droplets on the surface coated with MXene sheets after probe sonication. This figure gives insight into the influence of accelerating voltage on beam penetration and the quality of 2D MXene sheets.

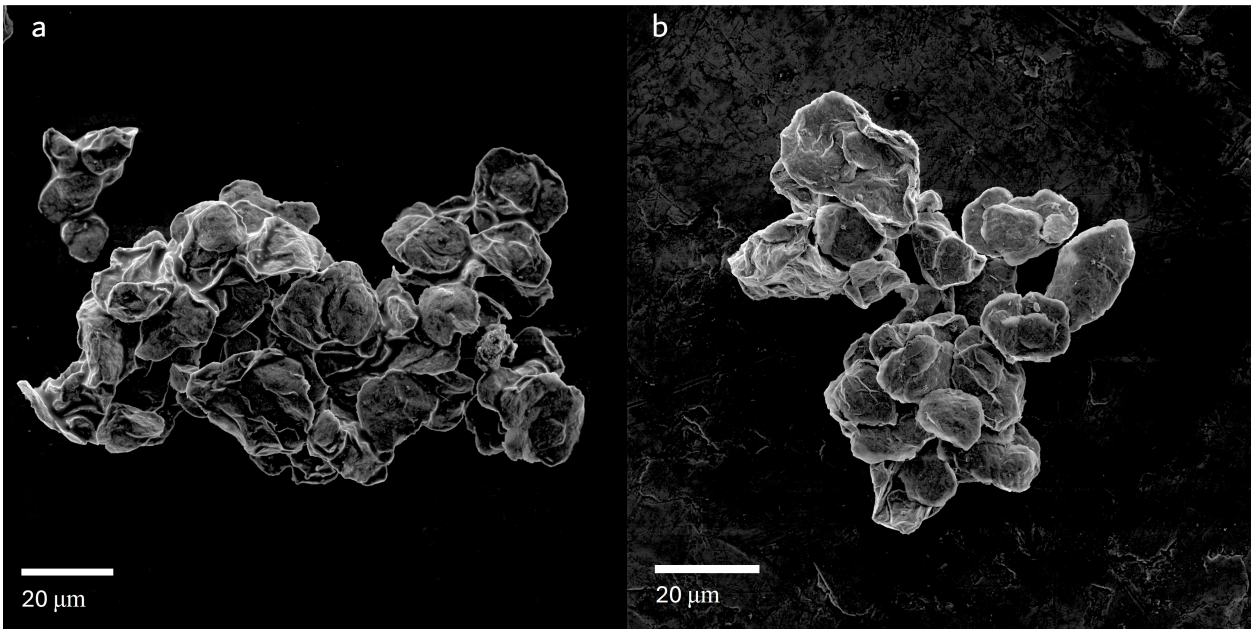

Figure D.4: **a-b**, Images of crumpled MXene aggregates recovered from silicone matrix material. Images are taken from the a 5 vol % MXene control sample suspended in silicone oil.

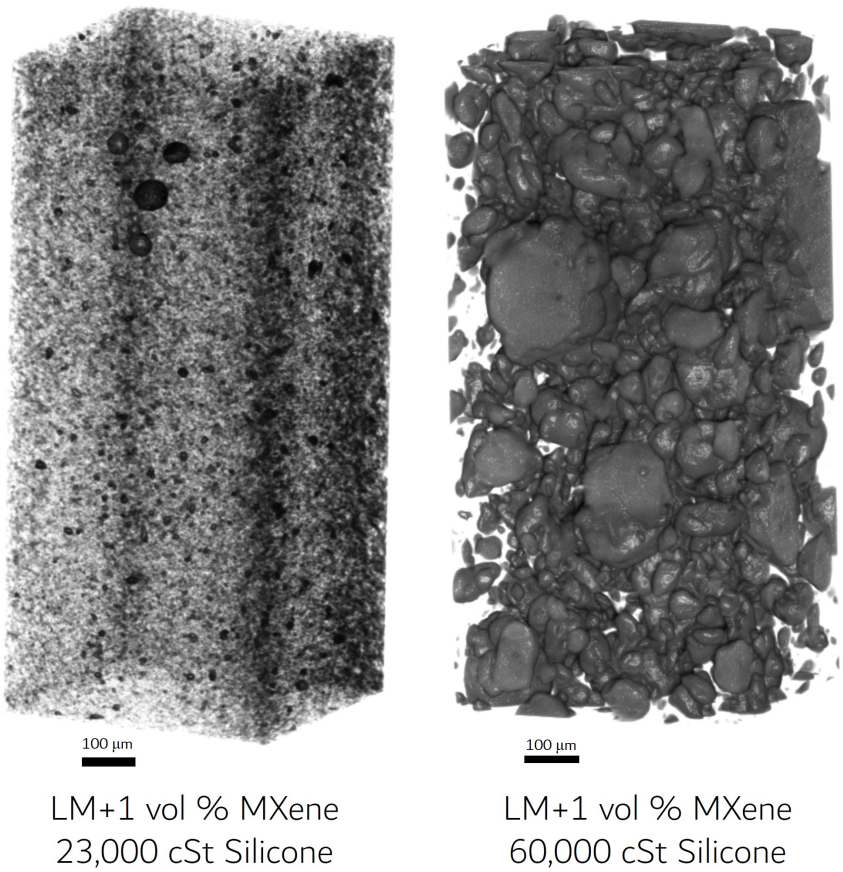

Figure D.5: Intensity calibrated MicroCT reconstructions of LM+1 vol % MXene samples prepared in 23,000 cSt silicone and 60,000 cSt silicone indicating that the friction caused by the high viscosity is causing a coalescence of larger aggregates.

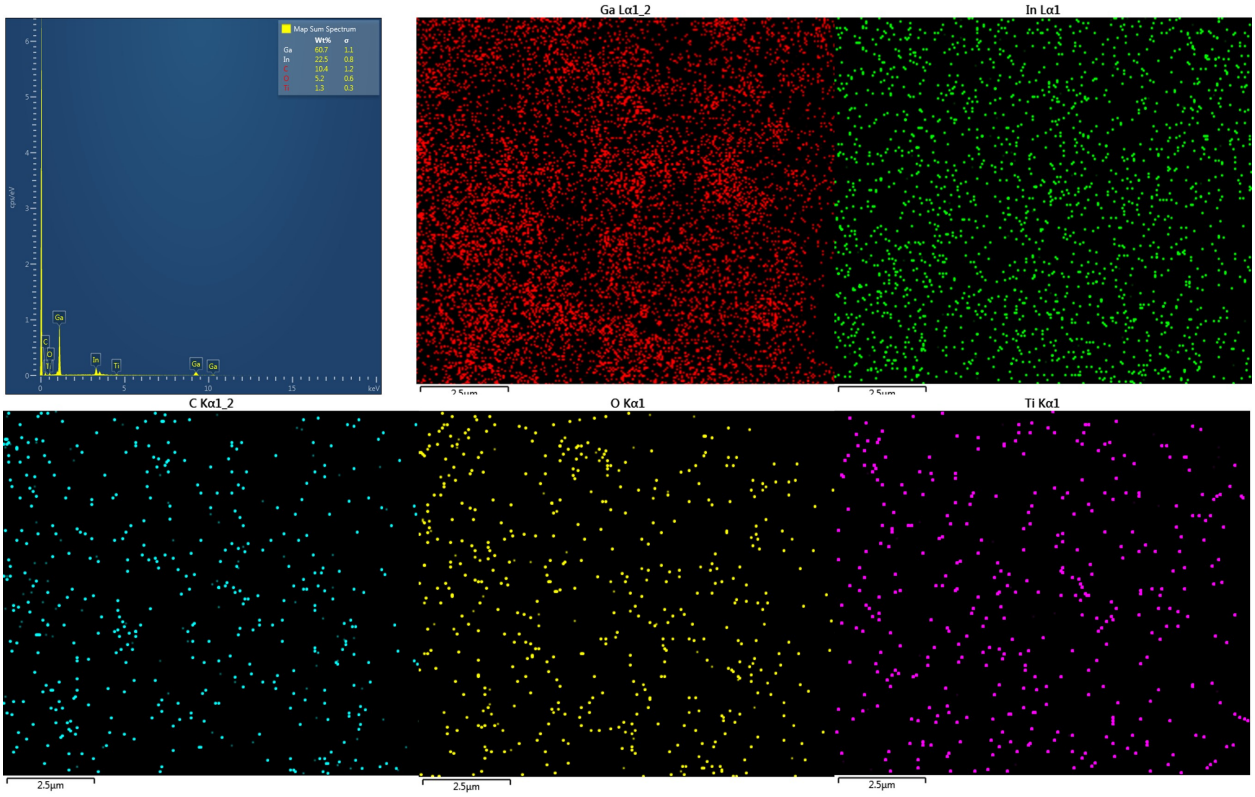

Figure D.6: **a**, EDS map sum spectrum corresponding to Figure 5.2e along with individual elemental maps.

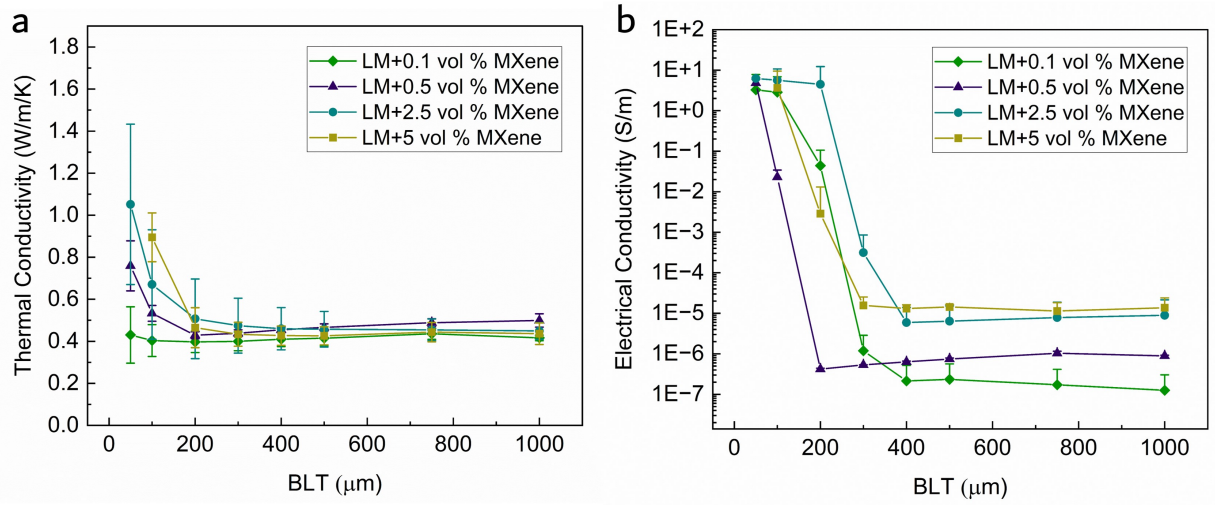

Figure D.7: **a**, Graph of thermal conductivity vs BLT for various MXene vol %. **b**, Graph of electrical conductivity vs BLT for various MXene vol %.

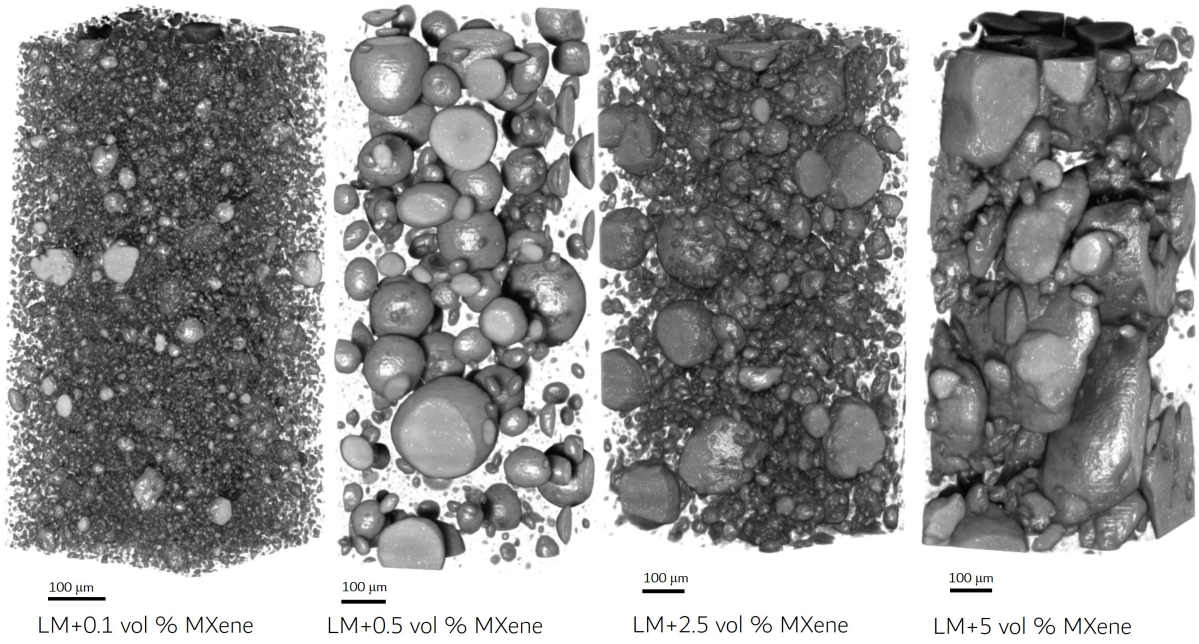

Figure D.8: Intensity calibrated microCT reconstructions of MXene-LM composites for additional volume fractions. Aggregation is shown with as little as 0.1 vol % MXenes over the LM control.

Bibliography

[1] J. Wang, S. Li, F. Yi, Y. Zi, J. Lin, X. Wang, Y. Xu, and Z. L. Wang, "Sustainably powering wearable electronics solely by biomechanical energy," *Nature communications*, vol. 7, no. 1, pp. 1–8, 2016.

[2] S. Gong and W. Cheng, "Toward soft skin-like wearable and implantable energy devices," *Advanced Energy Materials*, vol. 7, no. 23, p. 1700648, 2017.

[3] A. Nozariasbmarz, H. Collins, K. Dsouza, M. H. Polash, M. Hosseini, M. Hyland, J. Liu, A. Malhotra, F. M. Ortiz, F. Mohaddes *et al.*, "Review of wearable thermoelectric energy harvesting: From body temperature to electronic systems," *Applied Energy*, vol. 258, p. 114069, 2020.

[4] N. Jaziri, A. Boughamoura, J. Müller, B. Mezghani, F. Tounsi, and M. Ismail, "A comprehensive review of thermoelectric generators: Technologies and common applications," *Energy Reports*, vol. 6, pp. 264–287, 2020.

[5] D. Champier, "Thermoelectric generators: A review of applications," *Energy Conversion and Management*, vol. 140, pp. 167–181, 2017.

[6] K. Yazawa, J.-H. Bahk, and A. Shakouri, *Thermoelectric energy conversion devices and systems*. World Scientific, 2021, vol. 7.

[7] R. Riemer and A. Shapiro, "Biomechanical energy harvesting from human motion: theory, state of the art, design guidelines, and future directions," *Journal of neuroengineering and rehabilitation*, vol. 8, no. 1, pp. 1–13, 2011.

[8] L. Zhou, D. Liu, J. Wang, and Z. L. Wang, "Triboelectric nanogenerators: fundamental physics and potential applications," *Friction*, vol. 8, no. 3, pp. 481–506, 2020.

[9] H. Zou, Y. Zhang, L. Guo, P. Wang, X. He, G. Dai, H. Zheng, C. Chen, A. C. Wang, C. Xu *et al.*, "Quantifying the triboelectric series," *Nature communications*, vol. 10, no. 1, pp. 1–9, 2019.

[10] R. D. Kornbluh, R. Pelrine, H. Prahlad, A. Wong-Foy, B. McCoy, S. Kim, J. Eckerle, and T. Low, "Dielectric elastomers: Stretching the capabilities of energy harvesting," *MRS bulletin*, vol. 37, no. 3, pp. 246–253, 2012.

[11] F. Carpi, D. De Rossi, R. Kornbluh, R. E. Pelrine, and P. Sommer-Larsen, *Dielectric elastomers as electromechanical transducers: Fundamentals, materials, devices, models and applications of an emerging electroactive polymer technology*. Elsevier, 2011.

[12] K. S. Ramadan, D. Sameoto, and S. Evoy, "A review of piezoelectric polymers as functional materials for electromechanical transducers," *Smart Materials and Structures*, vol. 23, no. 3, p. 033001, 2014.

[13] W.-S. Jung, M.-J. Lee, M.-G. Kang, H. G. Moon, S.-J. Yoon, S.-H. Baek, and C.-Y. Kang, "Powerful curved piezoelectric generator for wearable applications," *Nano Energy*, vol. 13, pp. 174–181, 2015.

[14] S. J. Rupitsch, "Piezoelectric sensors and actuators," *Simulation of Piezoelectric Sensor and Actuator Devices. In: Piezoelectric Sensors and Actuators. Topics in Mining, Metallurgy and Materials Engineering*, pp. 83–126, 2019.

[15] Y. Sun, J. Chen, X. Li, Y. Lu, S. Zhang, and Z. Cheng, "Flexible piezoelectric energy harvester/sensor with high voltage output over wide temperature range," *Nano Energy*, vol. 61, pp. 337–345, 2019.

[16] D. Wang, G. Yuan, G. Hao, and Y. Wang, "All-inorganic flexible piezoelectric energy harvester enabled by two-dimensional mica," *Nano Energy*, vol. 43, pp. 351–358, 2018.

[17] C. Baek, J. H. Yun, J. E. Wang, C. K. Jeong, K. J. Lee, K.-I. Park, and D. K. Kim, "A flexible energy harvester based on a lead-free and piezoelectric bctz nanoparticle–polymer composite," *Nanoscale*, vol. 8, no. 40, pp. 17 632–17 638, 2016.

[18] H. J. Goldsmid, "Bismuth telluride and its alloys as materials for thermoelectric generation," *Materials*, vol. 7, no. 4, pp. 2577–2592, 2014.

[19] D. Enescu and E. O. Virjoghe, "A review on thermoelectric cooling parameters and performance," *Renewable and Sustainable Energy Reviews*, vol. 38, pp. 903–916, 2014.

[20] M. Zadan, M. H. Malakooti, and C. Majidi, "Soft and stretchable thermoelectric generators enabled by liquid metal elastomer composites," *ACS applied materials & interfaces*, vol. 12, no. 15, pp. 17 921–17 928, 2020.

[21] S. Nayak, Y. Li, W. Tay, E. Zamburg, D. Singh, C. Lee, S. J. A. Koh, P. Chia, and A. V.-Y. Thean, "Liquid-metal-elastomer foam for moldable multi-functional triboelectric energy harvesting and force sensing," *Nano Energy*, vol. 64, p. 103912, 2019.

[22] Y. Sargolzaeiaval, V. P. Ramesh, T. V. Neumann, V. Misra, D. Vashaee, M. D. Dickey, and M. C. Öztürk, "Flexible thermoelectric generators for body heat harvesting–enhanced device performance using high thermal conductivity elastomer encapsulation on liquid metal interconnects," *Applied Energy*, vol. 262, p. 114370, 2020.

[23] C. Pan, D. Liu, M. J. Ford, and C. Majidi, "Ultrastretchable, wearable triboelectric nanogenerator based on sedimented liquid metal elastomer composite," *Advanced Materials Technologies*, vol. 5, no. 11, p. 2000754, 2020.

[24] M. D. Bartlett, N. Kazem, M. J. Powell-Palm, X. Huang, W. Sun, J. A. Malen, and C. Majidi, "High thermal conductivity in soft elastomers with elongated liquid metal inclusions," *Proceedings of the National Academy of Sciences*, vol. 114, no. 9, pp. 2143–2148, 2017.

[25] Y.-L. Park, B.-R. Chen, and R. J. Wood, "Design and fabrication of soft artificial skin using embedded microchannels and liquid conductors," *IEEE Sensors journal*, vol. 12, no. 8, pp. 2711–2718, 2012.

[26] M. D. Dickey, "Emerging applications of liquid metals featuring surface oxides," *ACS applied materials & interfaces*, vol. 6, no. 21, pp. 18 369–18 379, 2014.

[27] J. Yang, W. Cheng, and K. Kalantar-Zadeh, "Electronic skins based on liquid metals," *Proceedings of the IEEE*, vol. 107, no. 10, pp. 2168–2184, 2019.

[28] M. H. Malakooti, N. Kazem, J. Yan, C. Pan, E. J. Markvicka, K. Matyjaszewski, and C. Majidi, "Liquid metal supercooling for low-temperature thermoelectric wearables," *Advanced functional materials*, vol. 29, no. 45, p. 1906098, 2019.

[29] C. Pan, E. J. Markvicka, M. H. Malakooti, J. Yan, L. Hu, K. Matyjaszewski, and C. Majidi, "A liquid-metal–elastomer nanocomposite for stretchable dielectric materials," *Advanced Materials*, vol. 31, no. 23, p. 1900663, 2019.

[30] X. Wang and J. Liu, "Recent advancements in liquid metal flexible printed electronics: Properties, technologies, and applications," *Micromachines*, vol. 7, no. 12, p. 206, 2016.

[31] K. Khoshmanesh, S.-Y. Tang, J. Y. Zhu, S. Schaefer, A. Mitchell, K. Kalantar-Zadeh, and M. D. Dickey, "Liquid metal enabled microfluidics," *Lab on a Chip*, vol. 17, no. 6, pp. 974–993, 2017.

[32] Y. Plevachuk, V. Sklyarchuk, S. Eckert, G. Gerbeth, and R. Novakovic, "Thermophysical properties of the liquid ga–in–sn eutectic alloy," *Journal of Chemical & Engineering Data*, vol. 59, no. 3, pp. 757–763, 2014.

[33] D. Zrnic and D. Swatik, "On the resistivity and surface tension of the eutectic alloy of gallium and indium," *Journal of the less common metals*, vol. 18, no. 1, pp. 67–68, 1969.

[34] J.-H. Kim, S. Kim, J.-H. So, K. Kim, and H.-J. Koo, "Cytotoxicity of gallium–indium liquid metal in an aqueous environment," *ACS applied materials & interfaces*, vol. 10, no. 20, pp. 17 448–17 454, 2018.

[35] R. C. Chiechi, E. A. Weiss, M. D. Dickey, and G. M. Whitesides, "Eutectic gallium–indium (egain): a moldable liquid metal for electrical characterization of self-assembled monolayers," *Angewandte Chemie International Edition*, vol. 47, no. 1, pp. 142–144, 2008.

[36] L. Zhu, B. Wang, S. Handschuh-Wang, and X. Zhou, "Liquid metal–based soft microfluidics," *Small*, vol. 16, no. 9, p. 1903841, 2020.

[37] C. B. Eaker and M. D. Dickey, "Liquid metals as ultra-stretchable, soft, and shape reconfigurable conductors," in *Micro-and Nanotechnology Sensors, Systems, and Applications VII*, vol. 9467. SPIE, 2015, pp. 21–29.

[38] N. Kazem, T. Hellebrekers, and C. Majidi, "Soft multifunctional composites and emulsions with liquid metals," *Advanced Materials*, vol. 29, no. 27, p. 1605985, 2017.

[39] R. Tutika, S. Kmiec, A. T. Haque, S. W. Martin, and M. D. Bartlett, "Liquid metal–elastomer soft composites with independently controllable and highly tunable droplet size and volume loading," *ACS applied materials & interfaces*, vol. 11, no. 19, pp. 17 873–17 883, 2019.

[40] A. Fassler and C. Majidi, "Liquid-phase metal inclusions for a conductive polymer composite," *Advanced Materials*, vol. 27, no. 11, pp. 1928–1932, 2015.

[41] Z. Yu, J. Shang, X. Niu, Y. Liu, G. Liu, P. Dhanapal, Y. Zheng, H. Yang, Y. Wu, Y. Zhou *et al.*, "A composite elastic conductor with high dynamic stability based on 3d-calabash bunch conductive network structure for wearable devices," *Advanced Electronic Materials*, vol. 4, no. 9, p. 1800137, 2018.

[42] H. Wang, Y. Yao, Z. He, W. Rao, L. Hu, S. Chen, J. Lin, J. Gao, P. Zhang, X. Sun *et al.*, "A highly stretchable liquid metal polymer as reversible transitional insulator and conductor," *Advanced Materials*, vol. 31, no. 23, p. 1901337, 2019.

[43] J. Tabor, K. Chatterjee, and T. K. Ghosh, "Smart textile-based personal thermal comfort systems: current status and potential solutions," *Advanced Materials Technologies*, vol. 5, no. 5, p. 1901155, 2020.

[44] H. Wu, Y. Huang, F. Xu, Y. Duan, and Z. Yin, "Energy harvesters for wearable and stretchable electronics: from flexibility to stretchability," *Advanced materials*, vol. 28, no. 45, pp. 9881–9919, 2016.

[45] A. R. M. Siddique, S. Mahmud, and B. Van Heyst, "A review of the state of the science on wearable thermoelectric power generators (tegs) and their existing challenges," *Renewable and Sustainable Energy Reviews*, vol. 73, pp. 730–744, 2017.

[46] S. W. Ula, N. A. Traugutt, R. H. Volpe, R. R. Patel, K. Yu, and C. M. Yakacki, "Liquid crystal elastomers: an introduction and review of emerging technologies," *Liquid Crystals Reviews*, vol. 6, no. 1, pp. 78–107, 2018.

[47] X. Qian, Q. Chen, Y. Yang, Y. Xu, Z. Li, Z. Wang, Y. Wu, Y. Wei, and Y. Ji, "Untethered recyclable tubular actuators with versatile locomotion for soft continuum robots," *Advanced Materials*, vol. 30, no. 29, p. 1801103, 2018.

[48] A. Kotikian, R. L. Truby, J. W. Boley, T. J. White, and J. A. Lewis, "3d printing of liquid crystal elastomeric actuators with spatially programed nematic order," *Advanced materials*, vol. 30, no. 10, p. 1706164, 2018.

[49] Y. Wang, Z. Wang, Q. He, P. Iyer, and S. Cai, "Electrically controlled soft actuators with multiple and reprogrammable actuation modes," *Advanced Intelligent Systems*, vol. 2, no. 6, p. 1900177, 2020.

[50] N. Torras, K. E. Zinoviev, J. Esteve, and A. Sánchez-Ferrer, "Liquid-crystalline elastomer micropillar array for haptic actuation," *Journal of Materials Chemistry C*, vol. 1, no. 34, pp. 5183–5190, 2013.

[51] M. J. Ford, C. P. Ambulo, T. A. Kent, E. J. Markvicka, C. Pan, J. Malen, T. H. Ware, and C. Majidi, "A multifunctional shape-morphing elastomer with liquid metal inclusions," *Proceedings of the National Academy of Sciences*, vol. 116, no. 43, pp. 21 438–21 444, 2019.

[52] A. Kotikian, C. McMahan, E. C. Davidson, J. M. Muhammad, R. D. Weeks, C. Daraio, and J. A. Lewis, "Untethered soft robotic matter with passive control of shape morphing and propulsion," *Science robotics*, vol. 4, no. 33, p. eaax7044, 2019.

[53] Z. Shen, F. Chen, X. Zhu, K.-T. Yong, and G. Gu, "Stimuli-responsive functional materials for soft robotics," *Journal of Materials Chemistry B*, vol. 8, no. 39, pp. 8972–8991, 2020.

[54] C. P. Ambulo, J. J. Burroughs, J. M. Boothby, H. Kim, M. R. Shankar, and T. H. Ware, "Four-dimensional printing of liquid crystal elastomers," *ACS applied materials & interfaces*, vol. 9, no. 42, pp. 37 332–37 339, 2017.

[55] S. I. Rich, R. J. Wood, and C. Majidi, "Untethered soft robotics," *Nature Electronics*, vol. 1, no. 2, pp. 102–112, 2018.

[56] D. J. Roach, C. Yuan, X. Kuang, V. C.-F. Li, P. Blake, M. L. Romero, I. Hammel, K. Yu, and H. J. Qi, "Long liquid crystal elastomer fibers with large reversible actuation strains for smart textiles and artificial muscles," *ACS applied materials & interfaces*, vol. 11, no. 21, pp. 19 514–19 521, 2019.

[57] J. M. Boothby, J. C. Gagnon, E. McDowell, T. Van Volkenburg, L. Currano, and Z. Xia, "An untethered soft robot based on liquid crystal elastomers," *Soft Robotics*, vol. 9, no. 1, pp. 154–162, 2022.

[58] Q. He, Z. Wang, Y. Wang, A. Minori, M. T. Tolley, and S. Cai, "Electrically controlled liquid crystal elastomer–based soft tubular actuator with multimodal actuation," *Science advances*, vol. 5, no. 10, p. eaax5746, 2019.

[59] S. Li, H. Bai, Z. Liu, X. Zhang, C. Huang, L. W. Wiesner, M. Silberstein, and R. F. Shepherd, "Digital light processing of liquid crystal elastomers for self-sensing artificial muscles," *Science Advances*, vol. 7, no. 30, p. eabg3677, 2021.

[60] T. H. Ware, M. E. McConney, J. J. Wie, V. P. Tondiglia, and T. J. White, "Voxelated liquid crystal elastomers," *Science*, vol. 347, no. 6225, pp. 982–984, 2015.

[61] C. Zhang, X. Lu, G. Fei, Z. Wang, H. Xia, and Y. Zhao, "4d printing of a liquid crystal elastomer with a controllable orientation gradient," *ACS applied materials & interfaces*, vol. 11, no. 47, pp. 44 774–44 782, 2019.

[62] T. A. Kent, M. J. Ford, E. J. Markvicka, and C. Majidi, "Soft actuators using liquid crystal elastomers with encapsulated liquid metal joule heaters," *Multifunctional Materials*, vol. 3, no. 2, p. 025003, 2020.

[63] C. Yuan, D. J. Roach, C. K. Dunn, Q. Mu, X. Kuang, C. M. Yakacki, T. Wang, K. Yu, and H. J. Qi, "3d printed reversible shape changing soft actuators assisted by liquid crystal elastomers," *Soft Matter*, vol. 13, no. 33, pp. 5558–5568, 2017.

[64] M. J. Ford, M. Palaniswamy, C. P. Ambulo, T. H. Ware, and C. Majidi, "Size of liquid metal particles influences actuation properties of a liquid crystal elastomer composite," *Soft Matter*, vol. 16, no. 25, pp. 5878–5885, 2020.

[65] A. Kotikian, J. M. Morales, A. Lu, J. Mueller, Z. S. Davidson, J. W. Boley, and J. A. Lewis, "Innervated, self-sensing liquid crystal elastomer actuators with closed loop control," *Advanced Materials*, vol. 33, no. 27, p. 2101814, 2021.

[66] C. P. Ambulo, M. J. Ford, K. Searles, C. Majidi, and T. H. Ware, "4d-printable liquid metal–liquid crystal elastomer composites," *ACS applied materials & interfaces*, vol. 13, no. 11, pp. 12 805–12 813, 2020.

[67] A. F. Minori, Q. He, P. E. Glick, I. Adibnazari, A. Stopol, S. Cai, and M. T. Tolley, "Reversible actuation for self-folding modular machines using liquid crystal elastomer," *Smart Materials and Structures*, vol. 29, no. 10, p. 105003, 2020.

[68] C. Wang, K. Sim, J. Chen, H. Kim, Z. Rao, Y. Li, W. Chen, J. Song, R. Verduzco, and C. Yu, "Soft ultrathin electronics innervated adaptive fully soft robots," *Advanced Materials*, vol. 30, no. 13, p. 1706695, 2018.

[69] H. Liu, H. Tian, J. Shao, Z. Wang, X. Li, C. Wang, and X. Chen, "An electrically actuated soft artificial muscle based on a high-performance flexible electrothermal film and liquid-crystal elastomer," *ACS Applied Materials & Interfaces*, vol. 12, no. 50, pp. 56 338–56 349, 2020.

[70] H. Lu, Z. Zou, X. Wu, C. Shi, Y. Liu, and J. Xiao, "Biomimetic prosthetic hand enabled by liquid crystal elastomer tendons," *Micromachines*, vol. 12, no. 7, p. 736, 2021.

[71] C. A. Aubin, B. Gorissen, E. Milana, P. R. Buskohl, N. Lazarus, G. A. Slipher, C. Keplinger, J. Bongard, F. Iida, J. A. Lewis *et al.*, "Towards enduring autonomous robots via embodied energy," *Nature*, vol. 602, no. 7897, pp. 393–402, 2022.

[72] G. M. Whitesides, "Soft robotics," *Angewandte Chemie International Edition*, vol. 57, no. 16, pp. 4258–4273, 2018.

[73] P. Roberts, M. Zadan, and C. Majidi, "Soft tactile sensing skins for robotics," *Current Robotics Reports*, vol. 2, pp. 343–354, 2021.

[74] D. Chen and Q. Pei, "Electronic muscles and skins: a review of soft sensors and actuators," *Chemical reviews*, vol. 117, no. 17, pp. 11 239–11 268, 2017.

[75] C. Della Santina, M. G. Catalano, A. Bicchi, M. Ang, O. Khatib, and B. Siciliano, "Soft robots," *Encyclopedia of Robotics*, vol. 489, 2020.

[76] A. L. Evenchik, A. Q. Kane, E. Oh, and R. L. Truby, "Electrically controllable materials for soft, bioinspired machines," *Annual Review of Materials Research*, vol. 53, no. 1, pp. 225–251, 2023.

[77] S. G. Fitzgerald, G. W. Delaney, and D. Howard, "A review of jamming actuation in soft robotics," in *Actuators*, vol. 9, no. 4. MDPI, 2020, p. 104.

[78] Y.-Y. Xiao, Z.-C. Jiang, and Y. Zhao, "Liquid crystal polymer-based soft robots," *Advanced Intelligent Systems*, vol. 2, no. 12, p. 2000148, 2020.

[79] F. Suarez, A. Nozariasbmarz, D. Vashaee, and M. C. Öztürk, "Designing thermoelectric generators for self-powered wearable electronics," *Energy & Environmental Science*, vol. 9, no. 6, pp. 2099–2113, 2016.

[80] J. P. Rojas, D. Singh, S. B. Inayat, G. A. T. Sevilla, H. M. Fahad, and M. M. Hussain, "Micro and nano-engineering enabled new generation of thermoelectric generator

devices and applications," *ECS Journal of Solid State Science and Technology*, vol. 6, no. 3, p. N3036, 2017.

[81] M. Jung, S. Jeon, and J. Bae, "Scalable and facile synthesis of stretchable thermoelectric fabric for wearable self-powered temperature sensors," *RSC advances*, vol. 8, no. 70, pp. 39 992–39 999, 2018.

[82] L. Zhang, S. Lin, T. Hua, B. Huang, S. Liu, and X. Tao, "Fiber-based thermoelectric generators: materials, device structures, fabrication, characterization, and applications," *Advanced Energy Materials*, vol. 8, no. 5, p. 1700524, 2018.

[83] F. Schneider, T. Fellner, J. Wilde, and U. Wallrabe, "Mechanical properties of silicones for mems," *Journal of Micromechanics and Microengineering*, vol. 18, no. 6, p. 065008, 2008.

[84] X. Wei and J. Liu, "Power sources and electrical recharging strategies for implantable medical devices," *Frontiers of Energy and Power Engineering in China*, vol. 2, no. 1, pp. 1–13, 2008.

[85] J.-H. Bahk, H. Fang, K. Yazawa, and A. Shakouri, "Flexible thermoelectric materials and device optimization for wearable energy harvesting," *Journal of Materials Chemistry C*, vol. 3, no. 40, pp. 10 362–10 374, 2015.

[86] W. He, G. Zhang, X. Zhang, J. Ji, G. Li, and X. Zhao, "Recent development and application of thermoelectric generator and cooler," *Applied Energy*, vol. 143, pp. 1–25, 2015.

[87] S. L. Kim, K. Choi, A. Tazebay, and C. Yu, "Flexible power fabrics made of carbon nanotubes for harvesting thermoelectricity," *Acs Nano*, vol. 8, no. 3, pp. 2377–2386, 2014.

[88] M. Tomita, S. Oba, Y. Himeda, R. Yamato, K. Shima, T. Kumada, M. Xu, H. Takezawa, K. Mesaki, K. Tsuda *et al.*, "Modeling, simulation, fabrication, and characterization of a 10-$\mu w/cm^2$ class si-nanowire thermoelectric generator for iot applications," *IEEE Transactions on Electron Devices*, vol. 65, no. 11, pp. 5180–5188, 2018.

[89] J. Y. Oh, J. H. Lee, S. W. Han, S. S. Chae, E. J. Bae, Y. H. Kang, W. J. Choi, S. Y. Cho, J.-O. Lee, H. K. Baik *et al.*, "Chemically exfoliated transition metal dichalcogenide nanosheet-based wearable thermoelectric generators," *Energy & Environmental Science*, vol. 9, no. 5, pp. 1696–1705, 2016.

[90] J. Y. Kim, J. Y. Oh, and T. I. Lee, "Multi-dimensional nanocomposites for stretchable thermoelectric applications," *Applied Physics Letters*, vol. 114, no. 4, p. 043902, 2019.

[91] K. Nan, S. D. Kang, K. Li, K. J. Yu, F. Zhu, J. Wang, A. C. Dunn, C. Zhou, Z. Xie, M. T. Agne *et al.*, "Compliant and stretchable thermoelectric coils for energy harvesting in miniature flexible devices," *Science Advances*, vol. 4, no. 11, p. eaau5849, 2018.

[92] S. Jo, M. Kim, M. Kim, and Y. Kim, "Flexible thermoelectric generator for human body heat energy harvesting," *Electronics letters*, vol. 48, no. 16, pp. 1015–1017, 2012.

[93] S. Hong, Y. Gu, J. K. Seo, J. Wang, P. Liu, Y. S. Meng, S. Xu, and R. Chen, "Wearable thermoelectrics for personalized thermoregulation," *Science advances*, vol. 5, no. 5, p. eaaw0536, 2019.

[94] S. J. Kim, H. E. Lee, H. Choi, Y. Kim, J. H. We, J. S. Shin, K. J. Lee, and B. J. Cho, "High-performance flexible thermoelectric power generator using laser multiscanning lift-off process," *ACS nano*, vol. 10, no. 12, pp. 10 851–10 857, 2016.

[95] C. S. Kim, H. M. Yang, J. Lee, G. S. Lee, H. Choi, Y. J. Kim, S. H. Lim, S. H. Cho, and B. J. Cho, "Self-powered wearable electrocardiography using a wearable thermoelectric power generator," *ACS Energy Letters*, vol. 3, no. 3, pp. 501–507, 2018.

[96] M. D. Dickey, R. C. Chiechi, R. J. Larsen, E. A. Weiss, D. A. Weitz, and G. M. Whitesides, "Eutectic gallium-indium (egain): a liquid metal alloy for the formation of stable structures in microchannels at room temperature," *Advanced functional materials*, vol. 18, no. 7, pp. 1097–1104, 2008.

[97] K. B. Ozutemiz, J. Wissman, O. B. Ozdoganlar, and C. Majidi, "Egain–metal interfacing for liquid metal circuitry and microelectronics integration," *Advanced Materials Interfaces*, vol. 5, no. 10, p. 1701596, 2018.

[98] M. Tavakoli, M. H. Malakooti, H. Paisana, Y. Ohm, D. Green Marques, P. Alhais Lopes, A. P. Piedade, A. T. de Almeida, and C. Majidi, "Egain-assisted room-temperature sintering of silver nanoparticles for stretchable, inkjet-printed, thin-film electronics," *Advanced Materials*, vol. 30, no. 29, p. 1801852, 2018.

[99] S. H. Jeong, K. Hjort, and Z. Wu, "Tape transfer atomization patterning of liquid alloys for microfluidic stretchable wireless power transfer," *Scientific reports*, vol. 5, no. 1, pp. 1–7, 2015.

[100] M. D. Dickey, "Stretchable and soft electronics using liquid metals," *Advanced Materials*, vol. 29, no. 27, p. 1606425, 2017.

[101] B. Chen, M. Kruse, B. Xu, R. Tutika, W. Zheng, M. D. Bartlett, Y. Wu, and J. C. Claussen, "Flexible thermoelectric generators with inkjet-printed bismuth telluride nanowires and liquid metal contacts," *Nanoscale*, vol. 11, no. 12, pp. 5222–5230, 2019.

[102] S. H. Jeong, F. J. Cruz, S. Chen, L. Gravier, J. Liu, Z. Wu, K. Hjort, S.-L. Zhang, and Z.-B. Zhang, "Stretchable thermoelectric generators metallized with liquid alloy," *ACS applied materials & interfaces*, vol. 9, no. 18, pp. 15 791–15 797, 2017.

[103] F. Suarez, D. P. Parekh, C. Ladd, D. Vashaee, M. D. Dickey, and M. C. Öztürk, "Flexible thermoelectric generator using bulk legs and liquid metal interconnects for wearable electronics," *Applied energy*, vol. 202, pp. 736–745, 2017.

[104] E. J. Markvicka, M. D. Bartlett, X. Huang, and C. Majidi, "An autonomously electrically self-healing liquid metal–elastomer composite for robust soft-matter robotics and electronics," *Nature materials*, vol. 17, no. 7, pp. 618–624, 2018.

[105] Y. Chen, X. Hou, C. Ma, Y. Dou, and W. Wu, "Review of development status of bi2te3-based semiconductor thermoelectric power generation," *Advances in Materials Science and Engineering*, vol. 2018, 2018.

[106] L.-P. Hu, T.-J. Zhu, Y.-G. Wang, H.-H. Xie, Z.-J. Xu, and X.-B. Zhao, "Shifting up the optimum figure of merit of p-type bismuth telluride-based thermoelectric materials for power generation by suppressing intrinsic conduction," *NPG Asia Materials*, vol. 6, no. 2, pp. e88–e88, 2014.

[107] S. H. Tan, N.-T. Nguyen, Y. C. Chua, and T. G. Kang, "Oxygen plasma treatment for reducing hydrophobicity of a sealed polydimethylsiloxane microchannel," *Biomicrofluidics*, vol. 4, no. 3, p. 032204, 2010.

[108] J. Zhou, D. A. Khodakov, A. V. Ellis, and N. H. Voelcker, "Surface modification for pdms-based microfluidic devices," *Electrophoresis*, vol. 33, no. 1, pp. 89–104, 2012.

[109] M. H. Malakooti, B. A. Patterson, H.-S. Hwang, and H. A. Sodano, "Zno nanowire interfaces for high strength multifunctional composites with embedded energy harvesting," *Energy & Environmental Science*, vol. 9, no. 2, pp. 634–643, 2016.

[110] M. H. Malakooti, Z. Zhou, and H. A. Sodano, "Enhanced energy harvesting through nanowire based functionally graded interfaces," *Nano Energy*, vol. 52, pp. 171–182, 2018.

[111] S. Harada, T. Arie, S. Akita, and K. Takei, "Highly stable liquid–solid metal contact toward multilayered detachable flexible devices," *Advanced Electronic Materials*, vol. 1, no. 7, p. 1500080, 2015.

[112] A. P. Condos, L. Zimaras, J. Marlow, and M. Kurniawan, "Optimisation of wearable thermoelectric generators," *PAM Review Energy Science & Technology*, vol. 6, pp. 2–15, 2019.

[113] Q. He, Z. Wang, Y. Wang, Z. Song, and S. Cai, "Recyclable and self-repairable fluid-driven liquid crystal elastomer actuator," *ACS applied materials & interfaces*, vol. 12, no. 31, pp. 35 464–35 474, 2020.

[114] H. Zeng, O. M. Wani, P. Wasylczyk, R. Kaczmarek, and A. Priimagi, "Self-regulating iris based on light-actuated liquid crystal elastomer," *Advanced materials*, vol. 29, no. 30, p. 1701814, 2017.

[115] Z. Wang, K. Li, Q. He, and S. Cai, "A light-powered ultralight tensegrity robot with high deformability and load capacity," *Advanced Materials*, vol. 31, no. 7, p. 1806849, 2019.

[116] M. Rogóż, K. Dradrach, C. Xuan, and P. Wasylczyk, "A millimeter-scale snail robot based on a light-powered liquid crystal elastomer continuous actuator," *Macromolecular rapid communications*, vol. 40, no. 16, p. 1900279, 2019.

[117] X. Wang, Y. Wang, X. Wang, H. Niu, B. Ridi, J. Shu, X. Fang, C. Li, B. Wang, Y. Gao *et al.*, "A study of the microwave actuation of a liquid crystalline elastomer," *Soft Matter*, vol. 16, no. 31, pp. 7332–7341, 2020.

[118] J. Liu, Y. Gao, H. Wang, R. Poling-Skutvik, C. O. Osuji, and S. Yang, "Shaping and locomotion of soft robots using filament actuators made from liquid crystal elastomer–carbon nanotube composites," *Advanced Intelligent Systems*, vol. 2, no. 6, p. 1900163, 2020.

[119] S. Schuhladen, F. Preller, R. Rix, S. Petsch, R. Zentel, and H. Zappe, "Iris-like tunable aperture employing liquid-crystal elastomers," *Advanced materials*, vol. 26, no. 42, pp. 7247–7251, 2014.

[120] J. Wang, Y. Song, M. Zadan, Y. Shen, V. Chen, C. Majidi, and S. Kumar, "Wireless actuation for soft electronics-free robots," in *Proceedings of the 29th Annual International Conference on Mobile Computing and Networking*, 2023, pp. 1–16.

[121] Y. Song, M. Zadan, K. Misra, Z. Li, J. Wang, C. Majidi, and S. Kumar, "Navigating soft robots through wireless heating," in *2023 IEEE International Conference on Robotics and Automation (ICRA)*. IEEE, 2023, pp. 2598–2605.

[122] M. Wang, Z.-W. Cheng, B. Zuo, X.-M. Chen, S. Huang, and H. Yang, "Liquid crystal elastomer electric locomotives," *ACS Macro Letters*, vol. 9, no. 6, pp. 860–865, 2020.

[123] Q. He, Z. Wang, Y. Wang, Z. Wang, C. Li, R. Annapooranan, J. Zeng, R. Chen, and S. Cai, "Electrospun liquid crystal elastomer microfiber actuator," *Science Robotics*, vol. 6, no. 57, p. eabi9704, 2021.

[124] J. Huber, N. Fleck, and M. Ashby, "The selection of mechanical actuators based on performance indices," *Proceedings of the Royal Society of London. Series A: Mathematical, physical and engineering sciences*, vol. 453, no. 1965, pp. 2185–2205, 1997.

[125] M. Zadan, C. Chiew, C. Majidi, and M. H. Malakooti, "Liquid metal architectures for soft and wearable energy harvesting devices," *Multifunctional Materials*, vol. 4, no. 1, p. 012001, 2021.

[126] J. Lee, H. Sul, W. Lee, K. R. Pyun, I. Ha, D. Kim, H. Park, H. Eom, Y. Yoon, J. Jung *et al.*, "Stretchable skin-like cooling/heating device for reconstruction of artificial thermal sensation in virtual reality," *Advanced Functional Materials*, vol. 30, no. 29, p. 1909171, 2020.

[127] J. Lee, D. Kim, H. Sul, and S. H. Ko, "Thermo-haptic materials and devices for wearable virtual and augmented reality," *Advanced Functional Materials*, vol. 31, no. 39, p. 2007376, 2021.

[128] S. Petsch, R. Rix, B. Khatri, S. Schuhladen, P. Müller, R. Zentel, and H. Zappe, "Smart artificial muscle actuators: Liquid crystal elastomers with integrated temperature feedback," *Sensors and Actuators A: Physical*, vol. 231, pp. 44–51, 2015.

[129] A. Wertz, A. P. Sabelhaus, and C. Majidi, "Trajectory optimization for thermally-actuated soft planar robot limbs," in *2022 IEEE 5th International Conference on Soft Robotics (RoboSoft)*. IEEE, 2022, pp. 439–446.

[130] A. Ianagui and E. A. Tannuri, "A sliding mode torque and position controller for an antagonistic sma actuator," *Mechatronics*, vol. 30, pp. 126–139, 2015.

[131] M. Moallem and V. A. Tabrizi, "Tracking control of an antagonistic shape memory alloy actuator pair," *IEEE Transactions on control systems technology*, vol. 17, no. 1, pp. 184–190, 2008.

[132] D. K. Patel, A. H. Sakhaei, M. Layani, B. Zhang, Q. Ge, and S. Magdassi, "Highly stretchable and uv curable elastomers for digital light processing based 3d printing," *Advanced Materials*, vol. 29, no. 15, p. 1606000, 2017.

[133] J. Lee, H. Sul, Y. Jung, H. Kim, S. Han, J. Choi, J. Shin, D. Kim, J. Jung, S. Hong *et al.*, "Thermally controlled, active imperceptible artificial skin in visible-to-infrared range," *Advanced Functional Materials*, vol. 30, no. 36, p. 2003328, 2020.

[134] C. Yakacki, M. Saed, D. Nair, T. Gong, S. Reed, and C. Bowman, "Tailorable and programmable liquid-crystalline elastomers using a two-stage thiol–acrylate reaction," *Rsc Advances*, vol. 5, no. 25, pp. 18 997–19 001, 2015.

[135] M.-Y. Lee, J.-H. Seo, H.-S. Lee, and K. S. Garud, "Power generation, efficiency and thermal stress of thermoelectric module with leg geometry, material, segmentation and two-stage arrangement," *Symmetry*, vol. 12, no. 5, p. 786, 2020.

[136] S. Carreon-Bautista, A. Eladawy, A. N. Mohieldin, and E. Sánchez-Sinencio, "Boost converter with dynamic input impedance matching for energy harvesting with multi-array thermoelectric generators," *IEEE Transactions on Industrial Electronics*, vol. 61, no. 10, pp. 5345–5353, 2014.

[137] Y. Jung, J. Choi, Y. Yoon, H. Park, J. Lee, and S. H. Ko, "Soft multi-modal thermoelectric skin for dual functionality of underwater energy harvesting and thermoregulation," *Nano Energy*, vol. 95, p. 107002, 2022.

[138] H. Lee, H. Kim, I. Ha, J. Jung, P. Won, H. Cho, J. Yeo, S. Hong, S. Han, J. Kwon *et al.*, "Directional shape morphing transparent walking soft robot," *Soft Robotics*, vol. 6, no. 6, pp. 760–767, 2019.

[139] Z. J. Patterson, A. P. Sabelhaus, K. Chin, T. Hellebrekers, and C. Majidi, "An untethered brittle star-inspired soft robot for closed-loop underwater locomotion," in *2020 IEEE/RSJ International Conference on Intelligent Robots and Systems (IROS)*. IEEE, 2020, pp. 8758–8764.

[140] S. Song, S. Joshi, and J. Paik, "Cmos-inspired complementary fluidic circuits for soft robots," *Advanced Science*, vol. 8, no. 20, p. 2100924, 2021.

[141] Y. Yan, Y. Zhao, Y. Alsaid, B. Yao, Y. Zhang, S. Wu, and X. He, "Artificial phototropic systems for enhanced light harvesting based on a liquid crystal elastomer," *Advanced Intelligent Systems*, vol. 3, no. 10, p. 2000234, 2021.

[142] H. Guo, M. O. Saed, and E. M. Terentjev, "Heliotracking device using liquid crystalline elastomer actuators," *Advanced Materials Technologies*, vol. 6, no. 11, p. 2100681, 2021.

[143] M. H. Malakooti, M. Zadan, N. Kazem, and C. Majidi, "Liquid metal composites for flexible thermoelectric energy harvesting," in *Behavior and Mechanics of Multifunctional Materials XV*, vol. 11589. SPIE, 2021, pp. 57–64.

[144] V. Nair, A. N. Dalrymple, Z. Yu, G. Balakrishnan, C. J. Bettinger, D. J. Weber, K. Yang, and J. T. Robinson, "Miniature battery-free bioelectronics," *Science*, vol. 382, no. 6671, p. eabn4732, 2023.

[145] A. S. Khan and F. U. Khan, "A survey of wearable energy harvesting systems," *International Journal of Energy Research*, vol. 46, no. 3, pp. 2277–2329, 2022.

[146] Y.-W. Chong, W. Ismail, K. Ko, and C.-Y. Lee, "Energy harvesting for wearable devices: A review," *IEEE Sensors Journal*, vol. 19, no. 20, pp. 9047–9062, 2019.

[147] M. Dargusch, W.-D. Liu, and Z.-G. Chen, "Thermoelectric generators: alternative power supply for wearable electrocardiographic systems," *Advanced Science*, vol. 7, no. 18, p. 2001362, 2020.

[148] X.-L. Shi, J. Zou, and Z.-G. Chen, "Advanced thermoelectric design: from materials and structures to devices," *Chemical reviews*, vol. 120, no. 15, pp. 7399–7515, 2020.

[149] M. Sattar and W.-H. Yeo, "Recent advances in materials for wearable thermoelectric generators and biosensing devices," *Materials*, vol. 15, no. 12, p. 4315, 2022.

[150] Y. Yang, H. Hu, Z. Chen, Z. Wang, L. Jiang, G. Lu, X. Li, R. Chen, J. Jin, H. Kang *et al.*, "Stretchable nanolayered thermoelectric energy harvester on complex and dynamic surfaces," *Nano letters*, vol. 20, no. 6, pp. 4445–4453, 2020.

[151] M. Zadan, D. K. Patel, A. P. Sabelhaus, J. Liao, A. Wertz, L. Yao, and C. Majidi, "Liquid crystal elastomer with integrated soft thermoelectrics for shape memory actuation and energy harvesting," *Advanced Materials*, p. 2200857, 2022.

[152] H. You, Z. Li, Y. Shao, X. Yuan, W. Liu, H. Tang, Q. Zhang, Y. Yan, and X. Tang, "Flexible bi2te3-based thermoelectric generator with an ultra-high power density," *Applied Thermal Engineering*, vol. 202, p. 117818, 2022.

[153] Z. An, Q. Fu, J. Lv, T. Zhou, Y. Wu, Y. Lu, G. Liu, Z. Shi, X. li, F. Zhang *et al.*, "Body heat powered wirelessly wearable system for real-time physiological and biochemical monitoring," *Advanced Functional Materials*, p. 2303361, 2023.

[154] V. Padmanabhan Ramesh, Y. Sargolzaeiaval, T. Neumann, V. Misra, D. Vashaee, M. D. Dickey, and M. C. Ozturk, "Flexible thermoelectric generator with liquid metal interconnects and low thermal conductivity silicone filler," *npj Flexible Electronics*, vol. 5, no. 1, p. 5, 2021.

[155] M. Zadan, D. K. Patel, M. H. Malakooti, L. Yao, and C. Majidi, "Fabrication of 3d printed thermoelectric devices for integration into liquid crystal elastomer actuators," in *Smart Materials, Adaptive Structures and Intelligent Systems*, vol. 86274. American Society of Mechanical Engineers, 2022, p. V001T01A011.

[156] Y. Han, L.-E. Simonsen, and M. H. Malakooti, "Printing liquid metal elastomer composites for high-performance stretchable thermoelectric generators," *Advanced Energy Materials*, vol. 12, no. 34, p. 2201413, 2022.

[157] T. Pan, M. Pharr, Y. Ma, R. Ning, Z. Yan, R. Xu, X. Feng, Y. Huang, and J. A. Rogers, "Experimental and theoretical studies of serpentine interconnects on ultrathin elastomers for stretchable electronics," *Advanced Functional Materials*, vol. 27, no. 37, p. 1702589, 2017.

[158] F. Bossuyt, T. Vervust, and J. Vanfleteren, "Stretchable electronics technology for large area applications: fabrication and mechanical characterization," *IEEE Transactions on components, packaging and manufacturing technology*, vol. 3, no. 2, pp. 229–235, 2013.

[159] Z. J. Farrell and C. Tabor, "Control of gallium oxide growth on liquid metal eutectic gallium/indium nanoparticles via thiolation," *Langmuir*, vol. 34, no. 1, pp. 234–240, 2018.

[160] C. J. Thrasher, Z. J. Farrell, N. J. Morris, C. L. Willey, and C. E. Tabor, "Mechanoresponsive polymerized liquid metal networks," *Advanced Materials*, vol. 31, no. 40, p. 1903864, 2019.

[161] P. Won, C. S. Valentine, M. Zadan, C. Pan, M. Vinciguerra, D. K. Patel, S. H. Ko, L. M. Walker, and C. Majidi, "3d printing of liquid metal embedded elastomers for soft thermal and electrical materials," *ACS Applied Materials & Interfaces*, 2022.

[162] R. Herbert, P. Mocny, Y. Zhao, T.-C. Lin, J. Zhang, M. Vinciguerra, S. Surprenant, W. Y. D. Chan, S. Kumar, M. R. Bockstaller *et al.*, "Thermo-mechanically stable, liquid metal embedded soft materials for high-temperature applications," *Advanced Functional Materials*, p. 2309725, 2023.

[163] Y. Liu, S. Hou, X. Wang, L. Yin, Z. Wu, X. Wang, J. Mao, J. Sui, X. Liu, Q. Zhang *et al.*, "Passive radiative cooling enables improved performance in wearable thermoelectric generators," *Small*, vol. 18, no. 10, p. 2106875, 2022.

[164] G. Lee, C. S. Kim, S. Kim, Y. J. Kim, H. Choi, and B. J. Cho, "Flexible heatsink based on a phase-change material for a wearable thermoelectric generator," *Energy*, vol. 179, pp. 12–18, 2019.

[165] B. Lee, H. Cho, K. T. Park, J.-S. Kim, M. Park, H. Kim, Y. Hong, and S. Chung, "High-performance compliant thermoelectric generators with magnetically self-assembled soft heat conductors for self-powered wearable electronics," *Nature communications*, vol. 11, no. 1, pp. 1–12, 2020.

[166] H. Wei, J. Zhang, Y. Han, and D. Xu, "Soft-covered wearable thermoelectric device for body heat harvesting and on-skin cooling," *Applied Energy*, vol. 326, p. 119941, 2022.

[167] J. Yuan and R. Zhu, "A fully self-powered wearable monitoring system with systematically optimized flexible thermoelectric generator," *Applied energy*, vol. 271, p. 115250, 2020.

[168] Y. Wang, Y. Shi, D. Mei, and Z. Chen, "Wearable thermoelectric generator to harvest body heat for powering a miniaturized accelerometer," *Applied energy*, vol. 215, pp. 690–698, 2018.

[169] J. Park, G. Bhat, A. Nk, C. S. Geyik, U. Y. Ogras, and H. G. Lee, "Energy per operation optimization for energy-harvesting wearable iot devices," *Sensors*, vol. 20, no. 3, p. 764, 2020.

[170] A. Nozariasbmarz, R. A. Kishore, B. Poudel, U. Saparamadu, W. Li, R. Cruz, and S. Priya, "High power density body heat energy harvesting," *ACS applied materials & interfaces*, vol. 11, no. 43, pp. 40 107–40 113, 2019.

[171] Y. Sargolzaeiaval, V. P. Ramesh, and M. C. Ozturk, "A comprehensive analytical model for thermoelectric body heat harvesting incorporating the impact of human metabolism and physical activity," *Applied Energy*, vol. 324, p. 119738, 2022.

[172] C. Choi, Y. Ma, X. Li, S. Chatterjee, S. Sequeira, R. F. Friesen, J. R. Felts, and M. C. Hipwell, "Surface haptic rendering of virtual shapes through change in surface temperature," *Science Robotics*, vol. 7, no. 63, p. eabl4543, 2022.

[173] K. Kendall, "The adhesion and surface energy of elastic solids," *Journal of Physics D: Applied Physics*, vol. 4, no. 8, p. 1186, 1971.

[174] Z. J. Patterson, D. K. Patel, S. Bergbreiter, L. Yao, and C. Majidi, "A method for 3d printing and rapid prototyping of fieldable untethered soft robots," *Soft Robotics*, vol. 10, no. 2, pp. 292–300, 2023.

[175] W. Zu, Y. Ohm, M. R. Carneiro, M. Vinciguerra, M. Tavakoli, and C. Majidi, "A comparative study of silver microflakes in digitally printable liquid metal embedded elastomer inks for stretchable electronics," *Advanced Materials Technologies*, p. 2200534, 2022.

[176] P. A. Lopes, D. F. Fernandes, A. F. Silva, D. G. Marques, A. T. de Almeida, C. Majidi, and M. Tavakoli, "Bi-phasic ag–in–ga-embedded elastomer inks for digitally printed, ultra-stretchable, multi-layer electronics," *ACS Applied Materials & Interfaces*, vol. 13, no. 12, pp. 14 552–14 561, 2021.

[177] S. Yu and M. Kaviany, "Electrical, thermal, and species transport properties of liquid eutectic ga-in and ga-in-sn from first principles," *The Journal of chemical physics*, vol. 140, no. 6, 2014.

[178] W. Kong, N. U. H. Shah, T. V. Neumann, M. H. Vong, P. Kotagama, M. D. Dickey, R. Y. Wang, and K. Rykaczewski, "Oxide-mediated mechanisms of gallium foam generation and stabilization during shear mixing in air," *Soft Matter*, vol. 16, no. 25, pp. 5801–5805, 2020.

[179] P. Won, S. Coyle, S. H. Ko, D. Quinn, K. J. Hsia, P. LeDuc, and C. Majidi, "Controlling c2c12 cytotoxicity on liquid metal embedded elastomer (lmee)," *Advanced Healthcare Materials*, vol. 12, no. 17, p. 2202430, 2023.

[180] D. Zhang, W. Y. S. Lim, S. S. F. Duran, X. J. Loh, and A. Suwardi, "Additive manufacturing of thermoelectrics: emerging trends and outlook," *ACS Energy Letters*, vol. 7, no. 2, pp. 720–735, 2022.

[181] S. Chen, H.-Z. Wang, R.-Q. Zhao, W. Rao, and J. Liu, "Liquid metal composites," *Matter*, vol. 2, no. 6, pp. 1446–1480, 2020.

[182] M. Zadan, A. Wertz, D. Shah, D. K. Patel, W. Zu, Y. Han, J. Gelorme, H. J. Mea, L. Yao, M. H. Malakooti *et al.*, "Stretchable thermoelectric generators for self-powered wearable health monitoring," *Advanced Functional Materials*, p. 2404861, 2024.

[183] R. Tutika, S. H. Zhou, R. E. Napolitano, and M. D. Bartlett, "Mechanical and functional tradeoffs in multiphase liquid metal, solid particle soft composites," *Advanced Functional Materials*, vol. 28, no. 45, p. 1804336, 2018.

[184] L. Zhao, H. Liu, X. Chen, S. Chu, H. Liu, Z. Lin, Q. Li, G. Chu, and H. Zhang, "Liquid metal nano/micro-channels as thermal interface materials for efficient energy saving," *Journal of Materials Chemistry C*, vol. 6, no. 39, pp. 10 611–10 617, 2018.

[185] C.-W. Nan, R. Birringer, D. R. Clarke, and H. Gleiter, "Effective thermal conductivity of particulate composites with interfacial thermal resistance," *Journal of Applied Physics*, vol. 81, no. 10, pp. 6692–6699, 1997.

[186] Y. Hu and C. Majidi, "Dielectric elastomers with liquid metal and polydopamine-coated graphene oxide inclusions," *ACS Applied Materials & Interfaces*, vol. 15, no. 20, pp. 24 769–24 776, 2023.

[187] C. Chiew, M. J. Morris, and M. H. Malakooti, "Functional liquid metal nanoparticles: synthesis and applications," *Materials Advances*, vol. 2, no. 24, pp. 7799–7819, 2021.

[188] Y. Liu, W. Zhang, and H. Wang, "Synthesis and application of core–shell liquid metal particles: A perspective of surface engineering," *Materials Horizons*, vol. 8, no. 1, pp. 56–77, 2021.

[189] J. Yan, M. H. Malakooti, Z. Lu, Z. Wang, N. Kazem, C. Pan, M. R. Bockstaller, C. Majidi, and K. Matyjaszewski, "Solution processable liquid metal nanodroplets by surface-initiated atom transfer radical polymerization," *Nature nanotechnology*, vol. 14, no. 7, pp. 684–690, 2019.

[190] M. A. Creighton, M. C. Yuen, N. J. Morris, and C. E. Tabor, "Graphene-based encapsulation of liquid metal particles," *Nanoscale*, vol. 12, no. 47, pp. 23 995–24 005, 2020.

[191] Y. Wei, P. Zhang, R. A. Soomro, Q. Zhu, and B. Xu, "Advances in the synthesis of 2d mxenes," *Advanced materials*, vol. 33, no. 39, p. 2103148, 2021.

[192] M. Naguib, M. W. Barsoum, and Y. Gogotsi, "Ten years of progress in the synthesis and development of mxenes," *Advanced Materials*, vol. 33, no. 39, p. 2103393, 2021.

[193] K. Maleski, V. N. Mochalin, and Y. Gogotsi, "Dispersions of two-dimensional titanium carbide mxene in organic solvents," *Chemistry of Materials*, vol. 29, no. 4, pp. 1632–1640, 2017.

[194] A. S. Zeraati, S. A. Mirkhani, P. Sun, M. Naguib, P. V. Braun, and U. Sundararaj, "Improved synthesis of ti 3 c 2 t x mxenes resulting in exceptional electrical conductivity, high synthesis yield, and enhanced capacitance," *Nanoscale*, vol. 13, no. 6, pp. 3572–3580, 2021.

[195] Y. Liu, W. Zou, N. Zhao, and J. Xu, "Electrically insulating pbo/mxene film with superior thermal conductivity, mechanical properties, thermal stability, and flame retardancy," *Nature Communications*, vol. 14, no. 1, p. 5342, 2023.

[196] M. Safarkhani, B. F. Far, Y. Huh, and N. Rabiee, "Thermally conductive mxene," *ACS Biomaterials Science & Engineering*, vol. 9, no. 12, pp. 6516–6530, 2023.

[197] C. Lamiel, I. Hussain, O. R. Ogunsakin, and K. Zhang, "Mxene in core–shell structures: research progress and future prospects," *Journal of Materials Chemistry A*, vol. 10, no. 27, pp. 14 247–14 272, 2022.

[198] N. Driscoll, B. Erickson, B. B. Murphy, A. G. Richardson, G. Robbins, N. V. Apollo, G. Mentzelopoulos, T. Mathis, K. Hantanasirisakul, P. Bagga *et al.*, "Mxene-infused bioelectronic interfaces for multiscale electrophysiology and stimulation," *Science Translational Medicine*, vol. 13, no. 612, p. eabf8629, 2021.

[199] C. Chiew and M. H. Malakooti, "Are mxenes suitable for soft multifunctional composites?" *Materials Horizons*, vol. 10, no. 11, pp. 5110–5125, 2023.

[200] C. E. Shuck, A. Sarycheva, M. Anayee, A. Levitt, Y. Zhu, S. Uzun, V. Balitskiy, V. Zahorodna, O. Gogotsi, and Y. Gogotsi, "Scalable synthesis of ti3c2tx mxene," *Advanced Engineering Materials*, vol. 22, no. 3, p. 1901241, 2020.

[201] N. Otsu *et al.*, "A threshold selection method from gray-level histograms," *Automatica*, vol. 11, no. 285-296, pp. 23–27, 1975.

[202] G. M. Guttmann and Y. Gelbstein, "Mechanical properties of thermoelectric materials for practical applications," *Bringing thermoelectricity into reality*, pp. 63–80, 2018.

[203] O. Yamashita and S. Tomiyoshi, "Effect of annealing on thermoelectric properties of bismuth telluride compounds," *Japanese journal of applied physics*, vol. 42, no. 2R, p. 492, 2003.

[204] D.-B. Hyun, J.-S. Hwang, J.-D. Shim, and T. S. Oh, "Thermoelectric properties of (bi0. 25sb0. 75) 2te3 alloys fabricated by hot-pressing method," *Journal of materials science*, vol. 36, no. 5, pp. 1285–1291, 2001.

[205] T. M. Tritt, "Thermoelectric phenomena, materials, and applications," *Annual review of materials research*, vol. 41, no. 1, pp. 433–448, 2011.

[206] Z. Cao, E. Koukharenko, M. Tudor, R. Torah, and S. Beeby, "Flexible screen printed thermoelectric generator with enhanced processes and materials," *Sensors and Actuators A: Physical*, vol. 238, pp. 196–206, 2016.

[207] F. Kim, S. E. Yang, H. Ju, S. Choo, J. Lee, G. Kim, S.-h. Jung, S. Kim, C. Cha, K. T. Kim *et al.*, "Direct ink writing of three-dimensional thermoelectric microarchitectures," *Nature Electronics*, vol. 4, no. 8, pp. 579–587, 2021.

[208] S. E. Yang, F. Kim, F. Ejaz, G. S. Lee, H. Ju, S. Choo, J. Lee, G. Kim, S.-h. Jung, S. Ahn *et al.*, "Composition-segmented bisbte thermoelectric generator fabricated by multimaterial 3d printing," *Nano Energy*, vol. 81, p. 105638, 2021.

[209] Q. Xu, N. Oudalov, Q. Guo, H. M. Jaeger, and E. Brown, "Effect of oxidation on the mechanical properties of liquid gallium and eutectic gallium-indium," *Physics of fluids*, vol. 24, no. 6, p. 063101, 2012.

[210] A. F. Silva, H. Paisana, T. Fernandes, J. Góis, A. Serra, J. F. Coelho, A. T. de Almeida, C. Majidi, and M. Tavakoli, "High resolution soft and stretchable circuits with pva/liquid-metal mediated printing," *Advanced Materials Technologies*, vol. 5, no. 9, p. 2000343, 2020.

[211] M. Reis Carneiro, C. Majidi, and M. Tavakoli, "Multi-electrode printed bioelectronic patches for long-term electrophysiological monitoring," *Advanced Functional Materials*, vol. 32, no. 43, p. 2205956, 2022.

[212] S. Bhattacharjee, "Dls and zeta potential–what they are and what they are not?" *Journal of controlled release*, vol. 235, pp. 337–351, 2016.

[213] Y. Su, J. Zhao, W. Zhan, H. Yuan, L. Wu, G. Sui, and H. Zhang, "A multifunctional hydrogel fabricated via ultra-fast polymerization by graphene oxide-adsorbed liquid metal nanodroplets," *Chemical Engineering Journal*, vol. 435, p. 135018, 2022.

[214] M. Mousavi, M. B. Ghasemian, J. Han, Y. Wang, R. Abbasi, J. Yang, J. Tang, S. A. Idrus-Saidi, X. Guan, M. J. Christoe *et al.*, "Bismuth telluride topological insulator synthesized using liquid metal alloys: Test of no2 selective sensing," *Applied Materials Today*, vol. 22, p. 100954, 2021.

[215] N. Kong, D. S. Ha, A. Erturk, and D. J. Inman, "Resistive impedance matching circuit for piezoelectric energy harvesting," *Journal of Intelligent Material Systems and Structures*, vol. 21, no. 13, pp. 1293–1302, 2010.

[216] K. J. Åström, T. Hägglund, and K. J. Astrom, *Advanced PID control*. ISA-The Instrumentation, Systems, and Automation Society Research Triangle Park, 2006, vol. 461.

[217] K. J. Åström and R. M. Murray, "Feedback systems," *Princeton Univer*, 2008.

[218] D. Lee, H. Park, G. Park, J. Kim, H. Kim, H. Cho, S. Han, and W. Kim, "Liquid-metal-electrode-based compact, flexible, and high-power thermoelectric device," *Energy*, vol. 188, p. 116019, 2019.

[219] W. Ren, Y. Sun, D. Zhao, A. Aili, S. Zhang, C. Shi, J. Zhang, H. Geng, J. Zhang, L. Zhang *et al.*, "High-performance wearable thermoelectric generator with self-healing, recycling, and lego-like reconfiguring capabilities," *Science advances*, vol. 7, no. 7, p. eabe0586, 2021.

[220] P. Zhu, C. Shi, Y. Wang, Y. Wang, Y. Yu, Y. Wang, Y. Deng, and J. Xiao, "Recyclable, healable, and stretchable high-power thermoelectric generator," *Advanced Energy Materials*, vol. 11, no. 25, p. 2100920, 2021.

[221] H. Park, D. Lee, D. Kim, H. Cho, Y. Eom, J. Hwang, H. Kim, J. Kim, S. Han, and W. Kim, "High power output from body heat harvesting based on flexible thermoelectric system with low thermal contact resistance," *Journal of Physics D: Applied Physics*, vol. 51, no. 36, p. 365501, 2018.

[222] M. Sitti, "Physical intelligence as a new paradigm," *Extreme Mechanics Letters*, vol. 46, p. 101340, 2021.

[223] X. Fan, B. Liu, J. Ding, Y. Deng, X. Han, W. Hu, and C. Zhong, "Flexible and wearable power sources for next-generation wearable electronics," *Batteries & Supercaps*, vol. 3, no. 12, pp. 1262–1274, 2020.

[224] S. A. Hashemi, S. Ramakrishna, and A. G. Aberle, "Recent progress in flexible–wearable solar cells for self-powered electronic devices," *Energy & Environmental Science*, vol. 13, no. 3, pp. 685–743, 2020.

[225] Y. Zou, V. Raveendran, and J. Chen, "Wearable triboelectric nanogenerators for biomechanical energy harvesting," *Nano Energy*, vol. 77, p. 105303, 2020.

[226] G. Moretti, S. Rosset, R. Vertechy, I. Anderson, and M. Fontana, "A review of dielectric elastomer generator systems," *Advanced Intelligent Systems*, vol. 2, no. 10, p. 2000125, 2020.

[227] N. Sezer and M. Koç, "A comprehensive review on the state-of-the-art of piezoelectric energy harvesting," *Nano Energy*, vol. 80, p. 105567, 2021.

[228] M. H. Kang, G. J. Lee, J. H. Yun, and Y. M. Song, "Nfc-based wearable optoelectronics working with smartphone application for untact healthcare," *Sensors*, vol. 21, no. 3, p. 878, 2021.

[229] M. A. Zoui, S. Bentouba, J. G. Stocholm, and M. Bourouis, "A review on thermoelectric generators: Progress and applications," *Energies*, vol. 13, no. 14, p. 3606, 2020.

[230] Y. Shi, Y. Wang, D. Mei, B. Feng, and Z. Chen, "Design and fabrication of wearable thermoelectric generator device for heat harvesting," *IEEE Robotics and Automation Letters*, vol. 3, no. 1, pp. 373–378, 2017.

[231] R. W. Style, R. Tutika, J. Y. Kim, and M. D. Bartlett, "Solid–liquid composites for soft multifunctional materials," *Advanced Functional Materials*, vol. 31, no. 1, p. 2005804, 2021.

[232] I. D. Joshipura, H. R. Ayers, C. Majidi, and M. D. Dickey, "Methods to pattern liquid metals," *Journal of materials chemistry c*, vol. 3, no. 16, pp. 3834–3841, 2015.

[233] T. Daeneke, K. Khoshmanesh, N. Mahmood, I. A. De Castro, D. Esrafilzadeh, S. Barrow, M. Dickey, and K. Kalantar-Zadeh, "Liquid metals: fundamentals and applications in chemistry," *Chemical Society Reviews*, vol. 47, no. 11, pp. 4073–4111, 2018.

[234] A. Haake, R. Tutika, G. M. Schloer, M. D. Bartlett, and E. J. Markvicka, "On-demand programming of liquid metal-composite microstructures through direct ink write 3d printing," *Advanced Materials*, vol. 34, no. 20, p. 2200182, 2022.

[235] M. D. Bartlett, A. Fassler, N. Kazem, E. J. Markvicka, P. Mandal, and C. Majidi, "Stretchable, high-k dielectric elastomers through liquid-metal inclusions," *Advanced Materials*, vol. 28, no. 19, pp. 3726–3731, 2016.

ProQuest Number: 31488086

INFORMATION TO ALL USERS
The quality and completeness of this reproduction is dependent on the quality
and completeness of the copy made available to ProQuest.

Distributed by
ProQuest LLC a part of Clarivate (2024).
Copyright of the Dissertation is held by the Author unless otherwise noted.

This work is protected against unauthorized copying under Title 17,
United States Code and other applicable copyright laws.

This work may be used in accordance with the terms of the Creative Commons license
or other rights statement, as indicated in the copyright statement or in the metadata
associated with this work. Unless otherwise specified in the copyright statement
or the metadata, all rights are reserved by the copyright holder.

ProQuest LLC
789 East Eisenhower Parkway
Ann Arbor, MI 48108 USA